



Defense Nuclear Agency
Alexandria, VA 22310-3398



DNA-TR-95-71

Russian Cratering Tests

V. Adushkin
B. Ivanov
L. Pernik
Institute for Dynamics of Geospheres, RAS
Leninsky Prospect, 38
Karpus 6, Moscow, Russia



November 1995

19951207 015

Technical Report

CONTRACT No. DNA 001-94-C-0131

Approved for public release;
distribution is unlimited.

DTIC QUALITY INSPECTED 1

**Destroy this report when it is no longer needed. Do not
return to sender.**

**PLEASE NOTIFY THE DEFENSE NUCLEAR AGENCY,
ATTN: CSTI, 6801 TELEGRAPH ROAD, ALEXANDRIA, VA
22310-3398, IF YOUR ADDRESS IS INCORRECT, IF YOU
WISH IT DELETED FROM THE DISTRIBUTION LIST, OR
IF THE ADDRESSEE IS NO LONGER EMPLOYED BY YOUR
ORGANIZATION.**



DISTRIBUTION LIST UPDATE

This mailer is provided to enable DNA to maintain current distribution lists for reports. (We would appreciate your providing the requested information.)

- ☐ Add the individual listed to your distribution list.
- ☐ Delete the cited organization/individual.
- ☐ Change of address.

NOTE:

Please return the mailing label from the document so that any additions, changes, corrections or deletions can be made easily. For distribution cancellation or more information call DNA/IMAS (703) 325-1036.

NAME: _____

ORGANIZATION: _____

OLD ADDRESS

CURRENT ADDRESS

TELEPHONE NUMBER: () _____

DNA PUBLICATION NUMBER/TITLE

CHANGES/DELETIONS/ADDITIONS, etc.)

(Attach Sheet if more Space is Required)

DNA OR OTHER GOVERNMENT CONTRACT NUMBER: _____

CERTIFICATION OF NEED-TO-KNOW BY GOVERNMENT SPONSOR (if other than DNA): _____

SPONSORING ORGANIZATION: _____

CONTRACTING OFFICER OR REPRESENTATIVE: _____

SIGNATURE: _____

CUT HERE AND RETURN



DEFENSE NUCLEAR AGENCY
ATTN: IMAS
6801 TELEGRAPH ROAD
ALEXANDRIA, VA 22310-3398

DEFENSE NUCLEAR AGENCY
ATTN: IMAS
6801 TELEGRAPH ROAD
ALEXANDRIA, VA 22310-3398

REPORT DOCUMENTATION PAGE			Form Approved OMB No. 0704-0188	
<small>Public reporting burden of this collection of information is estimated to average 1 hour per response, including the time for reviewing instructions, searching existing data sources, gathering and maintaining the data needed, and completing and reviewing the collection of information. Send comments regarding this burden estimate or any other aspect of this collection of information, including suggestions for reducing this burden, to Washington Headquarters Services, Directorate for Information Operations and Reports, 1215 Jefferson Davis Highway, Suite 1204, Arlington, VA 22202-4302, and to the Office of Management and Budget, Paperwork Reduction Project (0704-0188), Washington, DC 20503.</small>				
1. AGENCY USE ONLY (Leave Blank)	2. REPORT DATE 951101	3. REPORT TYPE AND DATES COVERED Technical 940730 - 950130		
4. TITLE AND SUBTITLE Russian Cratering Tests		5. FUNDING NUMBERS C - DNA-001-94-C-0131 PE - 62715H PR - AB TA - KB WU - DH605030		
6. AUTHOR(S) V. Adushkin, B. Ivanov and L. Pernik				
7. PERFORMING ORGANIZATION NAME(S) AND ADDRESS(ES) Institute for Dynamics of Geospheres, RAS Leninsky Prospect, 38 Karpus 6, Moscow, Russia		8. PERFORMING ORGANIZATION REPORT NUMBER		
9. SPONSORING / MONITORING AGENCY NAME(S) AND ADDRESS(ES) Defense Nuclear Agency 6801 Telegraph Road Alexandria, VA 22310-3398 SPWE/Tremba		10. SPONSORING / MONITORING AGENCY REPORT NUMBER DNA-TR-95-71		
11. SUPPLEMENTARY NOTES This work was sponsored by the Defense Nuclear Agency under RDT&E RMC Code B 4662 D AB KB 60503 7010 A 25904D.				
12a. DISTRIBUTION / AVAILABILITY STATEMENT Approved for public release; distribution is unlimited.		12b. DISTRIBUTION CODE		
13. ABSTRACT (Maximum 200 words) <p>Crater dimensions and general geologic conditions are described for 18 nuclear explosive tests conducted at the Semipalatinsk Test Site. For the 6 buried excavation tests, high-speed dome photographic results are presented. For the 12 near surface bursts, ejecta data are presented. In addition, an analytical model similar to the Z-model and related small-scale (modeling) crater data are discussed.</p> <p>Abstract contributed by the DNA Program Manager.</p>				
14. SUBJECT TERMS Nuclear Crater Data Semipalatinsk Buried and Near-Surface Bursts Z-model			15. NUMBER OF PAGES 114	
			16. PRICE CODE	
17. SECURITY CLASSIFICATION OF REPORT UNCLASSIFIED	18. SECURITY CLASSIFICATION OF THIS PAGE UNCLASSIFIED	19. SECURITY CLASSIFICATION OF ABSTRACT UNCLASSIFIED	20. LIMITATION OF ABSTRACT SAR	

UNCLASSIFIED

SECURITY CLASSIFICATION OF THIS PAGE

CLASSIFIED BY :

N/A since UNCLASSIFIED

DECLASSIFY ON :

N/A since UNCLASSIFIED

SECURITY CLASSIFICATION OF THIS PAGE

UNCLASSIFIED

TABLE OF CONTENTS

Section	Page
FIGURES	iv
TABLES	viii
1 EXCAVATION EFFECTS OF UNDERGROUND NUCLEAR EXPLOSIONS	1
1.1 BOREHOLE 1004 EVENT	2
1.2 BOREHOLE 1003 EVENT	4
1.3 THE BHL 101 EXPLOSION	8
1.4 THE T-1 EVENT	9
1.5 THE T-2 EXPERIMENT	11
1.6 EXPLOSION IN THE BOREHOLE # 125	13
2 NEAR SURFACE NUCLEAR EXPLOSIONS	37
3 EXCAVATION EXPLOSIONS OF HE CHARGES	57
4 PHYSICAL MODELING OF EXCAVATING EXPLOSIONS	66
5 Z-MODEL FOR NEAR SURFACE BURSTS	71
5.1 HISTORICAL NOTES	71
5.2 MAIN IDEAS	71
5.3 USING OF THE Z-MODEL	77
5.4 Z-MODEL WITH SHEAR BULKING	78
5.5 AN EXAMPLE OF MASS BALANCE FOR SURFACE NUCLEAR EVENTS	80
6 REFERENCES	95
Appendix	
TERMINOLOGY AND NOMENCLATURE	A-1

Accession For	
NTIS GRA&I	<input checked="" type="checkbox"/>
DTIC TAB	<input type="checkbox"/>
Unannounced	<input type="checkbox"/>
Justification	
By _____	
Distribution/ _____	
Availability Codes	
Dist	Avail and/or Special
A-1	

FIGURES

Figure		Page
1.1	Geological Cross-Section of the Crater Created by the BHL 1004 Event. Dimensions in Meters.	15
1.2	Explosion Dome Contours at Various Moment of Time at the BHL 1003 Event.	16
1.3	Ground Zero, Free Surface Velocities as a Function of Time for Events BHL 1004 (1) and BHL 1003 (2).	17
1.4	Topography Map of the Crater Created at the BHL 1003 Event.	18
1.5	The Crater and Ejecta Deposits for the BHL 1003 Event (The Cross-Section Along the 1-1 Direction Shown at the Fig. 1.4).	19
1.6	The Dome Profile Evolution at the BHL 101 Event. Time Marks in Seconds.	21
1.7	The Geological Cross-Section Scheme for the BHL 101 Event.	22
1.8	The Geologic Cross-Section Along the I-I Direction in the Vicinity of the Borehole #2308.	23
1.9	Legend for the Fig. 1.8.	24
1.10	Dome Profiles at Various Moments of Time at the T-1 Event.	25
1.11	The Topographic Map of the T-1 Crater.	26
1.12	Crater Profiles Along Different Directions.	28
1.13	The Geologic Cross-Section Along the Line of Ground Zeros for the T-2 Event.	29
1.14	Legend for Fig. 1.13.	30
1.15	The Dome Evolution at the T-2 Explosion.	31
1.16	The Topographic Map of the Elongated T-2 Crater.	32

FIGURES (Continued)

Figure		Page
1.17	The Map of Profile's Directions.	33
1.18	Cross-Sections of the Elongated Crater.	34
1.19	The Dome Profile Evolution at the BHL 125 Event. Time Marks in Seconds.	35
1.20	The Cross-Section of Crater for the BHL 125 Event.	36
2.1	Typical Surface Burst Crater.	47
2.2	Profiles of Craters Along Different Azimuths for Events ## 1, 3, 5.	48
2.3	Profiles of Crater Along Different Azimuths for Event # 2.	49
2.4	Profiles of Crater Along Different Azimuths for Event # 4.	50
2.5	Profiles of Crater Along Different Azimuths for Events ## 6, 11.	51
2.6	Profiles of Crater Along Different Azimuths for Event # 7.	52
2.7	Profiles of Crater Along Different Azimuths for Event # 10.	53
2.8	Profiles of Craters Along Different Azimuths for Events ## 8, 9, 12.	54
2.9	Isolines of Ejecta Thickness for Surface Burst Events # 2, 4, 12. Dashed Lines - Crater Contur at the Pre- Event Ground Level.	55
2.10	Isolines of Ejecta Thickness for Surface Burst Events # 7, 10, 11. Dashed Lines - Crater Contur at the Pre- Event Ground Level.	56
3.1	Profiles of Craters for Burst ## 1 - 6.	60
3.2	Profiles of Craters for Burst ## 7 - 10.	61
3.3	Profiles of Craters for Burst ## 11 - 14.	62

FIGURES (Continued)

Figure		Page
3.4	Profiles of Craters for Burst ## 15 - 19.	63
3.5	Profiles of Craters for Burst ## 20 - 25.	64
3.6	Profiles of Craters for Bursts ## 26 - 29.	65
4.1	The Modelling Installation Diagram: 1 - Vacuum Chamber; 2 - Working Volume; 3 - Vacuum Pump; 4 - Vacuum Gauge; 5 - Oil Pressure Gauge; 6 - Differential Manometer; 7 - Mercury Manometer; Compound Pressure and Vacuum Gauge; 9 - Compressed Air Cylinder; 10 - Blasting Unit; 11 - Instrumentation Camera.	69
4.2	Across - and Along-Valley Crossections of the Dam at the River Uch-Terek, 1 - The Real Explosion Dam, 2 - The Model Simulation.	70
5.1	a). An Example of a Quarter-Space Experiment. The High Speed Movie Frames was Overlapped to Plot Ejecta Trajectories. Plastic Disks Embedded to the Wet Sand are Ejected With Decreasing With the Ejection Distance Velocities. (b) Z-Model Representation of the Same Experiment. The Material Ejected Along a Stream Tube at Later May be Seen at the Curtain.	83
5.2	(a) Crater Profile's Evolution Plotted From Overlapped High Speed Movie Frames. Profiles is Numbered at the Figure in ms. The Time of Crater Depth Formation, t_d , is about 3 Times Smaller Then the Crater Radius Formation. (b) Z-Model Representation of the Same Process. For Some Target Media (i.e. For Wet Sand) One Can Find the Critical	84
5.3	A General View of a Mass Balance During Cratering According to the Z-Model.	85
5.4	(a) Experimental Data [19] Illustrating the Sand.	86
5.5	Structural Uplift For the Surface Burst # 4 in Comparison With Z-Model Estimates.	87

FIGURES (Continued)

Figure		Page
5.6	Structural Uplift For the Surface Burst # 11 in Comparison With Z-Model Estimates.	91

TABLES

Table		Page
1.1	Explosion Dome Height, H_k , and Gas/Dust Cloud Top, H_{max} Versus Time at the BHL 1003 Event.	6
1.2	The Dome Growth at the T-1 Event. Time is Measured From the Beginning of the Surface Motion.	10
1.3	Initial Velocity of the Surface Motion According to Flash Light Markers Motion.	12
1.4	Main Dynamic Parameters of the T-3 Event.	12
2.1	List of Near Surface Bursts.	37
2.2	Crater Dimensions of Near Surface Bursts.	38
3.1	Explosions in Loess-Like Loam.	58
3.2	Explosions in Clay.	59
4.1	(No Title).	68

1. Excavation effects of underground nuclear explosions.

During the period 1965-1970 USSR conducted 6 underground excavation nuclear explosions. Mostly all these explosions devoted to the investigation of excavation processes to use them later for peaceful purposes. The explosion yields varied in a wide range from 0.2 kton to 120 kt. Explosion devices were buried into rocks at the Semipalatinsk Test Site (STS). General data on date and place of events are listed in the following table:

Name of event	Date	Greenwich time, h.m.s	Coordinates (degrees, minutes, seconds)		Site name
			N latitude	E longitude	
BHL 1004	15.01.65	6.00.00.8	49.56.06.0	79.00.33.7	Balapan
BHL1003	14.10.65	4.00.00.2	49.59.26.3	77.38.08.6	Sary-Uzen'
BHL 101	18.12.66	4.58.00.0	49.55.28.5	77.44.50.0	Sary-Usen'
T-1	21.10.68	3.52.00.0	49.43.40.3	78.29.10.6	Tel'kem
T-2	12.11.68	7.30.00.0	49.42.44.8	78.27.40.8	Tel'kem
BHL125	04.11.70	6.02.59.8	49.55.21.2	77.45.44.8	Sary-Uzen'

Comment: BHL = borehole

The set of instrumental measurements was conducted during explosion events. Particularly, seismic effects, airblast, radiation environment, and dust cloud motion were monitored. The explosion dome motion was recorded by movie. For more precise measurements of the dome motion, special flash light markers were embedded at the ground surface along the line through the ground zero point. The spacing of markers was 20 to 50 m. Flash light markers were ignited 3 sec before the explosion and glowed about 40 sec.

Crater dimensioned measured immediately by airborne photo. As soon as radiation environment allowed, ground topographic measurements were conducted. Main parameters of 6 explosions craters are presented in the table below:

Name of event	Yield, kton	DOB, m	Crater radius, m	Crater depth, m	Crater volume, 10^3 m^3
BHL 1004	140	175	200 to 215	100	6400
BHL1003	1.1	48	62	20	111
BHL 101	80	227	150	19	540
T-1	0.2	31.4	34 to 40	21	37
T-2	3x0.2	31.4	65 x 142 (raw)	16	77
BHL125	19	151.3	97	17.5	300

Comments: BHL = borehole. All crater dimensions are measured in respect to the pre-event ground surface. For the T-2 event the length and width of a channel are denoted.

Sections below present detailed description of rock properties at the test site, as well as peculiarities of the explosion process and crater dimensions.

1.1 Borehole 1004 event.

The explosion at the Borehole 1004 occurred January 15, 1965, 6h 0.8s Greenwich Mean Time (GMT). The device of 140 kton yield exploded at the depth 175 m. The main goal of the experiment was to test the possibility of nuclear explosion usage for industrial purposes, namely for large-scale ground excavation.

The geologic structure of the event's vicinity includes Low Carboniferous rocks, covered by relatively thin (5 to 7 m) sheet of Triassic and Quaternary deposits. Low Carboniferous rocks consist of polymictic and tuffogenetic sandstones, aleurolites, carbonaceous shales, and conglomerates. Rocks are shattered by tectonic disruptions, and include dikes of porphyrites. Triassic and Quaternary deposits consist of clays and loam.

The explosion device was placed in shale.

The averaged exploded rocks may be described by following mechanical parameters:

1. Density	2560 kg m ⁻³
2. Longitudinal seismic wave velocity	4800 m s ⁻¹
3. Compressive strength	430 to 600 bar
4. Tensile strength	70 bar
5. Poisson coefficient	0.34
6. Gas Bearing Coefficient (GBC) [?]	0.21

Two types of ground water may be distinguished at the test site: (i) alluvial water at sand-gravel Quaternary deposits, and (2) in-fracture water at Low Carboniferous rocks.

Water bearing strata are hydraulically connected and have the united surface. At both horizons ground water is bittered-salted due to chloride-sulfate-sodium salt content.

Movie cameras to register the event were installed along three azimuth at distances 5, 11 and 17 km. Approximately 40 msec after detonation the water began to fountain from drillholes with the velocity of 350 m/s. At the same time one observed the dome formation with a diameter of 600 m. Initial upward dome velocity at the ground zero was about 100 m/s. 3 seconds later maximum velocity of ejected rock was as large as 140 m/s. The diameter of the ejecta column increased with the velocity of 10 m/s.

At the end of 6th second the quick expanding condensation cloud formed at the top of the column. The condensation belt was observed around the base of the column during the next 4 seconds. Approximately 10 seconds after detonation the ejecta column reached the maximum height of 950 m with the diameter of 800 m.

The explosion creates the crater with the ejecta zone around (Fig. 1.1). Averaged crater dimensions are:

Rim crest diameter	520 m
Apparent diameter (at the pre-event surface)	400 to 430 m
Rim crest height above the pre-event surface	20 to 35 m
Ejecta zone outer radius (from GZ)	647 m
Ejecta zone width (from rim crest)	412 m
Maximum ejecta distance (from GZ)	900 to 1000 m
Apparent crater volume below the rim crest level	10268 m ³

[?] Gas Bearing Coefficient (GBC) is measured as the mass fraction of all volatiles removed by heating of a specimen to the temperature of 1000 to 1100C.

Apparent crater volume below the pre-event surface	6400 m ³
Ejecta volume at the rim	6616 m ³
Volume of the structural uplift at the rim	4095 m ³

Engineer-geological study allows to distinguish following elements of the crater and deformed zone.

The surface of the apparent crater (Fig. 1.1) constructed of gravel, shuttered gravel and small fragments of test site rocks. Initial apparent crater slope angles were:

North slope: 30°
South slope 55°
West slope 35°
East slope 40°

3.5 years after the event slope processes decreased slope angles correspondingly to 30°, 40°, 20°, and 30°. These slopes are stable. Due to the downslope motion, 1.7E6 m³ sloped into the crater, most of the volume from the South slope. Downsides decreased the apparent crater depth at the central part by 17 m. The internal crater volume decreased at 22% and became equal to 5.7 E6 m³ in comparison with the initial volume of 6.4 E6 m³.

Physical and mechanical properties of ejecta deposits are:

Specific density	2.5 to 2.85 g cm-3
Volume density	1.61 to 2.23 g cm-3
Moisture content	12 %
Porosity	45 %
Coefficient of porosity	0.88
Coefficient of water saturation	0.44

Size-frequency distribution (SFD) of fragmented material at South and East crater slopes was measured by sieve analyzes of samples of shallow digging, as well as by technique of oblique photoplanimetry (along the water channel slopes, and at the surface of ejecta deposits). SFD analysis show that the main part (93.7 %) of ejecta deposits consists of fragments below 200 mm. Fractions below 200 mm may be separated into 2 to 20 mm fraction (gravel&pebble fraction, Russian name "dresva") which presents 36.8%, and 20 to 200 mm fraction (pebble&cobble fraction, Russian name "tsheben") which presents 34%. Fraction above 200 mm (boulders) is disrupted more uniformly: the coefficient of variation is about 17% in contrast to 124 % for fractions below 200 mm.

Hydrotechnical investigations shown that the crater rim filtration properties allow to use it as a dam keeping the head of 10 m of water without any additional sealing screen.

The excavated rocks closed the river valley creating an artificial dam. To allow spring melted water to pass through, the special channel was constructed the first spring after the event. The channel connected the crater with the river valley. As the result, two water reservoirs were created: the internal one (the crater itself) and the external one (in the river valley with the crater rim as the dam). During the snow melting in spring of the first year after the explosion 10E6 m³ of water was stored in the external reservoir, about 7E6 m³ - in the internal reservoir. About 4E6 m³ of water infilled fractured zones beneath the crater.

1.2 Borehole 1003 event

The explosion BHL 1003 occurred October 14, 1965, 04h0.2sec GMT. The device with the yield of 1.1 kton detonated at the depth of 48 m.

The test was conducted to study the excavation process and seismic effects, including the influence of DOB to relative intensity of various kinds of seismic waves. Other goals were:

- to measure crater dimensions and the size of residual deformation zone;
- to study residual rock transformation at various distances from GZ;
- to study radioactive pollution of rocks and ground water;
- to study engineering properties of the ejecta rim deposits.

Local Geology of the site. The geologic cross-section shows that the site is constructed of Upper Devonian, Neogenic and Quaternary sediments.

Upper Devonian sediments are presented by mostly ferriferous thin-layered alevrolites and argillites of a deep-cherry color with inter-layers of gray sands. Above alevrolites fat dense clays are placed. These clays have greenish-gray color. Their thickness varies from 0.5 to 27 m (22 m at the ground zero point). Quaternary sediments are presented by loams of 3.7 m thickness. The peculiarity of these sediments is a high level of a gypsum content.

Averaged properties of rocks around the explosion device are:

- | | |
|----------------------------------|-------------------------|
| 1. Density | 2690 kg m ⁻³ |
| 2. Longitudinal wave velocity | 3650 m/s |
| 3. Compressive strength | 320 to 700 bar |
| 4. Tensile strength | 80 bar |
| 5. Poisson coefficient | 0.33 |
| 6. Gas Bearing Coefficient (GBS) | 0.054 |

Ground water. Across all the event site the water bearing horizon coincides with Devonian sediments. The device installation borehole was tamped by natural ground water and sand. The metallic plug was placed at the depth of 16 m. Above the plug the borehole was infilled with quartz sand.

General picture. The free surface motion at the GZ began 45 msec after the detonation. One can derive the average compression wave speed of 1100 m/s. Before this moment (approximately 20 msec after detonation) the light flash was observed at the borehole mouth. The flash looked like a cloud of radiating gases. The light flash lasted around 60 msec and totally went off after this moment. During this time the light source uplifted at 5 m above the surface.

At the same moment as the free surface began to move, one observed the water fountain not far from the borehole mouth. The shape of the fountain lost the visible contour very quickly. It seems to result from quick loss of a hydraulic head. About 200 msec the water fountain was observed above the growing dome surface as a column-like formation of a constant height.

The initial upward ground motion at the GZ was about 42 m/s. This value remained a constant during 150 to 200 msec after the ground motion began. Later (200 to 250 msec after detonation) one observed the secondary acceleration of the central dome region. One may connect it with the gas acceleration (in contrast to the free surface motion after the

compressive wave reflection). This acceleration continued about 200 msec. After 400 to 450 msec after detonation the secondary (gas) acceleration stopped. At this moment the dome summit uplifted at the height of 20 m; the upward velocity was about 60 m/s. Later the dome moved with a constant deceleration equal to normal gravity acceleration till the moment of the dome disruption.

At the beginning of the gas acceleration phase (210 msec after detonation) close to the borehole mouth the new fountain-like column appeared. Most probably this column-like feature was the jet of sand and water, infilled the borehole, together with construction elements placed close to the borehole mouth. The summit of the feature uplifted with the velocity of 70 m/s. The feature was well visible just to the explosion gas breakthrough 450 msec after detonation. The breakthrough was localized at the central part of the dome. It seems that the borehole itself played as a gas-conducting channel when the tamp material was thrown out. Initial velocity of breakthrough gases was 170 m/s. Initially the breakthrough looked like several jets emitted from the base of a column of ejected tamp material. As the gas outflow velocity was much higher than the ejected tamp material, the later stopped to be visible very soon after the gas breakthrough.

Breakthrough gas jets very soon transformed into a rather symmetrical cloud around the dome summit. As the dome uplifted, this cloud uplifted also, steadily expanding. Approximately 0.8 sec after detonation one observed the relatively bright shine of gas products at the upper part of the gas cloud. The glowing seems to connect with the outflow of the main cavity products to the atmosphere.

The glowing stopped after several tens of seconds. At the same time the gas cloud growth also stopped. The cloud uplift velocity decreased, and the dome surface overrun it. The cloud lost its shape. One saw separate jets from the cloud top: there were pieces of constructions accelerated during the gas breakthrough. Some construction details was accelerated to 80 to 100 m/s.

The gas cloud and dust tails of flying construction fragments began to drift with the wind.

The maximum ground dome uplift was about 180 to 190 m. Separated construction fragments uplifted at 400 m. The general picture of the dome growth is well seen at the Fig. 1.2, where contours of the dome and gas cloud at different time moments are plotted. Table 1.1 presents the time sequence of the explosion dome height, H_k , and gas/dust cloud top, H_{max} .

Table 1.1. Explosion dome height, H_k , and gas/dust cloud top, H_{max} versus time at the BHL 1003 event.

#	1	2	3	4	5	6	7	8	9	10	11	12
T, sec	.32	.66	.98	1.29	1.63	2.29	2.94	3.59	4.24	4.89	5.54	6.19
H_k , m	15	34	52.5	71	90	120	150	169	172	180	187	189
H_{max} , m	25	n.a.	112	n.a.	146	176	221	262	292	322	350	370

is the frame number at the Fig. 1.2.

Fig. 1.3 shows the time dependence of the dome uplift for BHL 1004 (I) and BHL 1003 (2) events. One can see on both curves the secondary acceleration of the epicentral part of the dome, which seems to be the result of acceleration due to gas expansion. For the BHL 1003 event the epicentral uplift velocity increased from 42 to 60 m/s during approximately 150 to 200 msec. 450 msec after detonation the dome uplift mostly stopped and further the dome fall back with the acceleration about 10 m s^{-2} (dashed line at the Fig. 1.3.)

Note, that secondary acceleration at the BHL 1004 event was recorded 2.35 sec after detonation. At this moment initial velocity of the dome uplift decreased from 102 m/s to 80 m/s. Then due to secondary (gas) acceleration the velocity increased to 156 m/s.

The BHL 1003 explosion resulted in the crater with following averaged parameters (measured 2 years after the event):

Crater rim diameter	141 m
Crater diameter at the pre-event surface	124 m
Ejecta deposits diameter	281 m
Crater depth below the rim crest	29 m
Crater depth below the pre-event surface	20 m
Rim crest height above the pre-event surface	9 m

The crater and the ejecta zone are mapped at the Fig. 1.4. The crater cross-section along the I-I line (see Fig.1.4) are shown at the Fig. 1.5.

Surface of the apparent crater consists of clays and Devonian alevrolite fragments of gravel, pebble and cobble fractions. Slopes of the apparent crater have an inclination of 40 degrees at the upper part, decreasing to 8 to 12 degrees at the lower part. The apparent crater volume below rim crest is $226 \text{E}3 \text{ m}^3$, the volume below the pre-event surface is $111 \text{E}3 \text{ m}^3$.

The ejecta deposits consist of fragments and boulders of clay with 10 to 30 % of rubble ("tsheben") fraction of Devonian alevrolite. The maximum ejecta thickness is 6.5 m, the averaged width is 70 m. Down to depth of 2.5 to 3 m one can see slag and soot in clays. Physics-mechanical and filtration properties of ejecta are closed to the initial ones for clays. Average fragment density is 2.72 g cm^{-3} , average ejecta deposit density is 1.8 g cm^{-3} , moisture content is 13.2 %, porosity is 32 to 46 %.

The volume of ejecta deposits is $120.5 \text{E}3 \text{ m}^3$.

For 2 years after the event the ejecta layer was monitored to register the subsidence. The averaged subsidence was no more than 2%.

The zone of residual deformations (or the zone of structural uplift) is situated under the crater rim, covered by ejecta. The maximum structural uplift of 6 m observed at the radius of 120 m, which corresponds the dome dimension at the moment of its maximum size. The volume of the structural uplift is $60.2\text{E}3 \text{ m}^3$.

The surface of the true crater consisted of clay material at the upper and middle parts, and of pebble&cobble ("tsheben") fraction of alevrolite below. The content of "tsheben" fraction in clays increases from top to bottom. All rocks keep their initial stratigraphy. The density of clay fragments is 2.72 g cm^{-3} , the average volume density is 1.92 g cm^{-3} . Moisture content is 24.4 %, porosity is 41.7%, The internal friction angle is 23 to 27 degrees, cohesion is about 0.15 to 0.5 bar. Physical and mechanical properties of clay remain the same as pre-event ones for Neogenic clays. The filtration coefficient varies with depth from zero value (for clay layer) to 4 to 500 m/day at the crater basement.

The true crater volume is $235\text{E}3 \text{ m}^3$ below the pre-event level. The volume of fallback rocks is $124\text{E}3 \text{ m}^3$. The fallback thickness is 43 m along the pre-event borehole position.

The rock failure zone consists of highly disrupted alevrolite's fragments of pebble&cobble ("tsheben"), gravel&pebble ("dresva") and dust fractions. The thickness of the rock failure zone is about 12 m below the true crater floor along the centerline. The filtration coefficient is up to 300 m/day. The volume of this zone is $13\text{E}3 \text{ m}^3$.

Between the true crater surface and the alevrolite/clay contact surface the zone of spall fracturing is situated. The rock in this zone is finely fractured alevrolites. The level of fracturing decreases with a distance from the GZ. The rock fracturing here occurred due to wave reflection from the boundary of different rocks. For this reason, in contrast to the failure zone, here fine dust fraction and slag material are absent.

Thickness of damaged by spall zone at the surface of the true crater is 6 to 8 m; maximum radius is about 80 m.

The highly fractured zone presents by intensively fractured alevrolites. Fracturing occurred as along old pre-existed fractures and along new directions. The drill core revealed fragments of 10 to 15 cm height, rarely up to 20 cm. This zone has a thickness of 21 m along the charge borehole, and goes up to 87.5 m along the pre-event ground surface. The zone volume is $631\text{E}3 \text{ m}^3$.

In comparison with initial values, the strength of alevrolites decreased by 25 to 35 %, Acoustic impedance decreased by 11%.

The zone of blocky fragmentation is presented by fractured alevrolites. Fracturing occurred along pre-existed fractures: old fractures were renovated and became wider. The drill core from this zone presents column of 20 cm height, rarely up to 40 cm height. The thickness of the zone along the crater centerline is about 20 m, horizontal radius along the pre-event ground surface is about 115 m.

The filtration coefficient in the zone of blocky fragmentation is 6 to 7 m/day. The zone volume is $1314\text{E}3 \text{ m}^3$.

Hydrologic monitoring during 3 years after the event shown the regional decreasing of the ground water level. The radius of a hydraulic depression was above 1000m. At the distance of 310 m from GZ the level decreased at 12 m.

Total restoration of the ground water level occurred 2.5 years after the event. No serious changes in the chemical composition of ground water was observed. No Sr^{90} was observed in ground water beyond the ejecta zone.

Infilling of the apparent crater began 3 months after the event. Maximum volume of the water in the crater was 500 m^3 . At the end of the 3d year mineral content in the water achieved 6 g per liter due to evaporation during summer seasons.

1.3. The BHL 101 explosion

The explosion at the borehole 101 occurred December 18, 1966, 4 hours 58 minutes GMT. The device of the yield 80 kton exploded at the depth 227 m.

The borehole 101 is situated at the same site as the borehole 1003. Upper part of the geological section presents clays down to the depth of 40 m, underlaid with sandstone. Rocks around the explosion device may be characterized with following parameters:

1. Density	2610 kg m ⁻³
2. Longitudinal seismic wave velocity	4000 m/s
3. Compressive strength	650 bar
4. Tensile strength	50 bar
5. Gas Bearing Coefficient (GBC)	0.128

When a compressive wave reached the surface, the dome began to form at the epicenter region. The initial dome uplift was not recorded by movie cameras as the flash light markers died out at the moment of compression wave impact. Poor visibility prevented to get measurable movie frames at the initial stages. For heights 20 to 50 m above the initial surface the dome uplift velocity was about 48 m/s. At the BHL 101 event the uplift velocity was larger than at the BHL 1003 event, despite the larger DOB value. It seems to result from the difference at the local scaled geologic structure parameters: at the BHL 1003 site more than a half of the overburden rocks are clays (25 m of clays versus 23 m of sandstone); at the same time at the BHL 101 site clay layer had thickness equal to 1/6 DOB only. Dome profiles are shown at the Fig. 1.6. Contours marked with the time values in sec. One can see that the distinct shape of the dome was observed during approximately 4 sec. The dome surface uplifted at the height of 120 m and practically stopped. The dome basement radius was around 700 m.

Approximately 4.5 s after the motion began, the light emission zones appeared at the dome surface. These lights seems to be connected with the gas breakthrough to the atmosphere. Simultaneously with these lights, a lot of jets appeared at the dome. Jets united to the joint front. As the result, the central part of the dome was totally destroyed. The uplift velocity of the destroyed part increased from zero to 80 to 100 m/s.

It is hard to say from the movie frames, how much was the mass of rock involved into gas breakthrough motion. It is interesting to note, that lights, which were visible during 0.7 s,

also uplifted as the dome evolved. During 0.45 s after appearance, their height increased at 50 to 60 m. If the dome surface itself would be in the same position, the fracture gas outlets, the most probable place of the light emission, would be at the same position too. So we have some ground to conclude that breakthrough gases involved some dome material into motion. An additional evidence is that separated rock fragments were well visible after separation from the gas cloud. The fall down of these rocks generated an essential base surge.

The explosion created the crater with following parameters:

- | | |
|---|---------------------|
| 1. Rim crest diameter | 404 m |
| 2. Crater diameter at the pre-event surface | 300 m |
| 3. Crater depth below the pre-event surface | 19 m |
| 4. Rim height above the pre-event surface | 10 m |
| 5. Apparent crater volume | $5.4E5 \text{ m}^3$ |

Fig. 1.7 demonstrates the BHL 101 crater cross-section and estimated cavity size. One can see that the crater is relatively shallow, and has a very rough floor. The central mound is at the crater center; the top of the central mound is at the depth of 4 m below the pre-event surface. Most deep part of the crater has a depth up to 19 m. The average crater depth may be estimated as 10 to 15 m.

1.4. The T-1 event

The T-1 explosion was conducted October 2, 1968, 3 h 52 m GMT. The device of 0.2 kton yield detonated at the depth of 31.4 m. The purpose of the experiment was to get parameters of mechanical effects and radioactive wasting for the following experiment with the group explosion of 3 charges 0.2 kton each.

The test site constructed of Devon and Carboniferous deposits. The test site situated at the North-East wing of the anticline, constructed of sedimentary Low Carboniferous deposits (Figs. 1.8 and 1.9). These deposits consist of gray non-uniformly grained quartz-feldspar sandstone with interlayers of dark-brown argilite and yellowish-brown alevrolite with a high content of organic materials. One can find seams of carbonaceous deposits up to 3 cm of thickness.

The top 24 m of rocks are highly weathered; one can easily crumble samples. Sandstone at 80 to 85% consists of terrigenic poor sorted material. The terrigenic material is presented by fragments of effusive rocks, quartz and plagioclase. Argilite and alevrolite are presented as separated blocks of interlayers. These interlayers include flat charred fragments of ancient plants. At the surface Low Carboniferous deposits are covered by Quaternary clays and sands with a thickness of 3 to 18 m.

Parameters of rock around the explosion device may be described as follows:

- | | |
|---------------------------------------|--------------------------|
| 1. Density | 2540 kg m^{-3} |
| 2. Longitudinal seismic wave velocity | 4670 m/s |
| 3. Compressive strength | 500 to 700 bar |
| 4. Tensile strength | 140 bar |
| 5. Poisson coefficient | 0.31 |
| 6. Gas Bearing Coefficient (GBC) | 0.128 |

Underground water has a free surface at the depth of 2 to 3 m.

First motion at the surface after the detonation was the outflow of seal materials from the charge borehole with the velocity of 100 m/s. Later the surface up to radius of 100 to 110 m from GZ began to uplift with the initial velocity (at GZ) of 43.6 m/s. Around the charge borehole one observed the uplift of construction waste material (sand, gravel). This material uplifted 5 m above the surface in 0.4 sec. The growing dome had a distinct shape.

The general picture of the ejection process was similar the event BHL 1003, except no hot gases broke through to the atmosphere.

The evolution of the dome profile in time is shown at the Fig. 1.10. Table 1.2. presents processed parameters of the dome growth measured by photo- and movie registration.

Table 1.2. The dome growth at the T-1 event. Time is measured from the beginning of the surface motion.

Time, s	0.12	0.34	1.29	2.24	3.19	4.14	5.09	6.09
Dome height, m	5.24	15.0	66	105	135	157	162	157
Dome diameter, m	-	-	75	100	125	150	165	180
Uplift velocity, m/s	43.6	44.3	53.7	41.0	31.6	23.2	5.3	-5.3

Table 1.2. shows that between 0.34 and 1.29 sec (after beginning of the surface motion) the uplift velocity increases at 10 m/s relative to the initial velocity. This is the evidence of the secondary gas acceleration when the dome get an additional velocity.

Later the uplift velocity gradually decreases to zero (at T=5 sec approximately) and the dome begins to descend. No breakthrough of hot gases and dome opening were observed at this experiment.

The upper part of the casing tube (20 m length) with the tamp material inside well overrun the dome surface having maximum velocity of 70 m/s. It uplifted at the height of 320 m.

The base surge began to form 3.2 sec after the beginning of the surface motion and developed during 40 sec. The average velocity of the radial spreading of the base surge was 8.5 m/s, maximum diameter was about 700 m, maximum height was 116 m.

The explosion created the crater and the ejecta zone. Figs. 1.11 and 1.12 present the topography of the surface after the explosion and the profile of the crater.

The apparent crater and ejecta zone have dimensions:

Crater diameter at the pre-event surface	60 to 80 m
Crater depth below the pre-event surface	21 m
Crater rim crest diameter	82 to 108 m
Crater rim height	8 to 19 m
Radius of the ejecta zone	110 to 140 m
Angle of the crater inner slope	35 degrees

Maximum flight distance of rock fragments was around 190 m. Due to the large volatile content the crater radius was 25 % larger than the predicted one, the crater depth was 40% large than predicted. Several days after the explosion the crater was filled with ground water.

1.5. The T-2 experiment

The explosion T-2 occurred November 12, 1968, 7 h 30 m GMT. Three explosion devices of 0.2 kton each detonated at three borehole (#2305, #2306, and #2307) 31.4 m below surface. The distance between charges was 40 m. The main purpose of the experiment was to obtain data on mechanical effects and radioactive wasting for future industrial using of underground nuclear explosions.

The test site constructed of Devonian and Carboniferous deposits. The test site is situated at the core of an anticline of effusive-sedimentary Upper Devonian rocks, including porfirite, alevrolite, and gravelite (Figs. 1.13 and 1.14). The surface of Upper Devonian rocks is covered with Quaternary clay and sand of 6 m thickness. Upper Devonian rocks are weathered to the depth 15 to 18 m. Below the weathered zone rocks are highly fracture. Fractures contain calcite.

Rocks around the device may be characterized as follows:

1. Density	2610 kg m ⁻³
2. Longitudinal seismic wave velocity	4360 m/s
3. Compressive strength	850 to 990 bar
4. Tensile strength	70 bar
5. Poisson coefficient	0.3
6. Gas Bearing Coefficient (GBC)	0.04

Underground water has a free surface at the depth of 2 to 3 m.

The first surface manifestation of the explosion was fountains of water from exploration boreholes with the initial velocity of 90 to 110 m/s. The ejection of tamp material from charge boreholes and overrun motion of casing tubes were not observed. The initial velocity of the surface motion at the GZ near the charge borehole #2306 was 43.2 m/s. The ground uplifted as a dome elongated along the line of charge. The central part of the dome uplifted a little bit faster. At 6.3 sec after the motion beginning the dome reached its maximum size: height of the central part was 112 to 115 m, length at the base was 205 m, width at the base was 147 m. The breakthrough of hot gases was not observed. The dome growth is illustrated at the Fig. 1.15.

Along the charge line special flash light markers were installed at the top of well founded drill bars. A high-zoom movie camera was used to measure the initial free surface velocity using flash light markers. Table 1.3. summarizes data on initial velocities.

Table 1.3. Initial velocity of the surface motion according to flash light markers motion.

# of light marker	Measured uplift velocity, m/s	The time moment of measurement, msec	Marker location
1	43.2	50	At the surface, 2.5 m form the central charge borehole # 2306
1	38.4	150	The same
2	74.0	70	At the bar casted to the case tube of the #2306 charge borehole
3	33.6	100	Between #2305 and #2306 boreholes
4	20.8	100	25 m from the charge line
5	33.2	100	Between #2306 and #2307 boreholes
6	29.6	100	15 m from the charge line

Main dynamic parameters of the event, measured by photo registration, are listed at the Table 1.4.

Table 1.4. Main dynamic parameters of the T-3 event.

Parameter:	Time, sec					
	0.15	0.87	1.94	3.0	4.08	5.15
Dome height, m, at:						
#2306 GZ	6.0	33.4	70.0	96.0	112	115
#2305 GZ	-	28.0	54.0	72.0	75.0	75
#2307 GZ	-	29.8	63.0	85.0	95.0	95
Dome uplift velocity, m/s, at:						
#2306 GZ	38.4	-	34.2	24.3	15.0	2.8
#2305 GZ	-	-	24.4	16.8	2.8	0
#2307 GZ	-	-	31.0	20.6	9.4	0
Dome width at the half height level above the day surface, m		90	100	115	140	165
Dome length at the half height level above the day surface, m		150	160	185	200	220

As in a single explosion event T-1, the breakthrough of hot gases was not observed. The dome subsidence generated the base surge with diameter of 600 to 800 m and height of 40 to 80 m.

According to the data processing it seems that the secondary gas acceleration phase was not as effective as at the single T-1 explosion. As a consequence the dome uplift velocity and maximum height were lower that during the single T-1 explosion. The difference of the gas acceleration phase intensity corresponds to the difference of volatile and moisture contents (expressed by the Gas Bearing Coefficient) at the site of the single explosion (GBC = 13 %) and the multiple explosion (4 %).

Small difference in surface uplift velocities at ground zero points and between them shows the proper charge interference at the chosen distance between charges.

The explosion of 3 in-line charges created the trench crater and the continuous ejecta zone (Fig. 1.16). The trench has a shape of an elongated ellipse. Side slopes of the crater between charges are almost parallel to the charge line.

The main parameters of the excavated trench are:

The trench length:

at the pre-event surface level	142 m
at the rim crest level	160 m

The trench width:

at the pre-event surface level	61 to 69 m
at the rim crest level	90 to 108 m

The trench depth below the pre-event surface level 16 m

Rim height above the pre-event surface level:

at trench sides	9 to 16 m
at trench ends	7 m

Continuous ejecta width:

at trench sides	95 m
at trench ends	65 m

Maximum ejecta flight distance from GZ 170 m

The trench volume;

below the pre-event surface level	77E3 m ³
below the rim crest level	187E3 m ³

1.6. Explosion in the borehole # 125

The explosion in the BHL 125 occurred November 4, 1970, 06 h 59.8 s GMT. The device of 19 kton yield detonated at the depth 151.3 m.

The geological cross section includes porfirite, alevrolite, light-green clay, sand-gravel deposits and loam. These rocks may be separated into two groups according to their physical and mechanical properties. The first group consists a bunch of loose and cohesive materials with thickness of 19 m at the ground zero. The second group includes porfirite and alevrolite.

Rock properties around the charge are follows:

1. Density	2750 kg m ⁻³
2. Longitudinal seismic wave velocity	4930 m/s
3. Compressive strength	1124 bar
4. Tensile strength	110 bar
5. Poisson coefficient	0.25
6. Gas Bearing Coefficient (GBC)	0.12

The surface events were observed as follows. After the compression wave arrival to the free surface, the dome began to uplift above the GZ region (Fig. 1.19). When the dome raised 30 m above the pre-event surface, its velocity was 36 m/s. The distinct dome shape was observed during 5 sec. During this period the dome uplifted at 98 m, the dome base diameter was 500

m. Approximately 3.5 sec after the surface motion beginning, the breakthrough of explosion products occurred at two points of the dome surface. The gas outflow involved some mass of the ground. The initial velocity of breakthrough jets was 35 m/s. At 5th and 6th seconds the gas luminosity was observed at the vicinity of the breakthrough.

The explosion resulted in the crater with following parameters:

1. Crater diameter at the pre-event surface	194 m
2. Crater rim crest diameter	282 m
3. Crater depth below the pre-event surface	17.5 m
4. Crater rim height	23 m
5. Apparent crater volume	$3E5 \text{ m}^3$

The crater cross-section is shown on Fig. 1.20. One can see the relatively shallow crater, which is very similar to the crater of the BHL 101 explosion: the similar central mound formed at the crater center. The crater depth here is about 9.5 m. The rim is non-symmetrical: the rim height varies from 7 to 23 m. Possibly this asymmetry is related to the oblique boundary surface between soft and hard rocks.

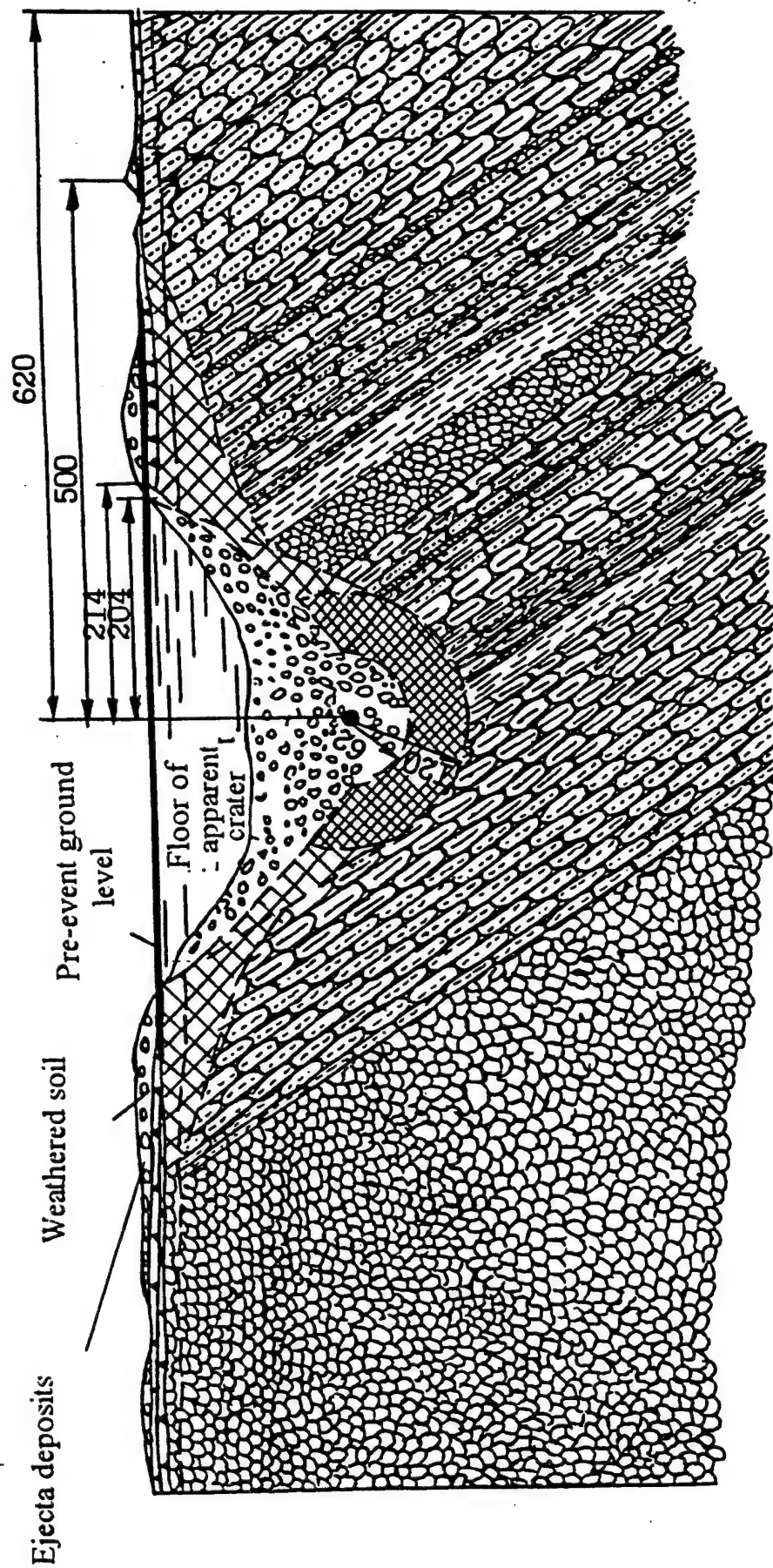


Fig. 1.1. Geological cross-section of the crater created by the BHL 1004 event. Dimensions in meters.

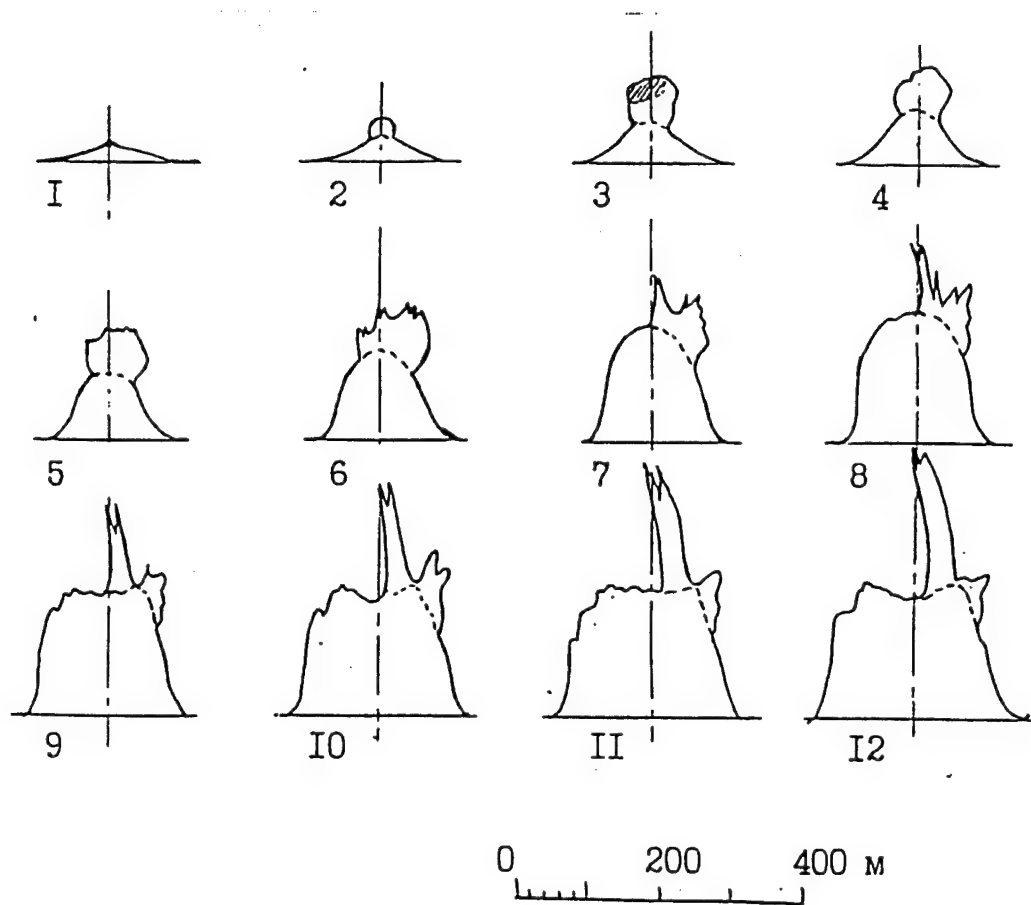


Fig. 1.2. Explosion dome contours at various moment of time at the BHL 1003 event.

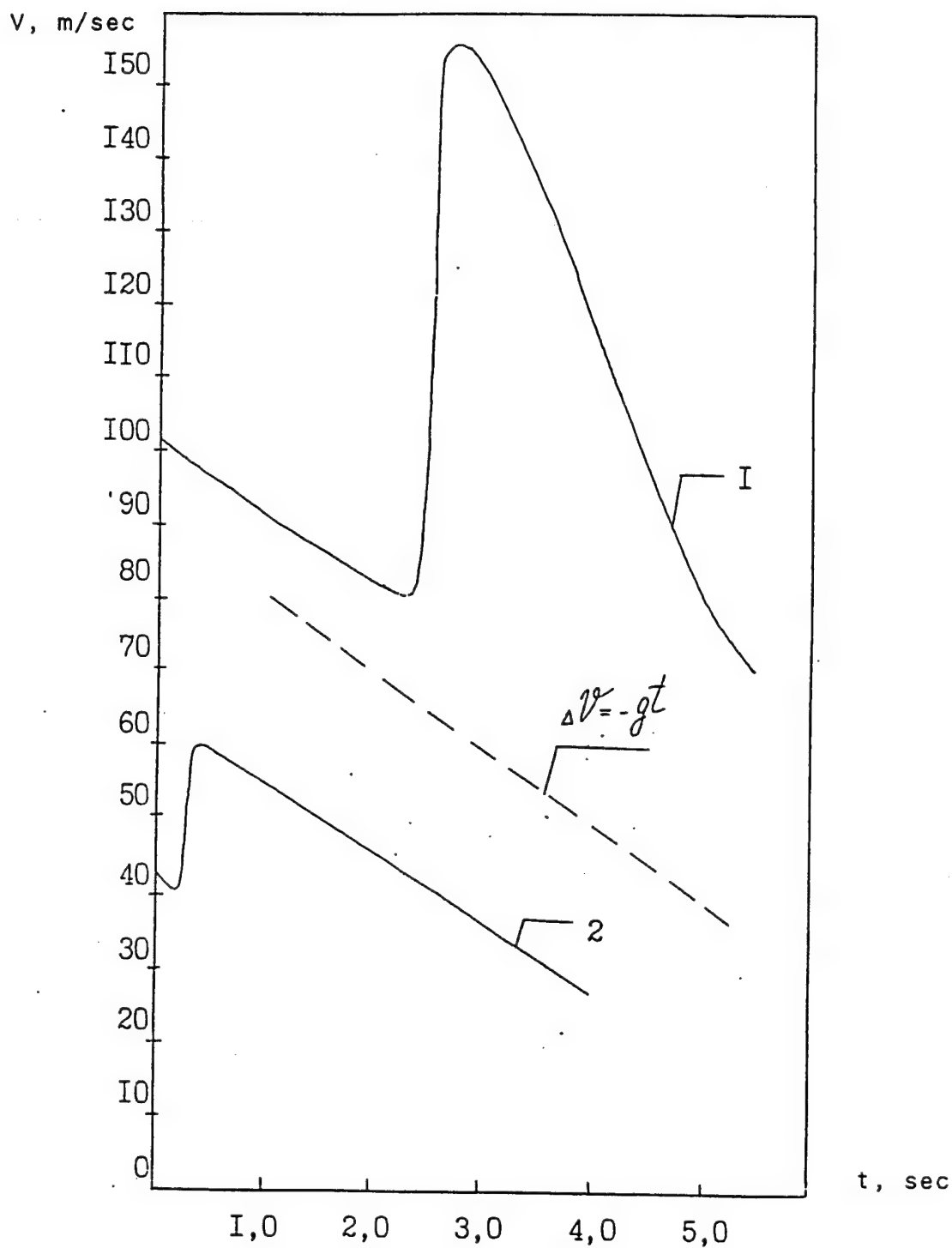


Fig. 1 3. Ground zero, free surface velocities as a function of time for events BHL 1004 (1) and BHL 1003 (2).

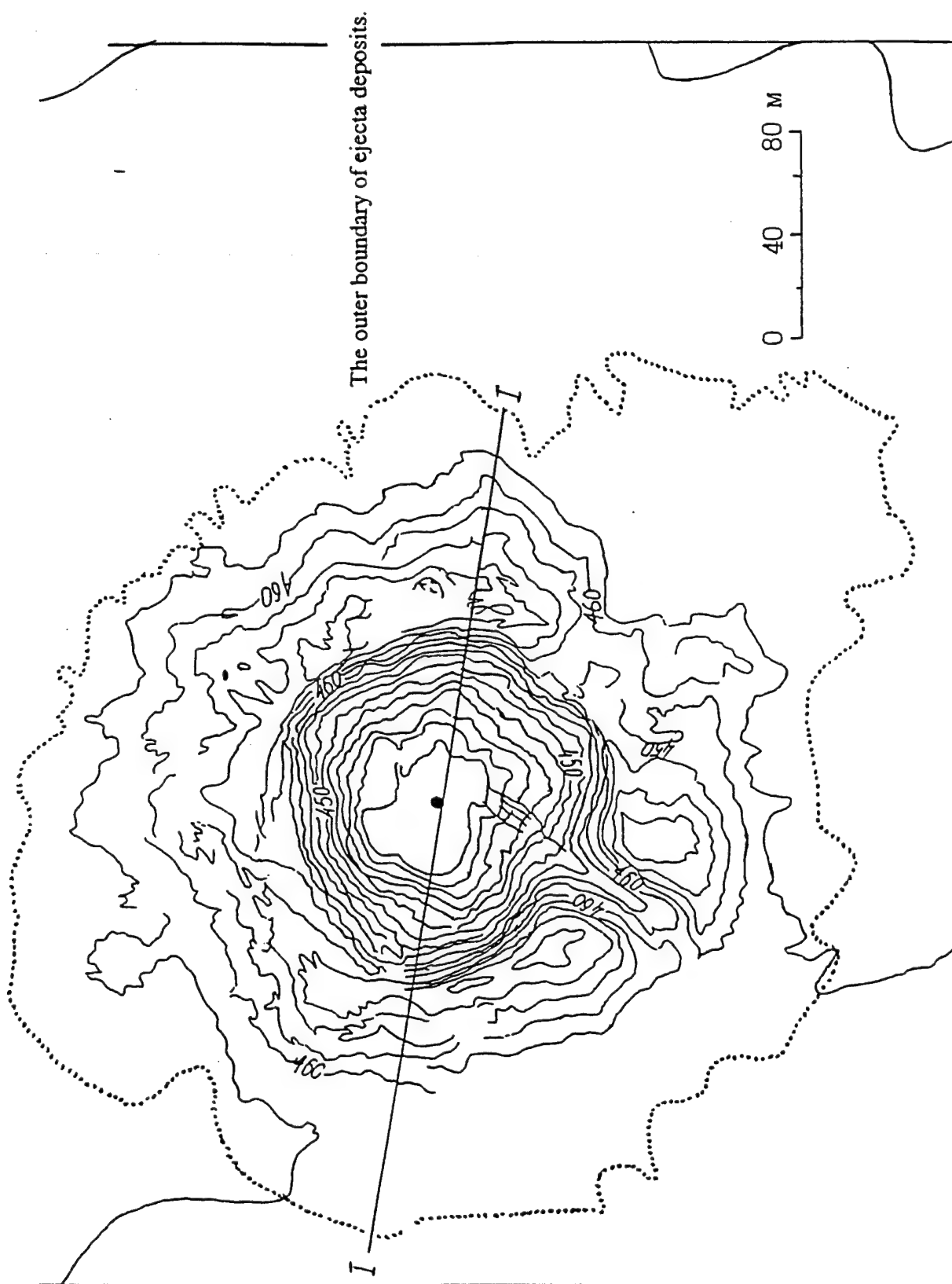


Fig. 1.4. Topography map of the crater created at the BHL 1003 event.

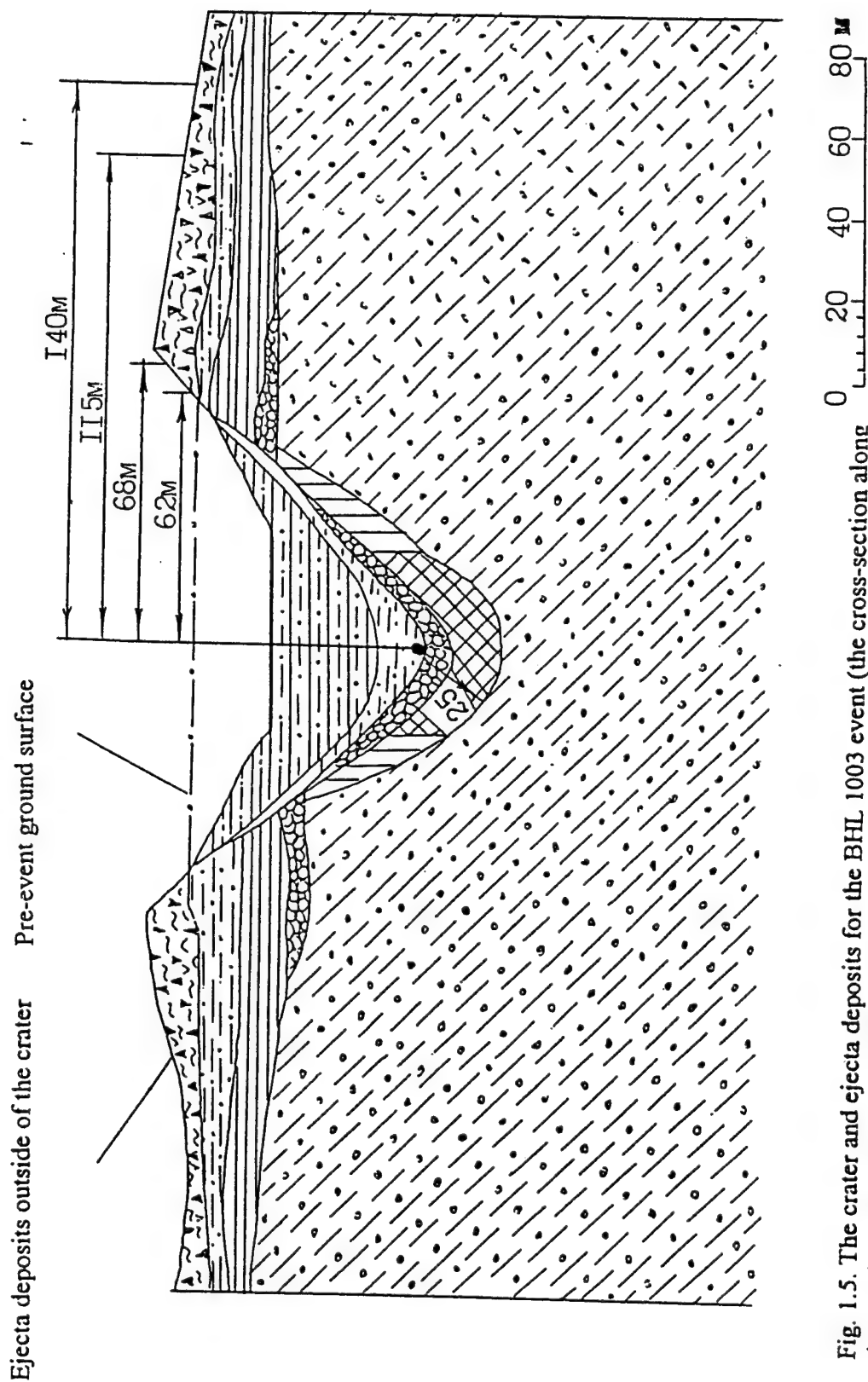
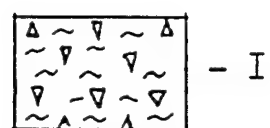
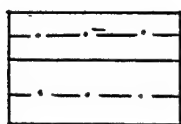


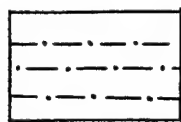
Fig. 1.5. The crater and ejecta deposits for the BHL 1003 event (the cross-section along the 1-1 direction shown at the Fig. 1.4).



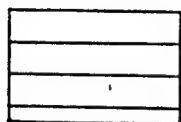
- I



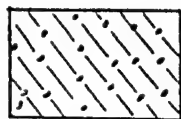
- 2



- 3



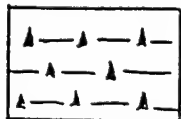
- 4



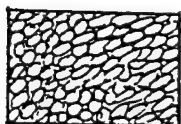
- 5



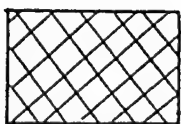
- 6



- 7



- 8



- 9

Legend for Fig.1.5.

- 1 - soil and loam
- 2 - gray-greenish and brown clay
- 3 - gray-greenish clay
- 4 - brown clay
- 5 - alevrolite
- 6 - diabasic porfirite
- 7 - clay with alevrolite fragments (up to 30 %)
- 8 - crashed alevrolite
- 9 - zone of rock failure

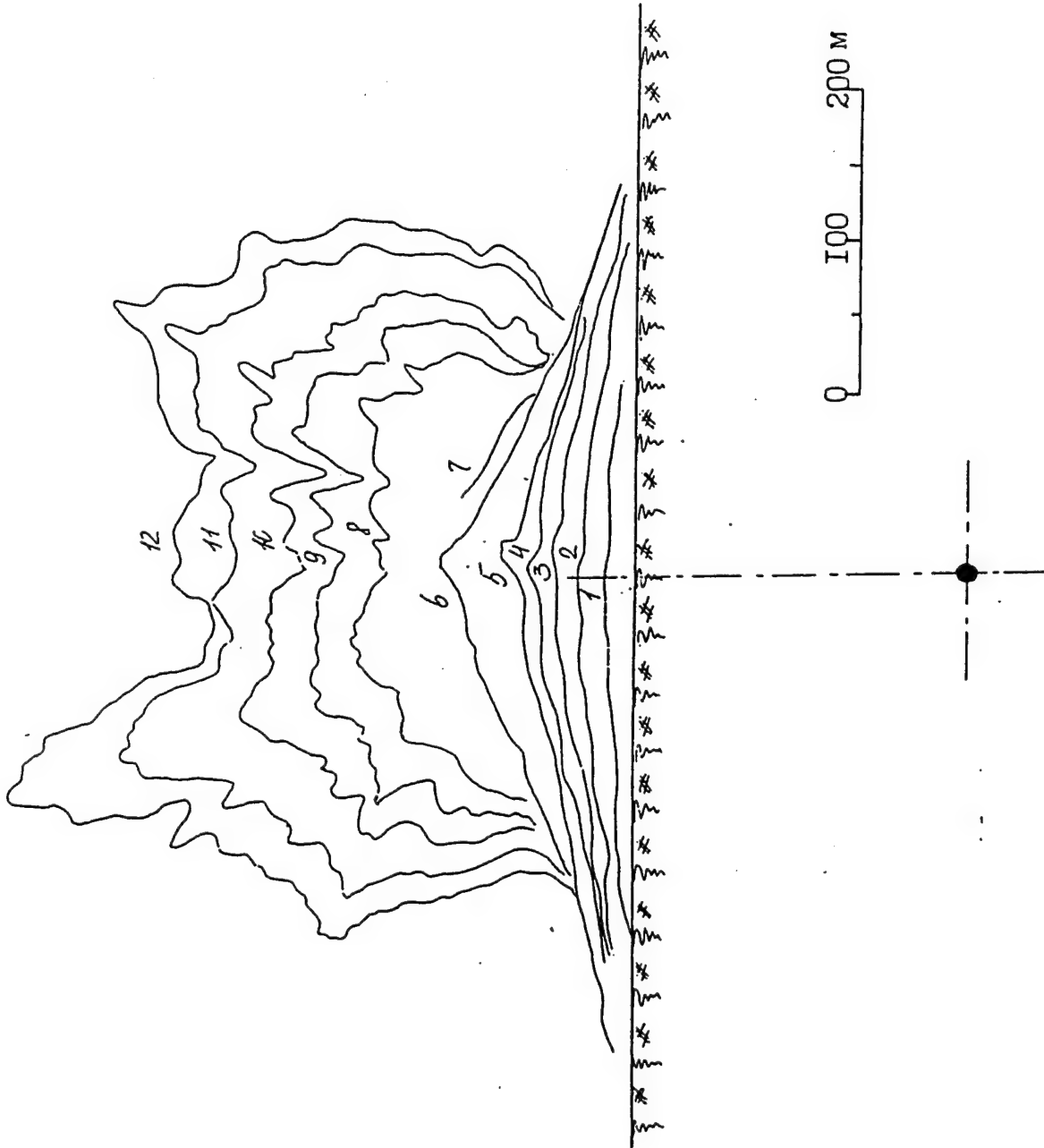


Fig. 1.6. The dome profile evolution at the BHL 101 event. Time marks in seconds.

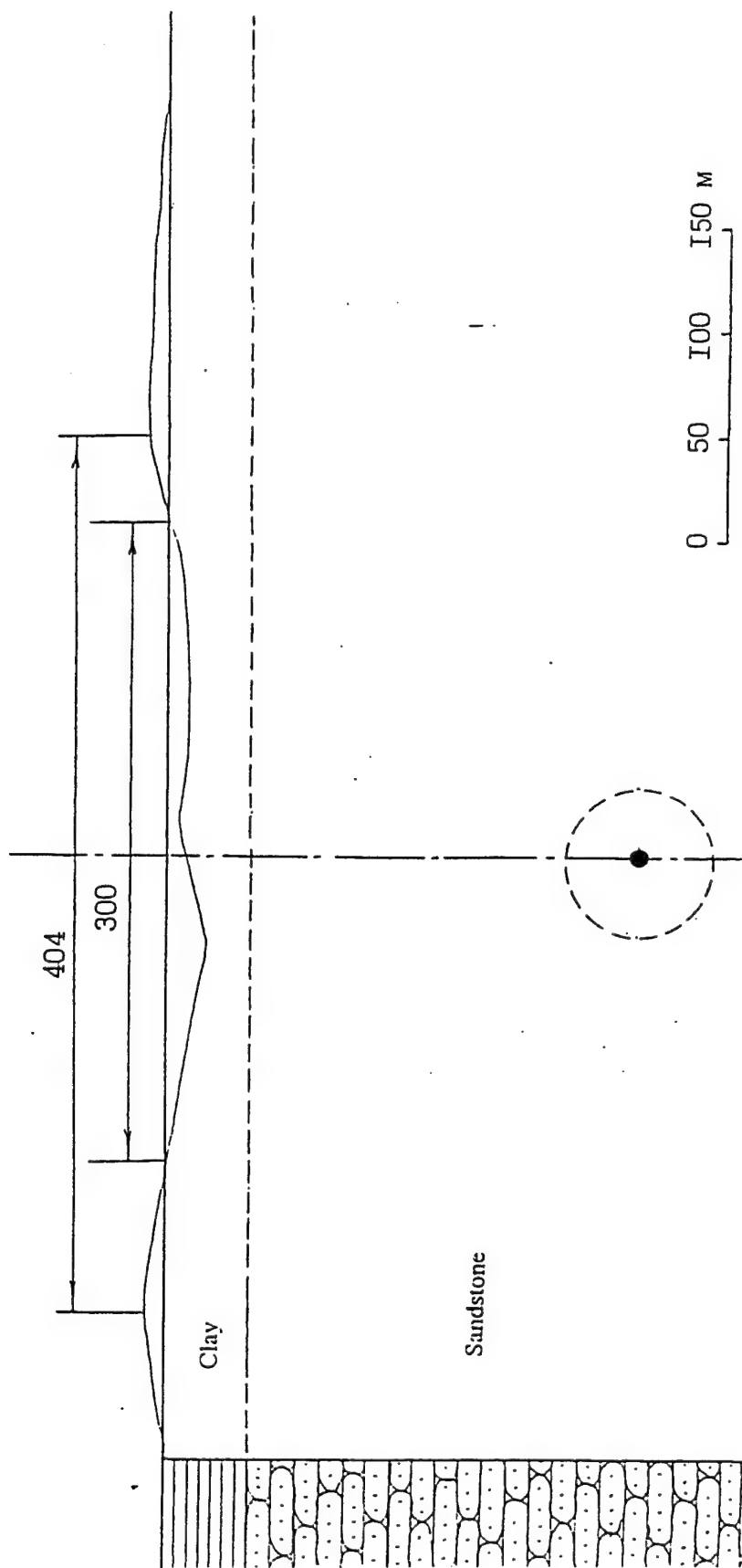


Fig. 1.7. The geological cross-section scheme for the BHL 101 event.

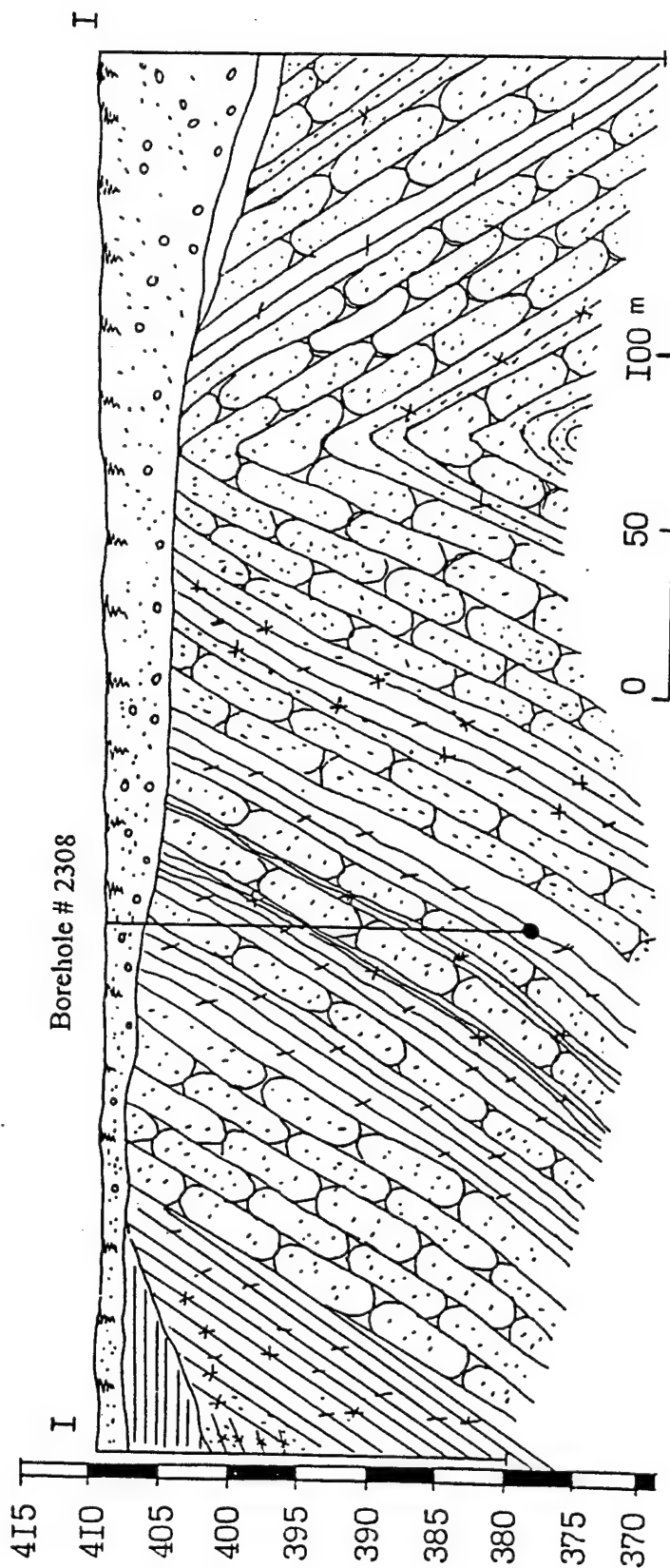
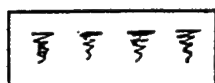


Fig. 1.8. The geologic cross-section along the I-I direction in the vicinity of the borehole #2308.

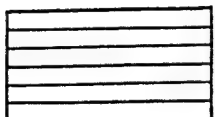
Fig.1.9. Legend for the Fig. 1.8.



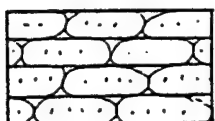
- soil (mostly sandy loam)



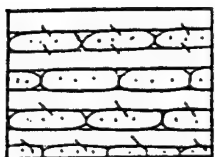
- gray sand of variable grain size, polymictic with the admixture of 10 to 12 % of fine gravel



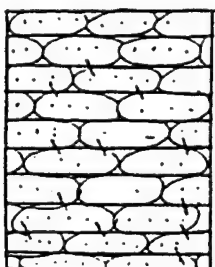
- Dark-gray clay with violet hue (weathered crust of argillite)



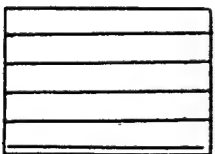
- Brownish-yellow sandstone, fine grained and weathered.



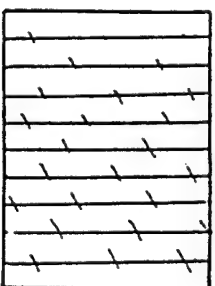
- Interlayering of dark-brown argillite with minor layers of yellowish-brown alevrolite. Thickness of interlayers is of 1.5 to 3 cm.



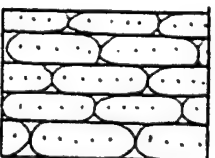
- Gray sandstone, fine grained with thin interlayers of dark-gray argillite and gravelite (thickness up to 2 mm). Angle of layering is 20° to 25° to the core axis. Rocks are slightly weathered and fractured. Fracture surfaces are covered with hydroxides of Fe and Mn.



- Brownish-gray sandstone of middle grain size, polymictic with the admixture of carbonaceous fragments (up to 4 %, size of 1.5 cm, rarely up to 3 cm).



- Dark-gray argillite, dense with slight banding at 70° to the core axis. The rock is fractured, with rusty fracture surfaces. The recovered core consists of cylinders of 5 to 15 cm length. At the depth interval from 32 to 34 m large rock fragments was observed. A large amount of organic materials was found at this depth interval.



- Gray argillite, of a middle grain size with interlayers of the fine-grained one. Angle of interlayers is about 70° to the core axis. One can find infrequently thread-like carbonate veins.

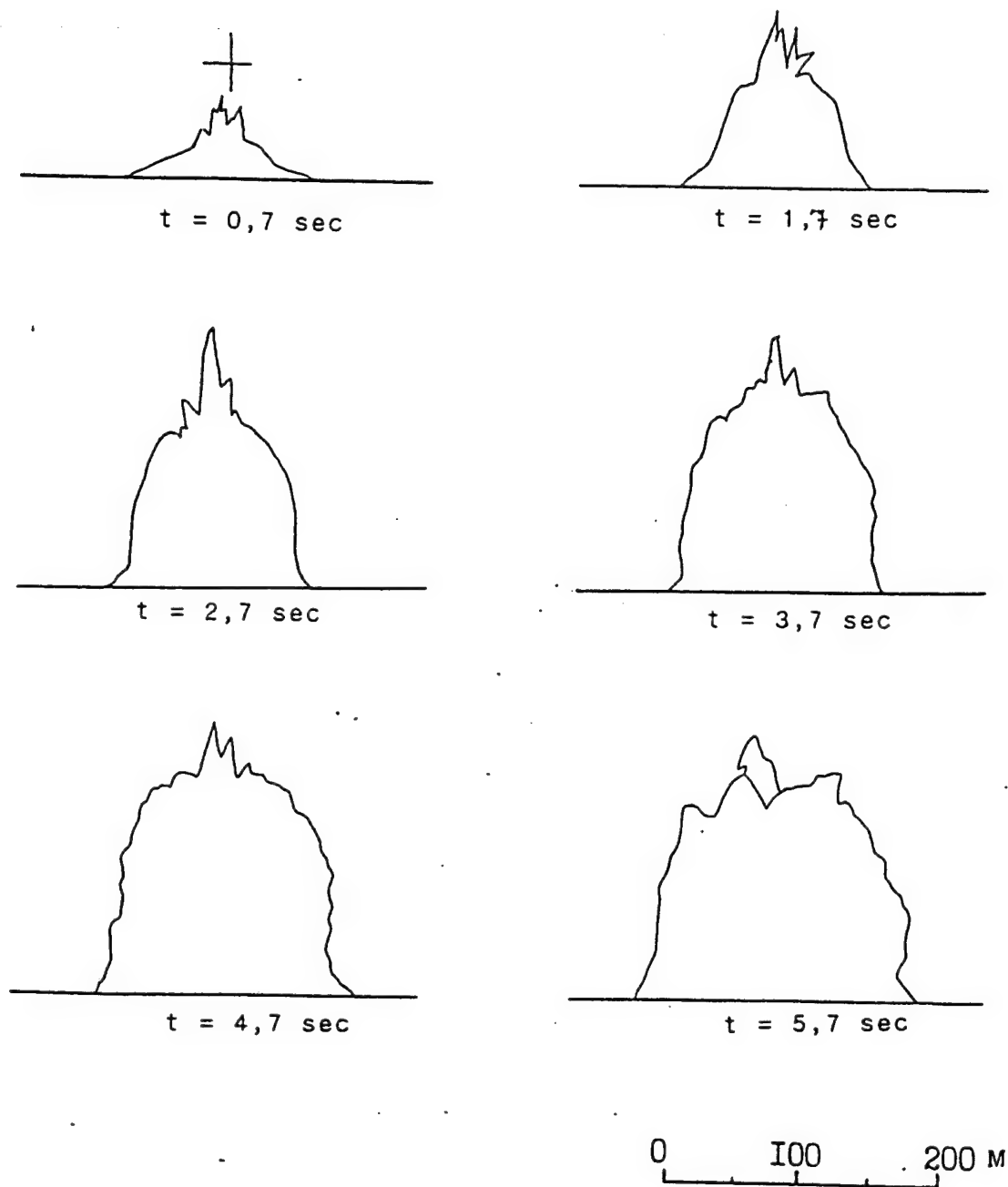
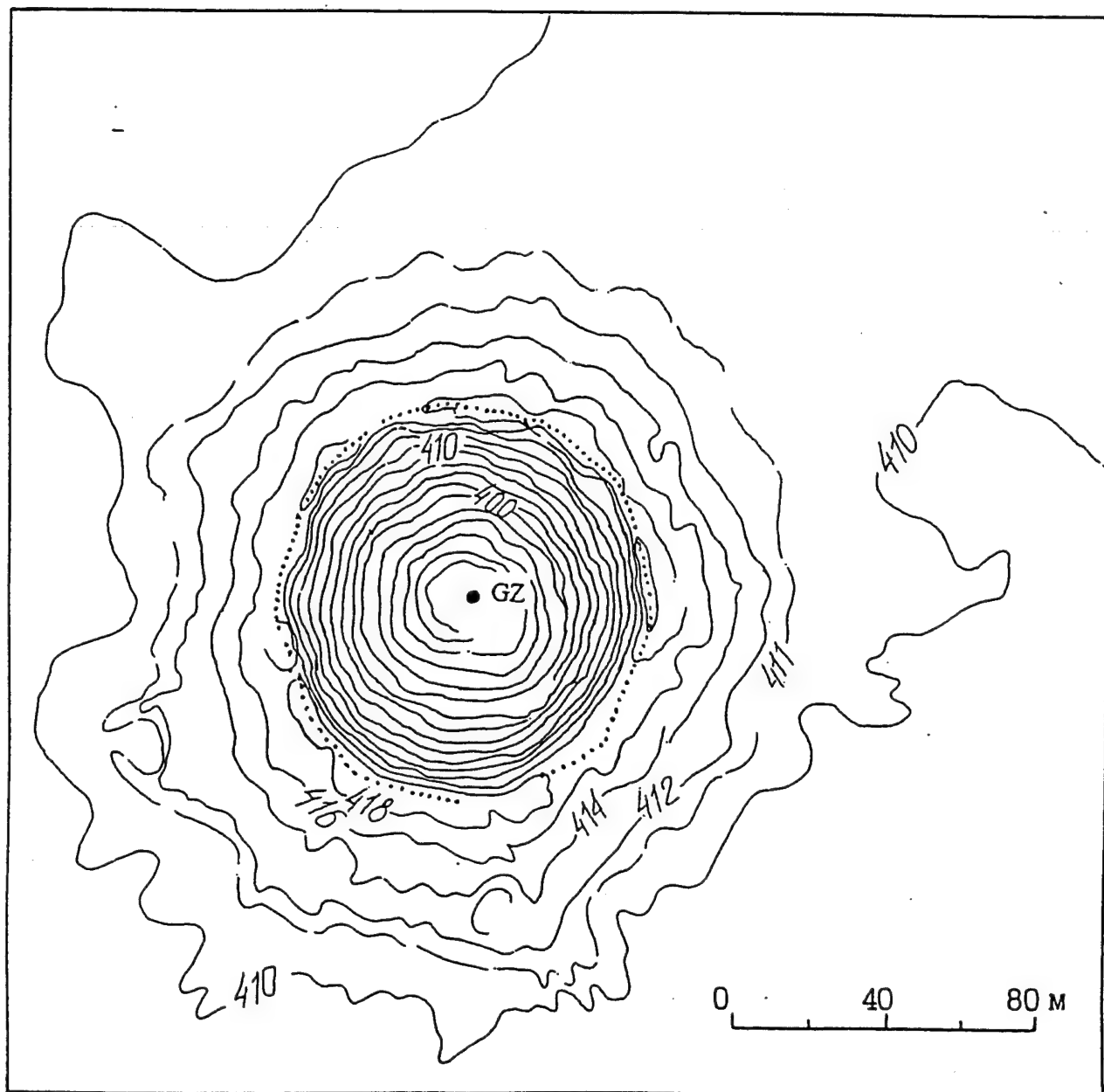
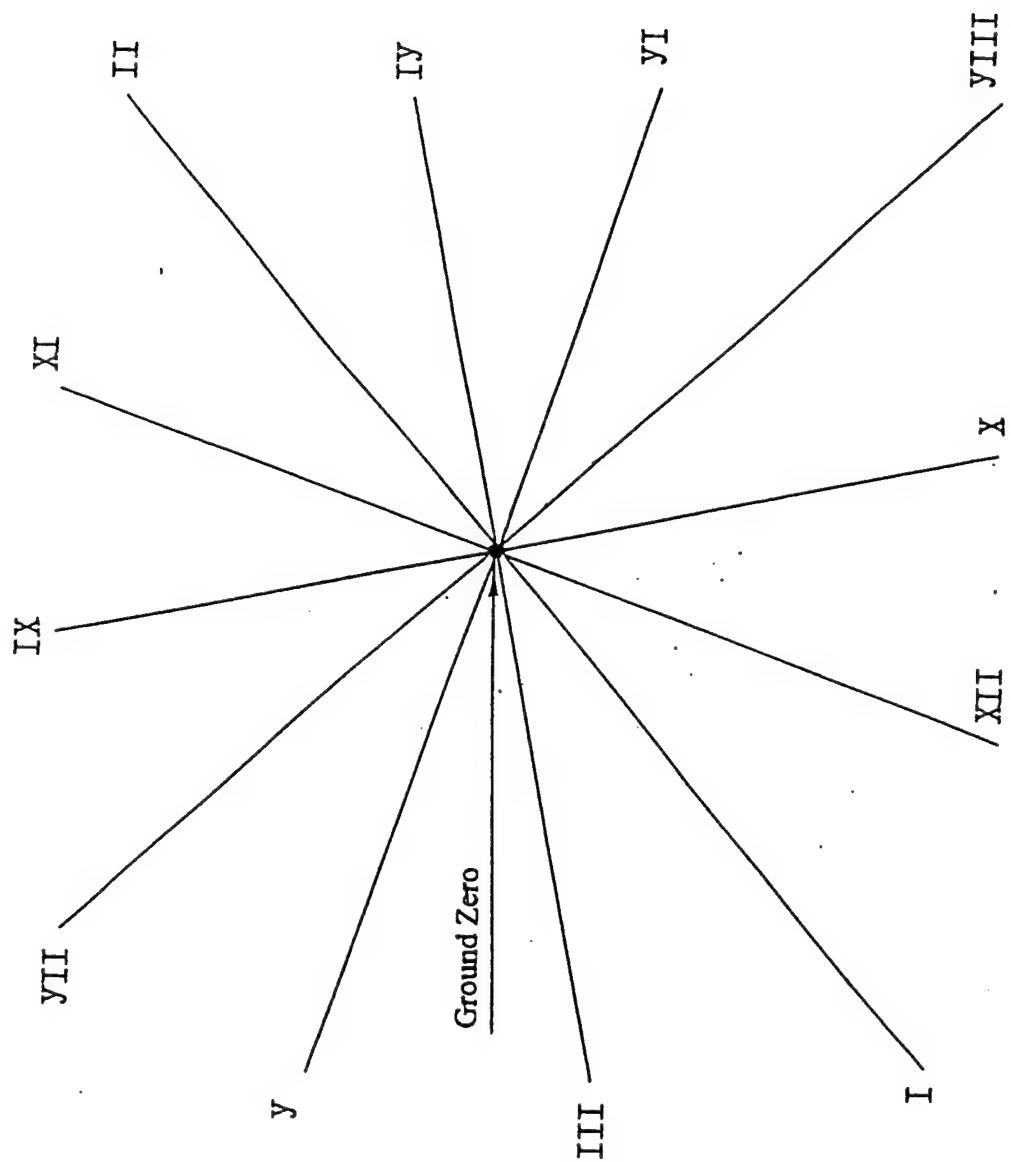


Fig. 1.10. Dome profiles at various moments of time at the T-1 event.



..... - Rim crest contour

Fig. 1.11. The topographic map of the T-1 crater.



The map of directions along which cross-sections are shown at Figs. 1.11 and 1.12.

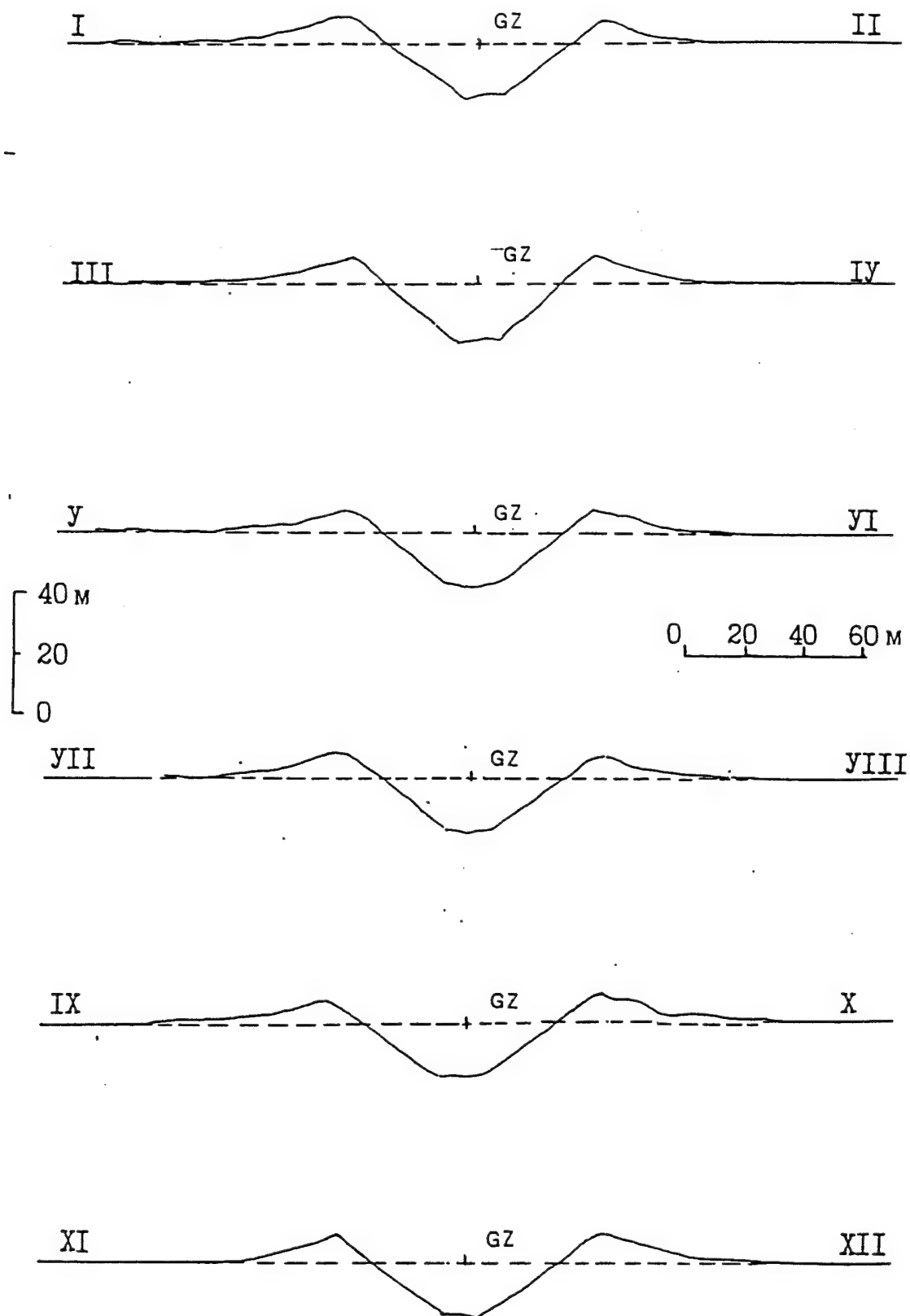


Fig. 1.12. Crater profiles along different directions.

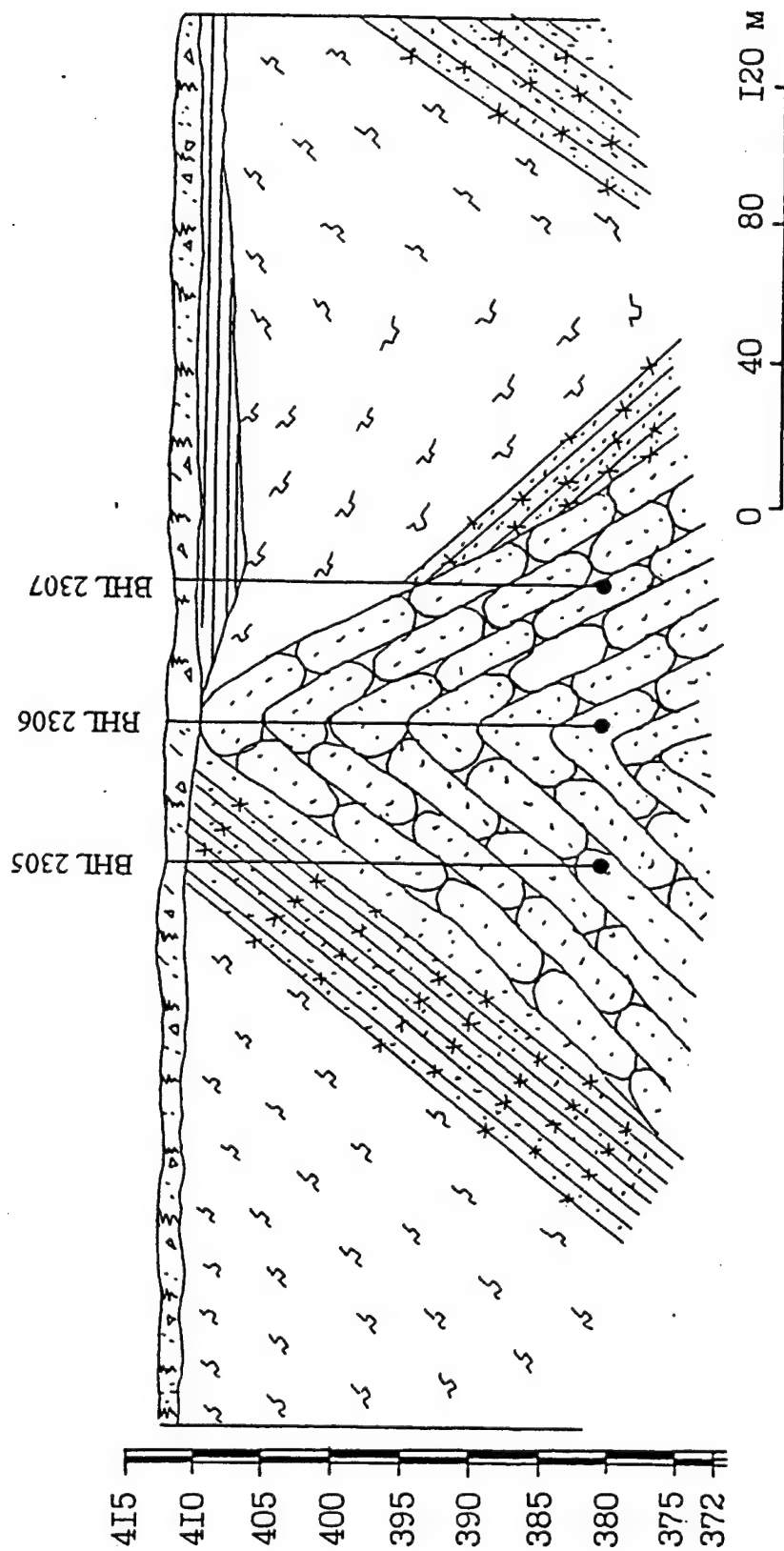
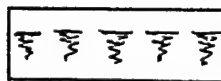
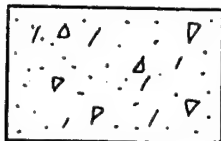


Fig. 1.13. The geologic cross-section along the line of ground zeros for the T-2 event.

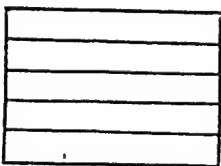
Fig. 1.14. Legend for Fig. 1.13.



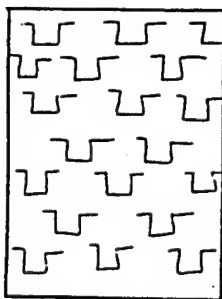
- soil (sandy loam)



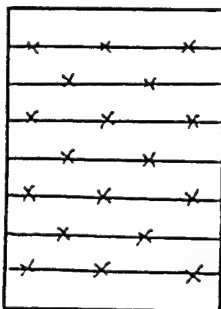
- coarse debris with rubble fragments, polimictic, with the matrix of dens gray lime sandy loam.



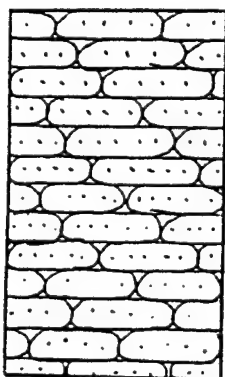
- Motley clay, with yellowish-brown and cherish-red patches. Plastic one.



- Weathered porfirite, of yellowish-brown color, highly fractured. Below the depth of 11.50 m the color is cherish-red. One see an intensive carbonatisation.



- Cherish-red alevrolite, cohesive, with rare interlayers (5 to 10 cm thick) of coarse-grain sandstone (polimictic one with siliceous matrix). It is highly fractured rock.



- Gravelite: gray, variable grain size, slightly rounded, polimictic, with cohesive siliceous matrix. The general color is cherish-red. At depth's intervals 26 to 29 m and 33 to 37 m rocks are highly fractured, angle of fractures are inclines at 15 to 20°. Fracture surfaces are covers with calcite.

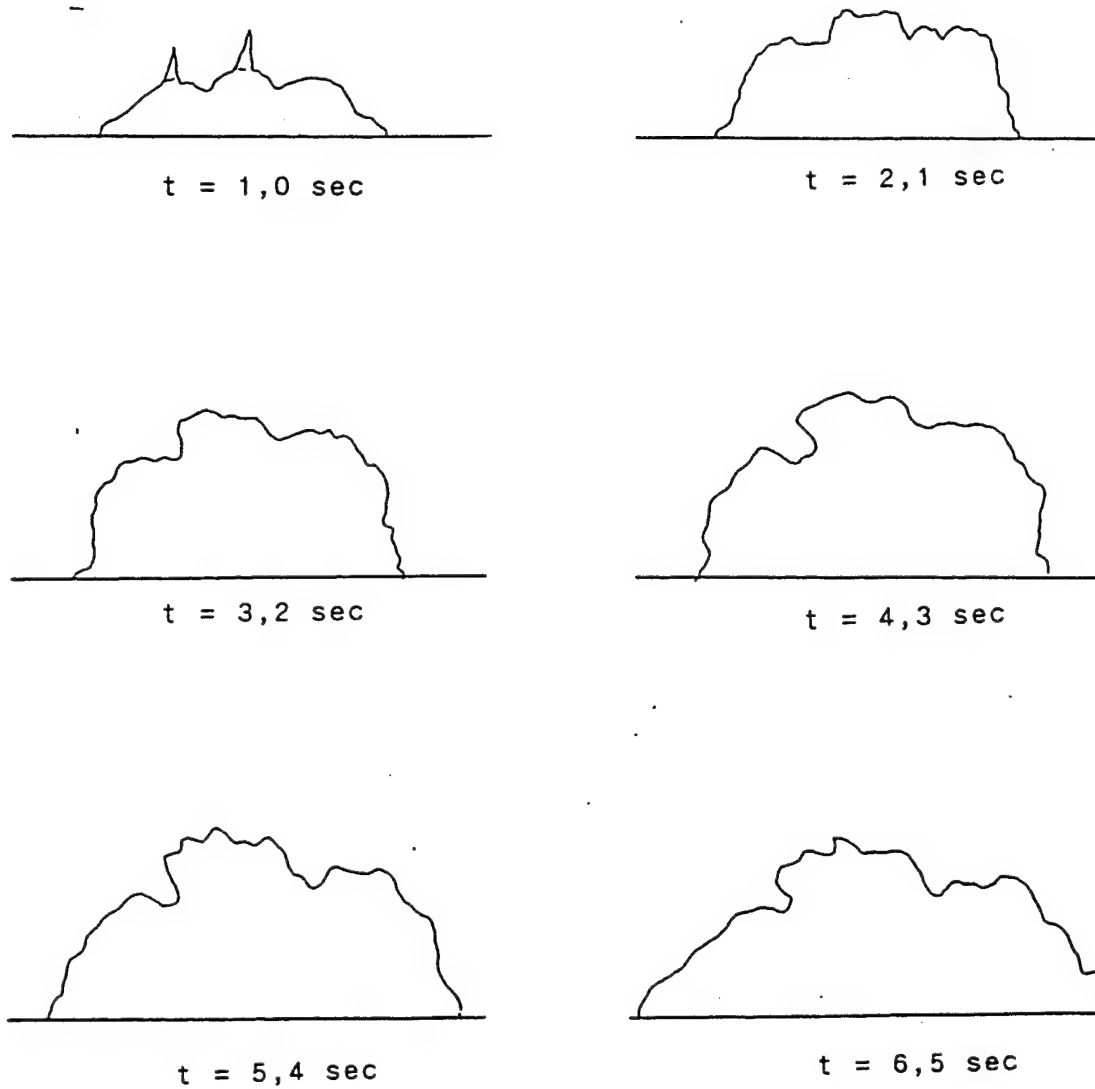
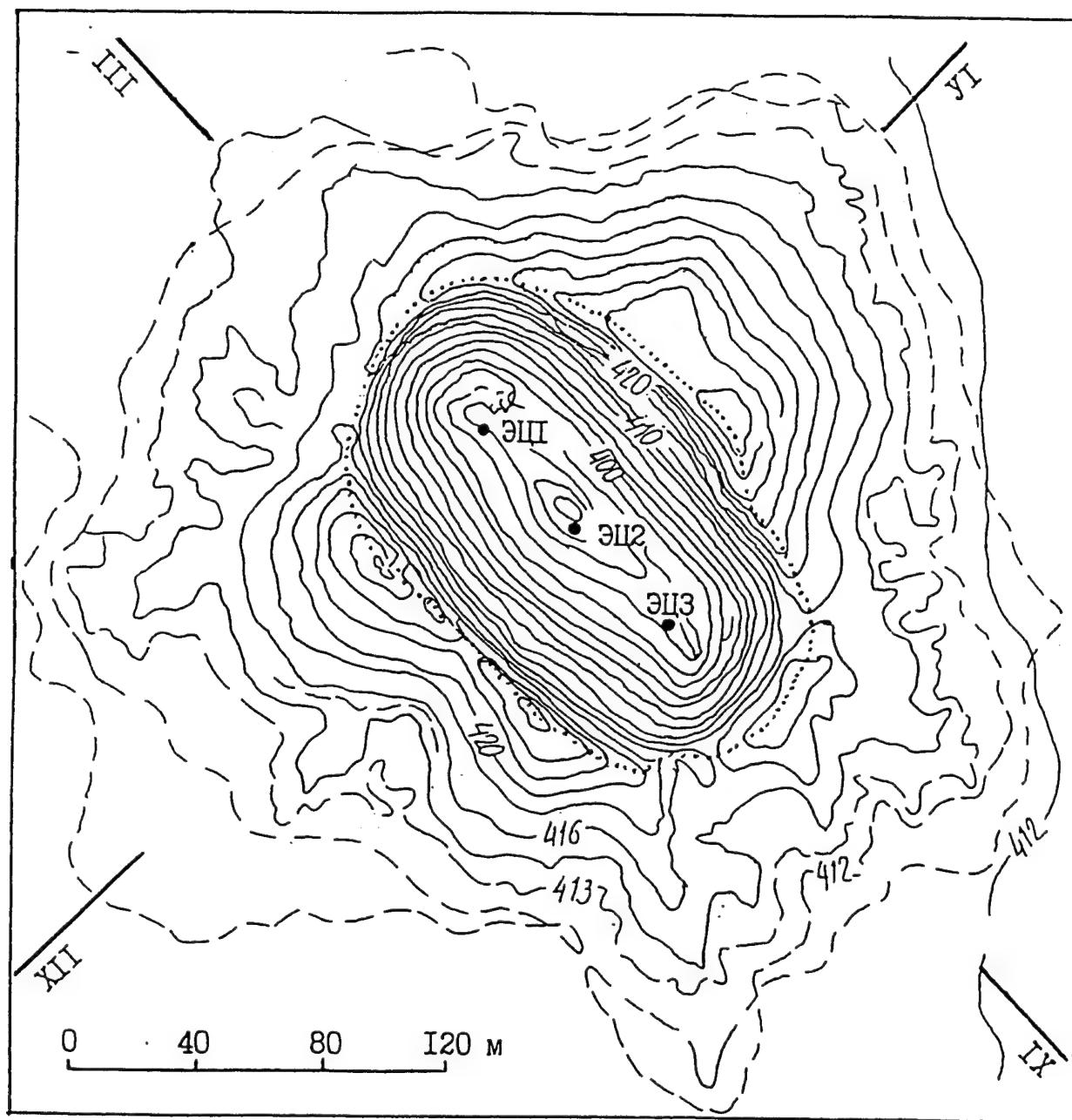


Fig. 1.15. The dome evolution at the T-2 explosion.



..... — Rim crest contour

----- — The outer boundary of ejecta deposits

Fig. 1.16. The topographic map of the elongated T-2 crater.

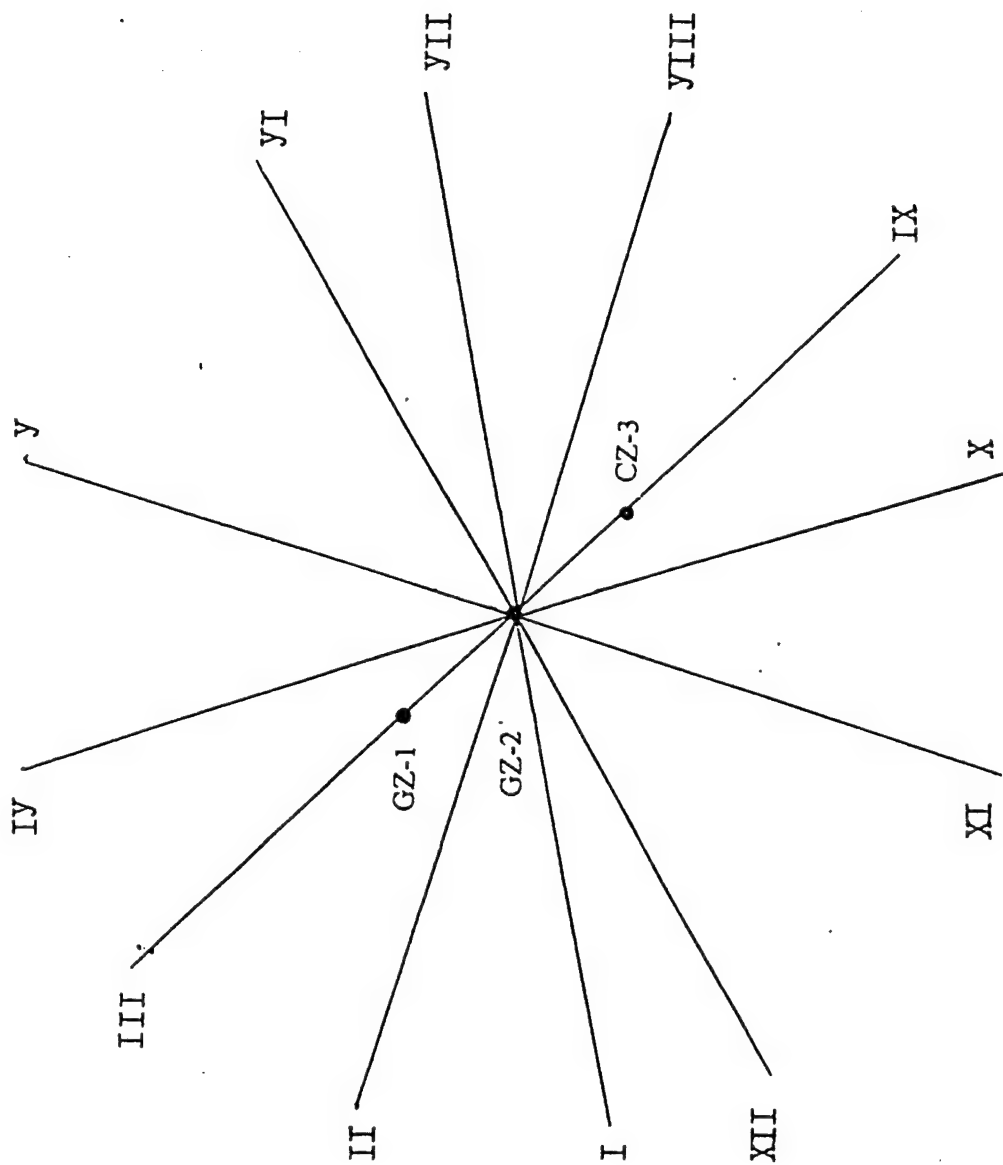


Fig. 1.17. The map of profile's directions.

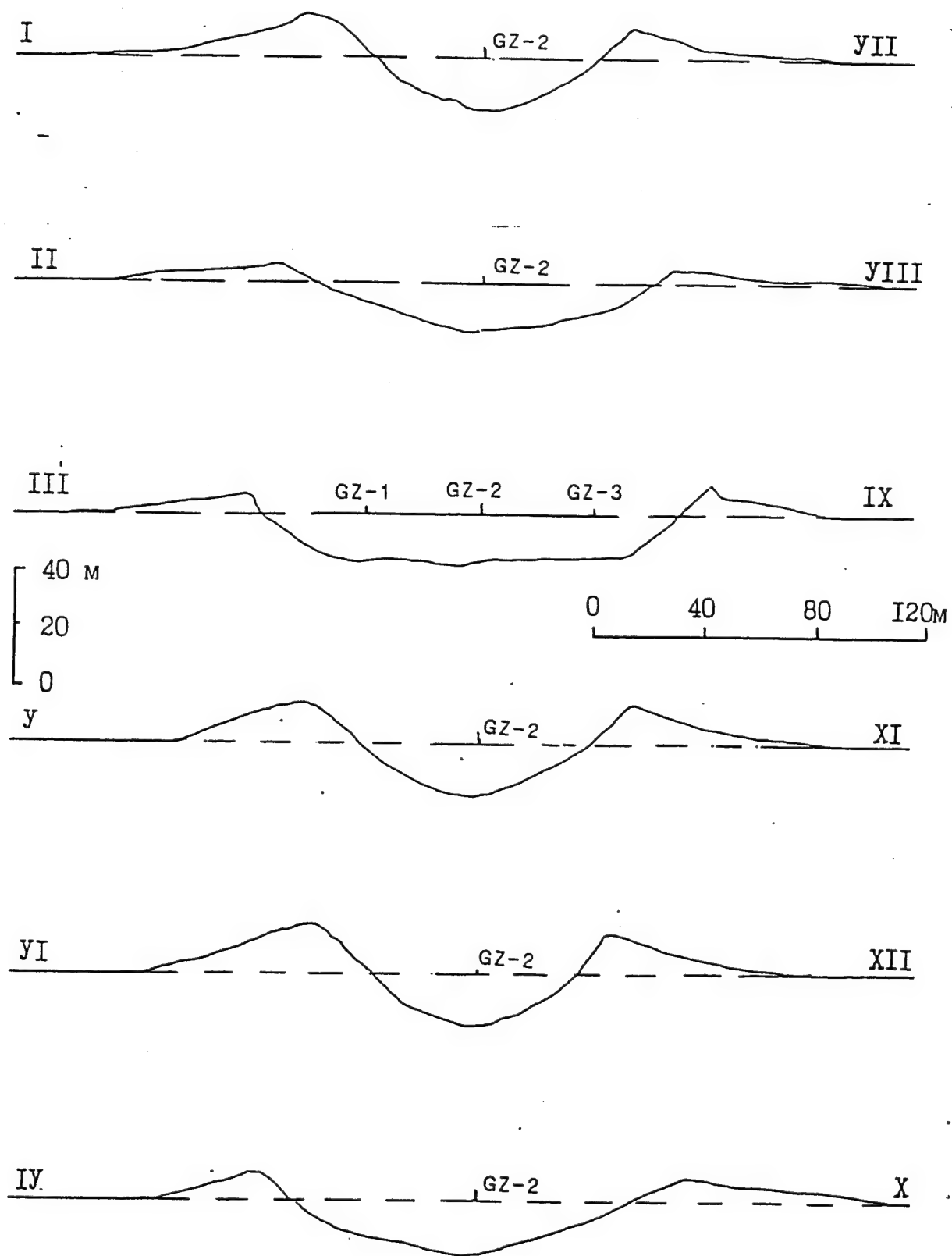


Fig. 1.18. Cross-sections of the elongated crater.

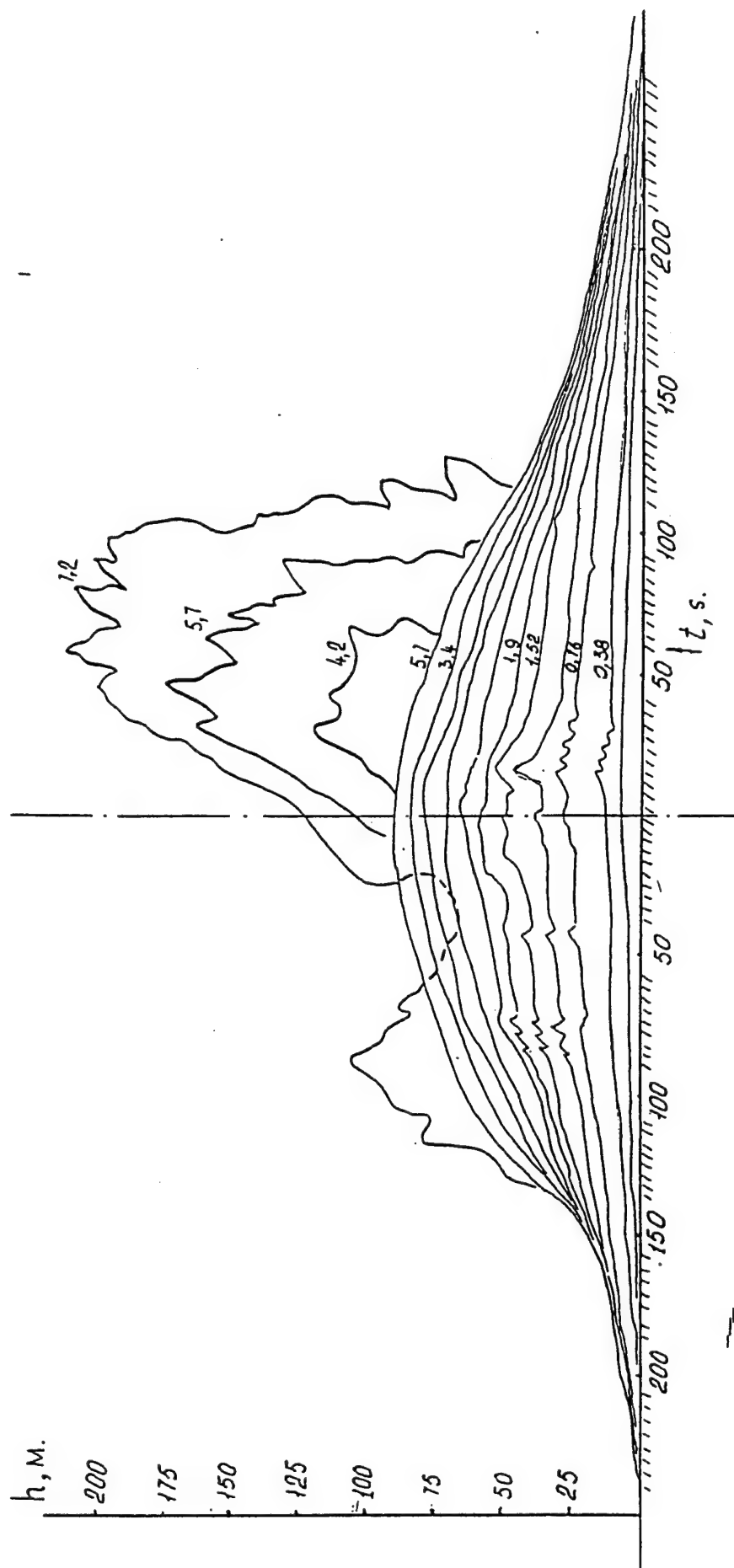


Fig. 1.19. The dome profile evolution at the BHL 125 event. Time marks in seconds.

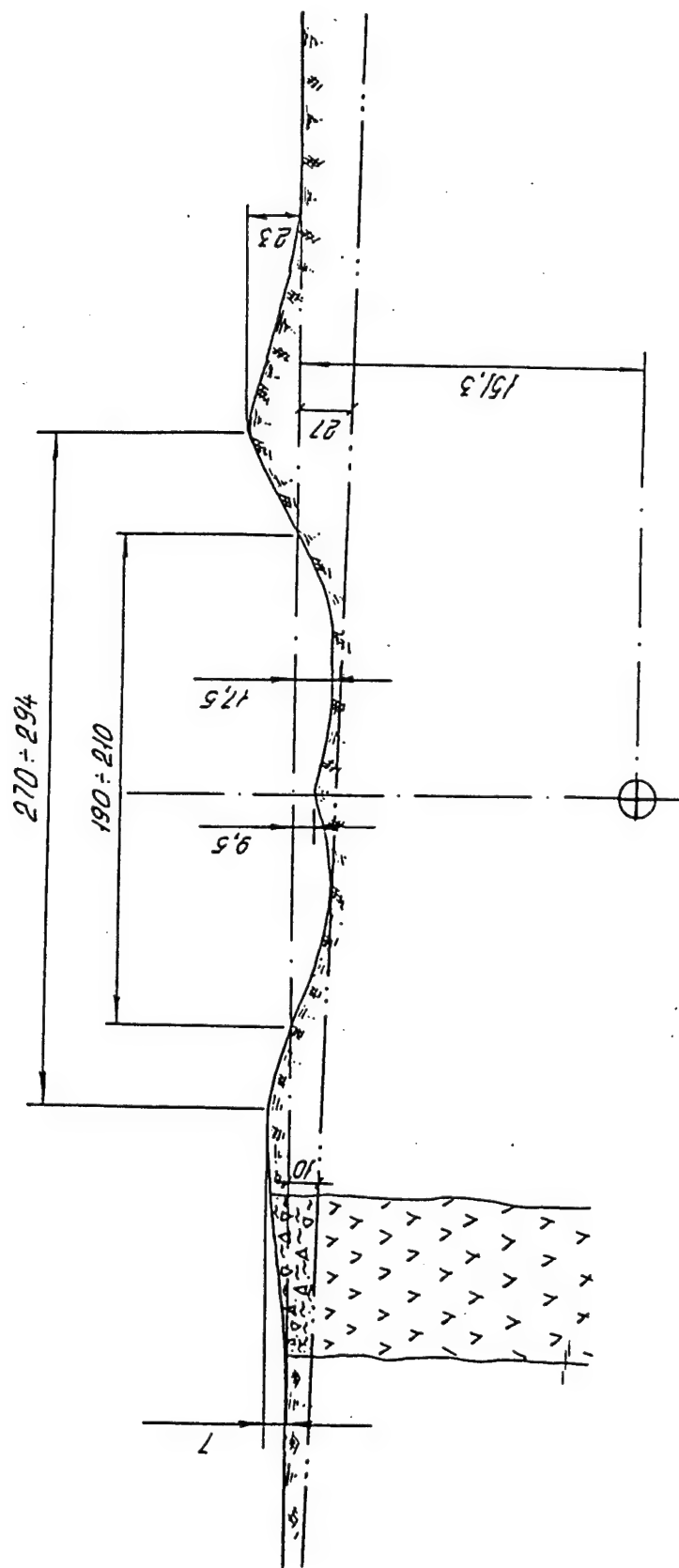


Fig. 1.20. The cross - section of crater for the BHL 125 event.

2. Near surface nuclear explosions

In the period 1953 to 1962 at the Semipalatinsk test site 12 near surface bursts was conducted. Explosion yields was from 0.3 to 450 kton. The general list of events is presented at the Table 2.1.

Table 2.1. List of near surface bursts.

Event #	Date	q, kton	HOB, m	Target rocks *)	H _{rock} , m **)	Average density kg m ⁻³
1	12.08.53	450	33	1	9.5	1700
2	05.10.54	4.0	0.5	3	5 to 6	1980
3	29.07.55	1.3	2.1	1	20	1800
4	02.08.55	11.6	2.1	1	20	1800
5	05.08.55	1.7	2.1	1	20	1800
6	25.03.56	5.5	1	4	7	2110
7	16.03.56	14.3	1	5	3	2380
8	09.09.61	0.5	0.5	1	20	1850
9	14.09.61	0.3	0.5	1	20	1850
10	07.08.62	10	0.5	5	3	2290
11	25.09.62	7	0.5	2	-	1900
12	26.11.62	1.1	0.5	1	22	1850

*) Target rocks:

- 1 - soft soil
- 2 - soft soil (clayish deposits)
- 3 - soft soil layer over quartzite
- 4 - soft soil layer over highly fractured quartzite
- 5 - soft soil layer over fractured quartzite

**) H_{rock} is the depth of basement rocks (or surface soft layer thickness). For events ## 2, 6, 7, and 10, basement rocks are presented by highly fractured quartzite, fractures are filled with water.

In tables q is the explosion yield, HOB is the height of the device's center of gravity.

Table 2.2 summarizes dimensions of craters and crater's rims for near-surface bursts. Listed parameters are:

- Crater radius at the pre-event surface;
- Crater depth below at the pre-event surface;
- Crater volume at the pre-event surface;
- R_{rim} is the rim crest crater radius;
- H_{rim} is the average rim crest height;
- R_{ced} is the continuous ejecta deposit outer radius;
- R_{su} is the radius of a maximum structural uplift;
- H_{su} is the height of the structural uplift (averaged on azimuths);

Meanings of these parameters are shown for a typical crater on Fig. 2.2. Profiles of craters along different azimuths and map schemes are shown on Figs. 2.2 - 2.10.

Table 2.2. Crater dimensions of near surface bursts.

Event #	q, kton	HOB, m	Crater radius, m	Crater depth, m	Crater volume m ³	R _{rim} , m	H _{rim} , m	R _{ced} , m	R _{su} , m	H _{su} , m
1	450	33	11.5	2.4	500		-1.6	45		
2	4.0	0.5	20.5	7.9	4940	24.8	1.64	90	50	1.26
3	1.3	2.1	7.25	3.7	240	9	0.4	12.8	12.8	0.4
4	11.6	2.1	26	11	10700	31.8	2.45	88	65	2.26
5	1.7	2.1	10.75	5.8	840	12.5	0.85	18	18	0.85
6	5.5	1	25	12.5	11200	27.5	2.9	37	50	
7	14.3	1	32.3	17.6	24150	41.8	3.4	112		
8	0.5	0.5	10	5.5	860	12.5	1.25	17.8		
9	0.3	0.5	6.25	3.5	215	12.5	0.75	6 to 13		
10	10	0.5	22	9.9	5050	28.6	2.09	97	45	1.2
11	7	0.5	21.3	8.35	5560	27.7	1.9	130	46.5	1.45
12	1.1	0.5	13.5	7.25	1410	16.8	1.03	67	38	0.8

Comments: R_{rim} is the rim crest radius, H_{rim} is the rim height, R_{ced} is the continuous ejecta deposit radius, R_{su} is the structural uplift radius, H_{su} is the height of the structural uplift.

The data of geological cites for some (not all) events are listed below in separated tables, marked with the event number. "a" is the longitudinal seismic wave velocity. Strength coefficient (Protodiakonov Strength Coefficient) is the value of unconfined compressive strength, measured in special units: 1 unit = 100 bar..

#1	Thickness, m	a, m/s	Density, kg m ⁻³	Strength coefficient
Heavy sandy loam	0.8	230	1700	0.8
Sand with 15 % of gravel	1.4	420	1700	0.6
Gravel with sand and pebbles	1.9	400	1900	0.8
Loam with pebbles	1.9	600	1800	0.5
Pebbles and cobbles	3.3	1000	1900	2
Shale	6.9	2000	2100	4
Strong sandstone	3.3	2200	2200	8
Shale	> 10	2500	2200	6

##3 and 5	Thickness, m	a, m/s	Density, kg m ⁻³	Strength coefficient
Loam with pebbles	0.5	-	1690	-
Sandy loam with pebbles	1.5	-	1880	-
Gravel	2.5	-	1870	-
Loam with pebbles	1.5	-	1670	-

##8, 9, 12	Thickness, m	a, m/s	Density, kg m^{-3}	Strength coefficient
Sandy loam , sand with clay	0.5	300	1700	0.8
Sandy loam , sand with clay	2	400	1850	0.95
Sandy loam , sand with clay	4.1	600	1850	1.10
Sandy loam , sand with clay	0.4	600-	1850	1.10
Sandy loam , sand with clay	9	800	1900	1.22
Sandy clay	8	1200	2000	1.22
Shale	-	2500	2200	1.46

# 7, 10	Thickness, m	a, m/s	Density, kg m^{-3}	Strength coefficient
Loam with gravel and pebbles	3	-	1800	-
Fractured quartzite	>15	-	2500	-

#11	Thickness, m	a, m/s	Density, kg m^{-3}	Strength coefficient
Highly sanded clay	>8.4	-	1900	-

# 6	Thickness, m	a, m/s	Density, kg m^{-3}	Strength coefficient
Sandy loam with sand	1.1	350	1800	0.8
Sand with gravel	3.9	550	1800	0.8
Clay	9.5	550	1800	1.5
Clay	2.5	550	1800	1.5
Water saturated quartzite	>5	500	2500	6.0

# 2	Thickness, m	a, m/s	Density, kg m^{-3}	Strength coefficient
Loam	0.8	-	1690	-
Gravel	2	-	1760	-
Loam	0.2	-	1710	-
Sandy loam with pebbles	1.0	-	1690	-
Gravel	1.0	-	1770	-
Quartzite	>2.9	-	2400	-

#4	Thickness, m	a, m/s	Density, kg m^{-3}	Strength coefficient
Loam with pebbles	0.5	-	1690	-
Sandy loam with pebbles	1.5	-	1880	-
Gravel	2.5	-	1870	-
Loam with pebbles	1.5	-	1640	-
Loam with pebbles	>5	-	1800	-

Topographic measurements of crater rims and ejecta deposits was done several years after explosions for some (not all) craters. These data are summarized below as separated

tables, marked with the event number. Tables contain azimuth number, radial distance from the ground zero, R , the measured height of the structural uplift of the pre-event surface, h_{su} , m, and thickness of ejecta deposits, h_e , m. Close to the rim crest ejecta was absent at the time of measurements, but it not obvious, were they never deposited here or been eroded in the period of the event and topo measurements.

Surface burst #/2

Azimuth #, m	1		2		3		4		5		6		7		8		Density g/cc
	h_{SN} , m	h_e , m	h_{SN} , m	h_e , m	h_{SN} , m	h_e , m	h_{SN} , m	h_e , m	h_{SN} , m	h_e , m	h_{SN} , m	h_e , m	h_{SN} , m	h_e , m	h_{SN} , m	h_e , m	
24	1.42		1.45		2.38		1.5		0.8	0.23	1.47		1.6		1.32		1.7
25	1.3	0.33	1.3	0.24	2.6	0.33	1.55		0.62	0.13	1.4	0.23	2.03		1.12	0.49	1.7
30	0.8	0.07	1.4	0.27	1.95	0.1	1.35	0.65	0.36	0.17	0.5	0.13	1.47	0.42	0.58	0.25	1.7
35	0.38			0.08	0.72	0.09	0.27	0.13		0.12	0.18	0.09	0.64	0.14		0.12	1.7
40		0.12		0.09	0.4	0.12		0.07		0.1		0.1	0.43	0.12		0.11	1.7
45		0.2		0.06	0.24	0.09		0.05		0.07		0.1	0.22	0.06		0.08	1.5
50		0.08		0.06		0.06		0.08		0.11		0.13	0.06	0.04		0.07	1.5
55		0.14		0.05		0.09		0.09		0.05		0.09		0.08		0.07	1.5
60		0.07		0.05		0.06		0.09		0.06		0.11		0.03		0.05	1.5
65		0.1		0.05		0.06		0.1		0.06		0.08		0.06		0.06	1.5
70		0.29		0.03		0.03		0.06		0.04		0.12		0.07		0.04	1.5
75		0.2		0		0		0.06		0.03		0.09		0.05		0.04	1.5
80		0.05		0		0		0.06		0.02		0.08		0.03		0.04	1.5
85		0.03		0		0		0.05		0		0.06		0.05		0.04	1.5
90		0		0		0		0.06		0		0.04		0.05		0	1.5

Surface burst #4

Azimuth #	1		2		3		4		5		6		7		8		Density g/cc
	h_{SD}, m	h_e, m	h_{SD}, m	h_e, m	h_{SD}, m	h_e, m	h_{SD}, m	h_e, m	h_{SD}, m	h_e, m	h_{SD}, m	h_e, m	h_{SD}, m	h_e, m	h_{SD}, m	h_e, m	
32	4.22	0	3.37		2.25	0.05	1	0.4	1.62		2.93	0.2	1.24	0.1	2.6		1.7
35	3.52	0	3.2		1.8	0.03	0	0.34	1.6	0.23	1.41	0.1	0.96	0.1	2	0.2	1.7
40	2.2	0.07	2.4	0.8	0	0.08	0	0.15	1.25	0.71	0.5	0.35	0.6	0.14	0.92	0.18	1.7
45	0.75	0.03	1.16	0.54	0	0.06	0	0.12	0.7	0.35	0	0.18	0.47	0.15	0.72	0.14	1.7
50	0	0.27	0.52	0.45	0	0.1	0	0.11	0.43	0.22	0	0.13	0.33	0.11	0.6	0.09	1.7
55	0	0.15	0.4	0.36	0	0.12	0	0.09	0.36	0.29	0	0.1	0	0.22	0.55	0.09	1.5
60	0	0.18	0	0.21	0	0.22	0	0.08	0.25	0.1	0	0.14	0	0.17	0.48	0.04	1.5
65	0	0.18	0	0.17	0	0.1	0	0.09	0	0.1	0	0.1	0	0.1	0.35	0.04	1.5
70	0	0.05	0	0.2	0	0.08	0	0.07	0	0.12	0	0.1	0	0.07	0.2	0.04	1.5
75	0	0.04	0	0.1		0.06		0.08		0.1		0.08		0.09		0.06	1.5
80				0.04		0.07		0.04		0.04				0.1		0.03	1.5
85				0.15		0.06								0.08			1.5
90				0.03		0.05								0.04			1.5

Surface burst #7

Azimuth #	1	2	3	4	5	6	7	8	Density
R.m	$h_{rim, m}$	$h_{rim, m}$	$h_{rim, m}$	$h_{rim, m}$	$h_{rim, m}$	$h_{rim, m}$	$h_{rim, m}$	$h_{rim, m}$	g/cc
43	4.85	2.84	4.08	3.05	4.47	1.54	3.35	1.07	2
45	4.53	2.1	3.56	2.98	4.23	1.5	3.2	1.07	2
47	4.2	1.7	3.28	2.9	4	1.6	2.7	1.07	2
50	3.45	1.25	2.9	2.67	3.24	1.72	1.85	0.84	2
53	3.15	0.9	2.55	2.24	2.72	1.66	1.5	0.4	2
56	2.42	0.65	1.95	1.65	1.85	1.5	1.5	0.27	2
60	0.38	0.45	1.35	1.26	0.97	0.61	1.35	0.45	2
63	0.35	0.17	0.95	0.3	0.23	0.5	1.23	0.4	2
65	0.19	0.08	0.49	0.23	0.16	0.42	0.51	0.36	1.8
75	0.08	0.09	0.28	0.24	0.13	0.28	0.29	0.17	1.8
80	0.1	0.11	0.32	0.11	0.08	0.17	0.1	0.16	1.8
85	0.09	0.16	0.27	0.04	0.06	0.3	0.06	0.06	1.8
90	0.06	0.1	0.08	0.05	0.06	0.06	0.1	0.23	1.8
95	0.09	0.18	0.04	0.03	0.03	0.04	0.08	0.23	1.8
100	0.08	0.13	0.06	0	0	0.03	0.03	0.18	1.8
105	0.03	0.14	0.06	0	0	0	0	0.06	1.8
110	0	0.13	0.03	0	0	0	0	0.03	1.8

Surface burst #10

Azimuth #	1		2		3		4		5		6		7		8		Density g/cc
	h_{su}, m	h_e, m	h_{su}, m	h_e, m	h_{su}, m	h_e, m	h_{su}, m	h_e, m	h_{su}, m	h_e, m	h_{su}, m	h_e, m	h_{su}, m	h_e, m	h_{su}, m	h_e, m	
30	1.7		1.5		1.3		1.54	0.52	3.12		1.4	0.65	2.8		1.2		1.95
32	2.45		0.97		1		1.46	0.52	3.05		1.2	0.55	2.17		1.15		1.95
38	1.11		0.83		0.57	0.2	1.08	0.46	0.8		0.45	0.2	1		0.55		1.95
40		0.48		0.6		0.24		0.34				0.14		0.69	0.47		1.95
45		0.6		0.36		0.24		0.22				0.1		0.4	0.28		1.8
50		0.31		0.15		0.14		0.26				0.12		0.37		0.22	1.8
65		0.16		0.12		0.1		0.12				0.09		0.21		0.08	1.8
70		0.12		0.14		0.08		0.08				0.12		0.15		0.08	1.8
85		0.08		0.08		0.05		0.04				0		0.11		0.08	1.8
95		0.06		0.16		0		0				0		0.04		0	1.8
100		0		0.05		0		0				0		0		0	1.8

Surface burst #11

Azimuth #	1		2		3		4		5		6		7		8		Density g/cc
	h_{SN} , m	h_e , m	h_{SN} , m	h_e , m	h_{SN} , m	h_e , m	h_{SN} , m	h_e , m	h_{SN} , m	h_e , m	h_{SN} , m	h_e , m	h_{SN} , m	h_e , m	h_{SN} , m	h_e , m	
27	1.8		1.95		1.8		2.18	0.4	1	0.35	1.78		2.08		2		1.7
28	1.66		1.7		1.8		2.3	0.35	1.1	0.35	1.57		1.94		1.76		1.7
30	1.3		1.17		1.6		2.48	0.35	1.5	0.3	1.12		1.3		1.12		1.7
35	1.5		0.43		0.92		1.07	0.3	0.55	0.25	0.32		1.07		0.81		1.5
40	0.7		0.4		0.3		0.25	0.24	0.45	0.18	0.48		0.5		0.42		1.5
45		0.27		0.22		0.15		0.17		0.18		0.32		0.52		0.3	1.5
50		0.15		0.1		0.2		0.1		0.33		0.2		0.3		0.28	1.5
55		0.26		0.12		0.15		0.15		0.32		0.14		0.12		0.23	1.5
65		0.2		0.07		0.12		0.1		0.18		0.07		0.08		0.1	1.5
70		0.12		0.08		0.18		0.08		0.2		0.08		0.09		0.08	1.5
120		0.04		0.08		0.04						0.03		0.04			1.5

Surface burst #12

Azimuth #	1		2		3		4		5		6		7		8		Density g/cc
	h_{SN} , m	h_e , m	h_{SN} , m	h_e , m	h_{SN} , m	h_e , m	h_{SN} , m	h_e , m	h_{SN} , m	h_e , m	h_{SN} , m	h_e , m	h_{SN} , m	h_e , m	h_{SN} , m	h_e , m	
R_c , m																	
17			1.85		0.9		0.48		1.2		0.7	0	0.47	0	0.75	0	1.75
20	0.26	0.18	1.65	0.1	0.84	0.23	0.67	0.05	0.93	0.1	0.55	0	0.55	0	1	0	1.75
25	0.2		0.22	0.1	0.53	0.1	0.25	0.12	0.3	0.1	0.3	0.13	0.36	0		0.08	1.75
30		0.12	0.2	0.15	0.32	0.06	0.2	0.14	0.18	0.12	0.14	0.08	0.15	0.08		0.07	1.5
35		0.08		0.1	0.2	0.07	0.17	0.11	0.15	0.1		0.08	0.1	0.06		0.07	1.5
40		0.1		0.08	0.08	0.06	0.1	0.06	0.1	0.08		0.08		0.08		0.08	1.5
45		0.11		0.09		0.04		0.06		0.05		0.06		0.08		0.03	1.5

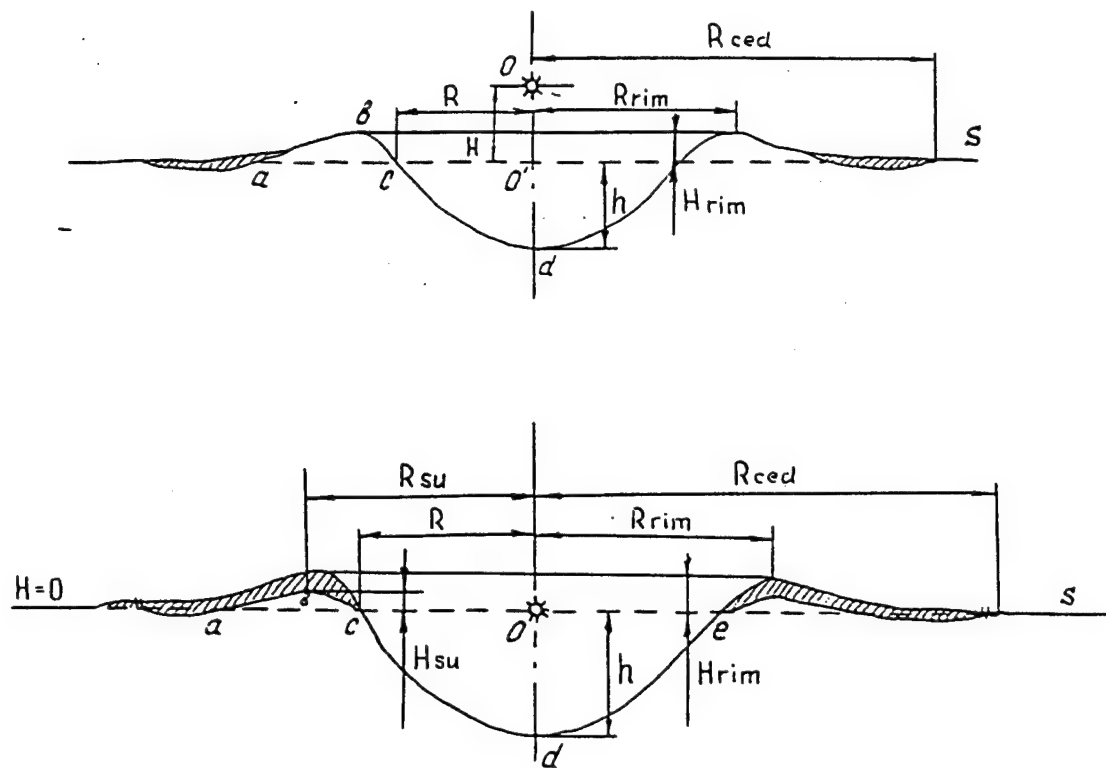


Fig. 2.1. Typical surface burst crater.

- R - crater radius at the pre-event surface;
- h - crater depth below at the pre-event surface;
- R_{rim} - rim crest crater radius;
- H_{rim} - average rim crest height;
- R_{ced} - continuous ejecta deposit outer radius;
- R_{su} - radius of a maximum structural uplift;
- H_{su} - height of the structural uplift.

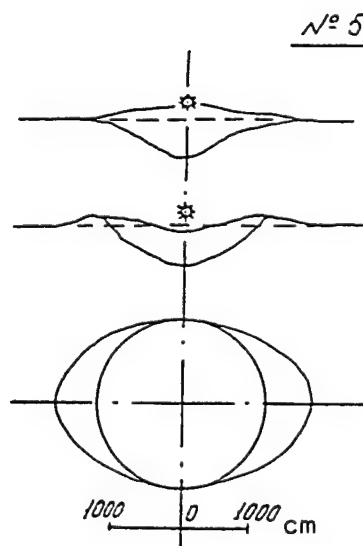
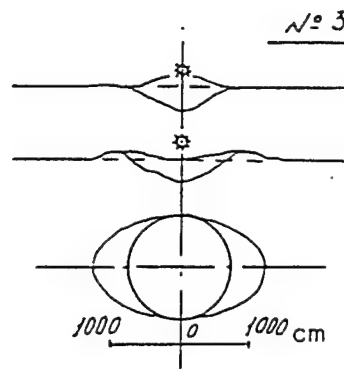
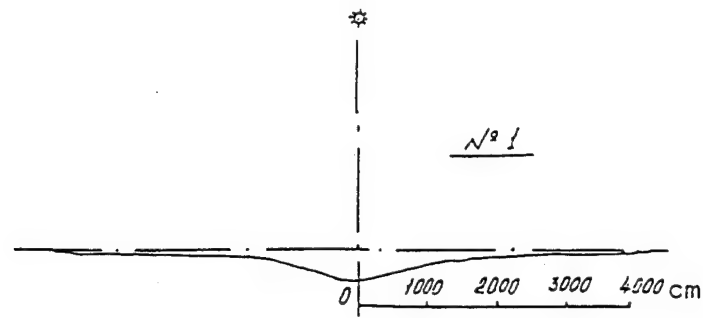


Fig. 2.2. Profiles of craters along different azimuths for events ## 1, 3, 5.

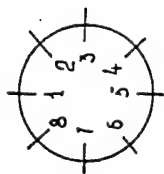
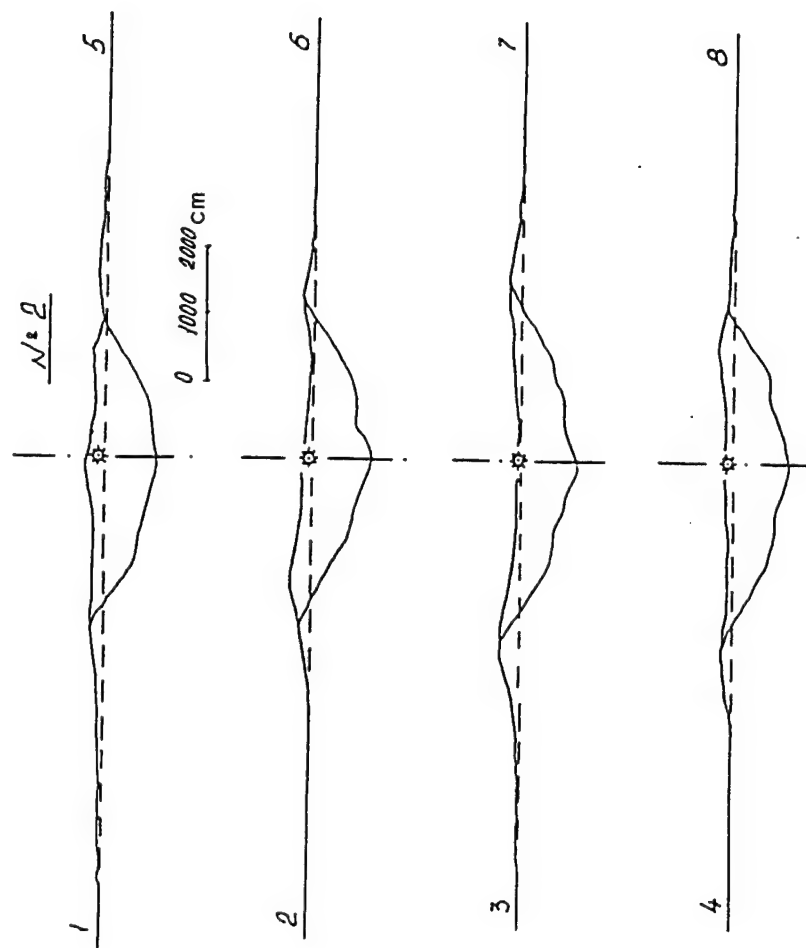


Fig. 2.3. Profiles of crater along different azimuths for event # 2.

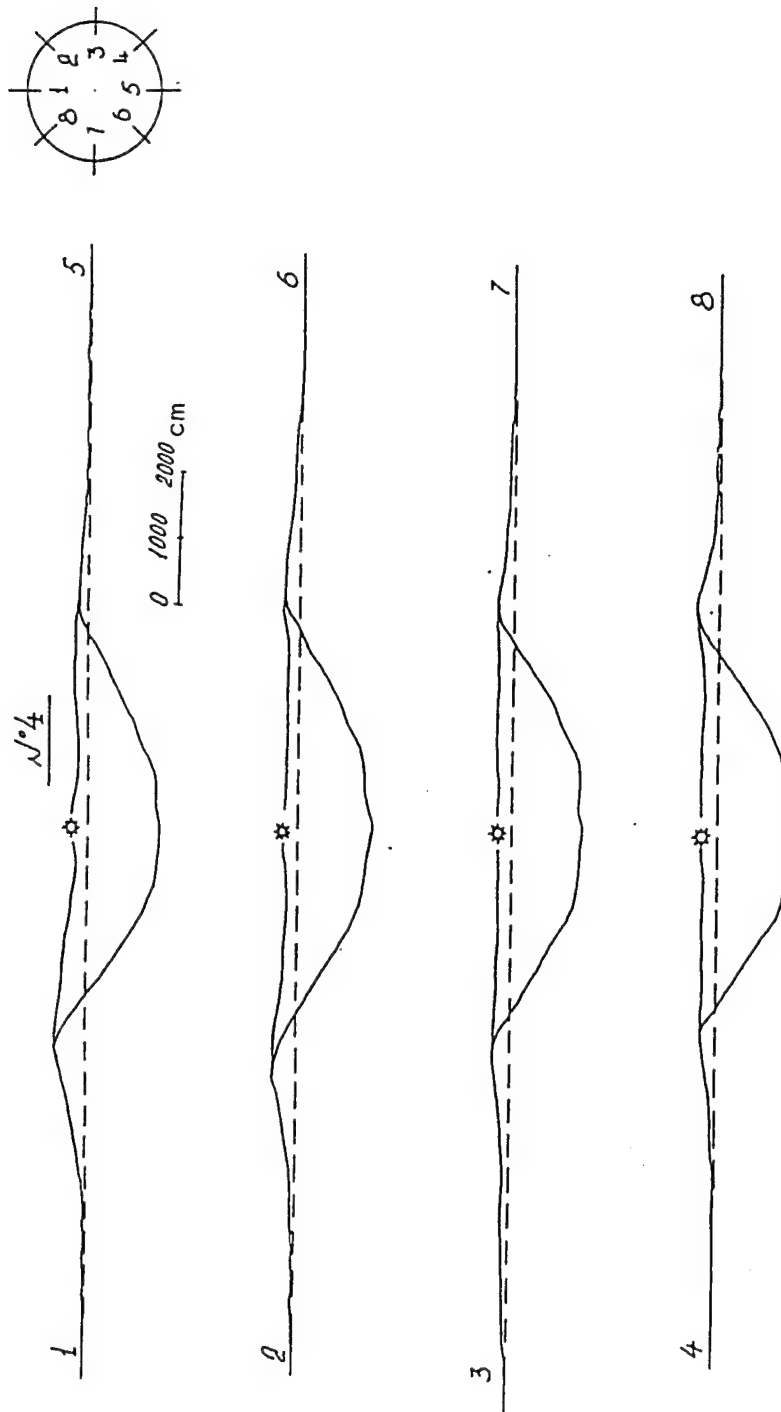


Fig. 2.4. Profiles of crater along different azimuths for event # 4.

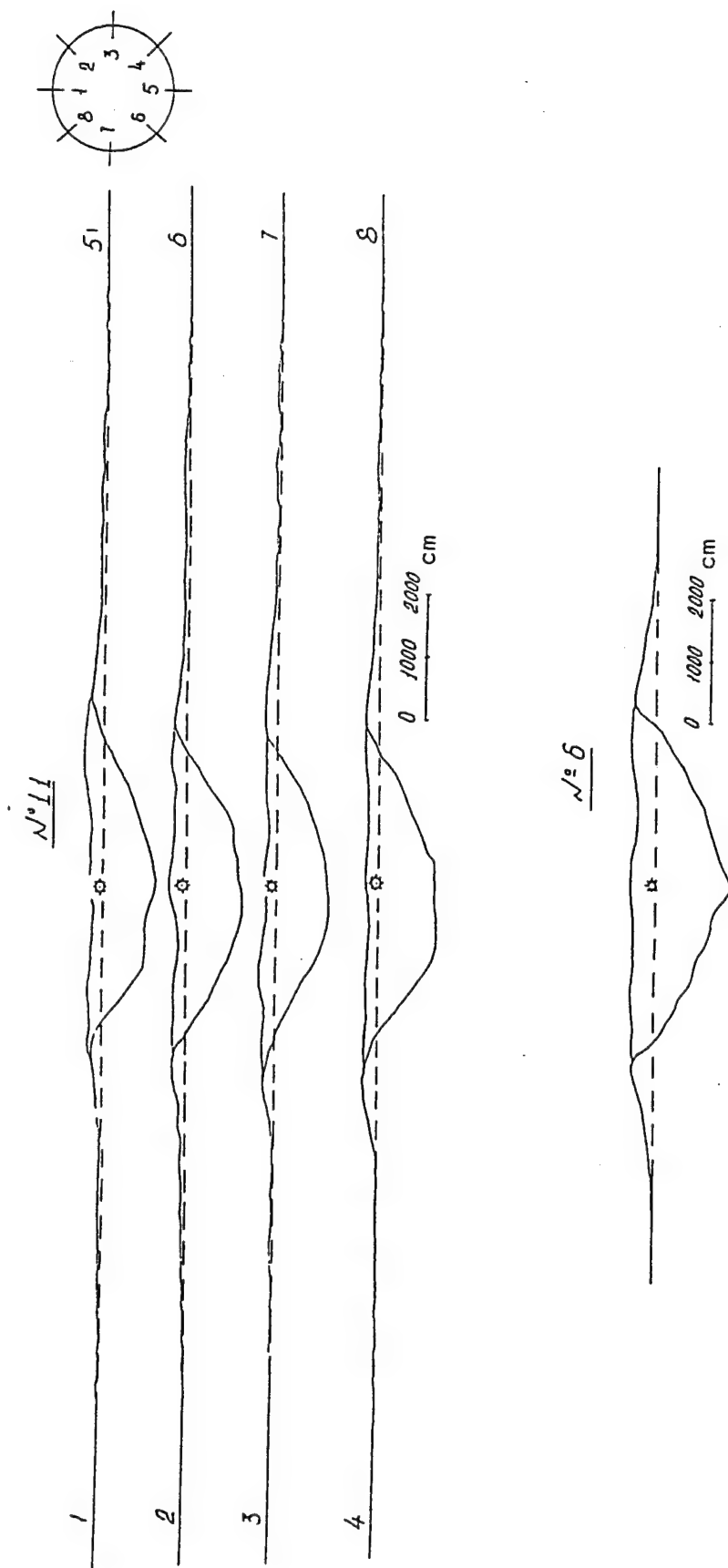


Fig. 2.5. Profiles of craters along different azimuths for events #6, 11.

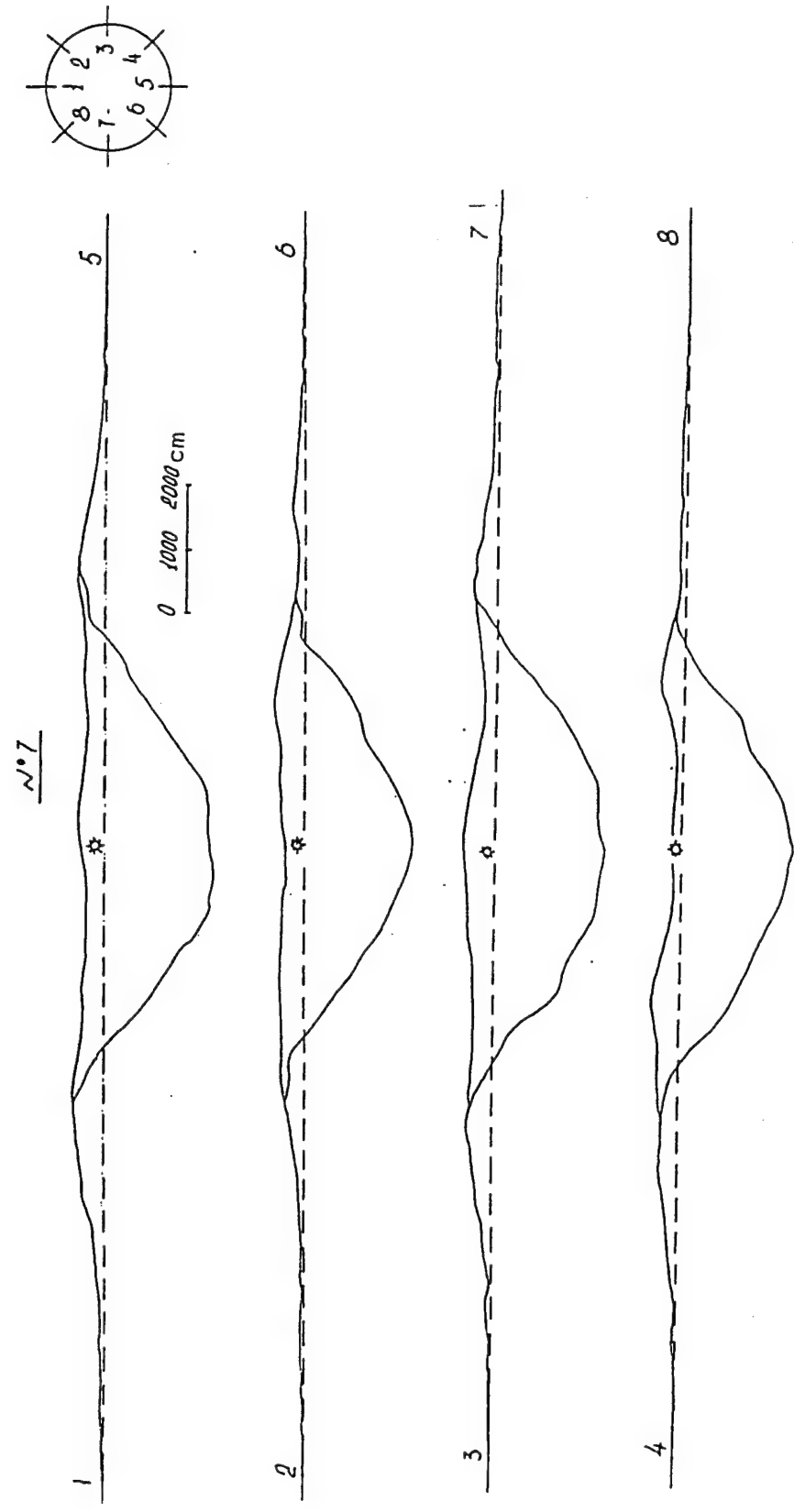


Fig. 2.6. Profiles of crater along different azimuths for event # 7

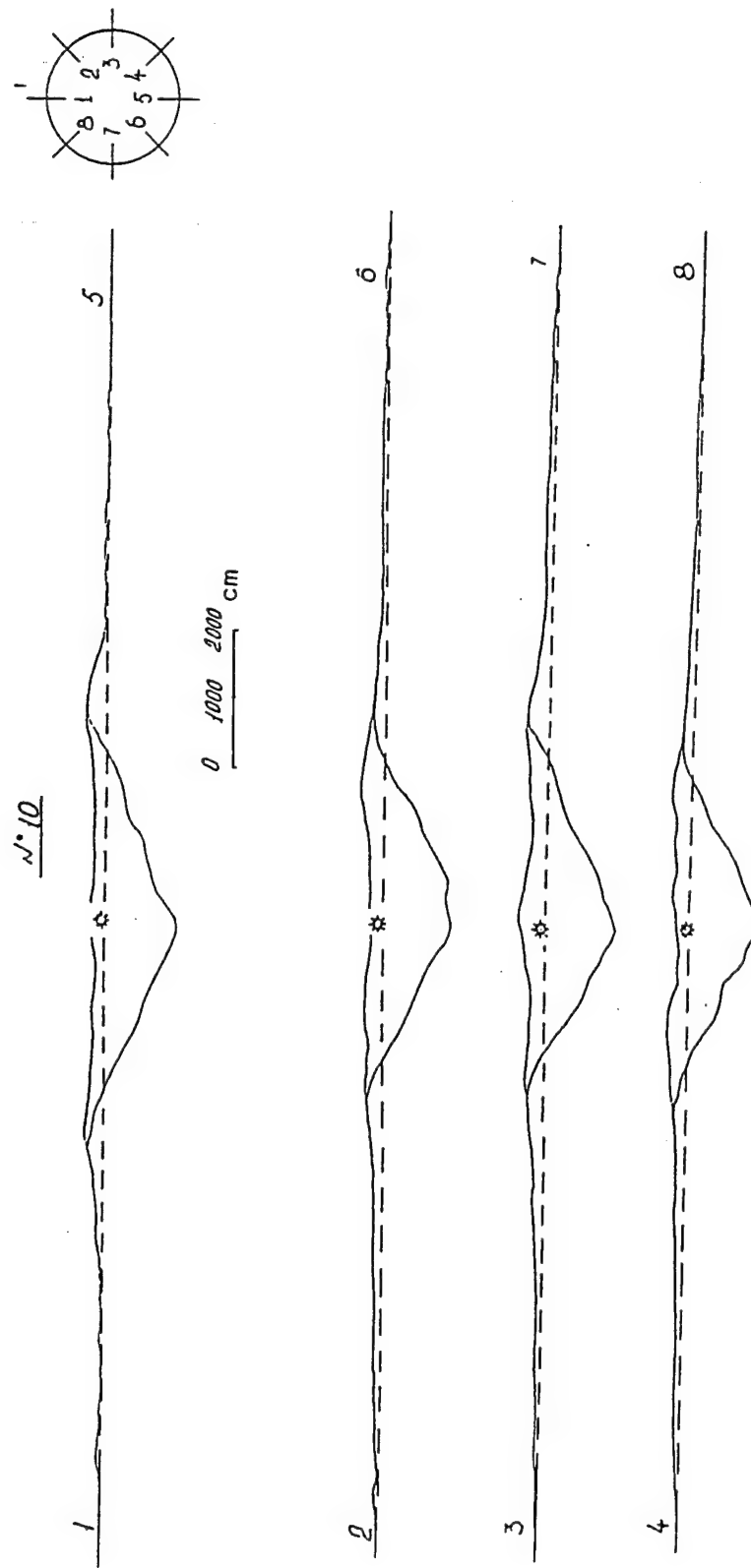


Fig. 2.7. Profiles of crater along different azimuths for event # 10.

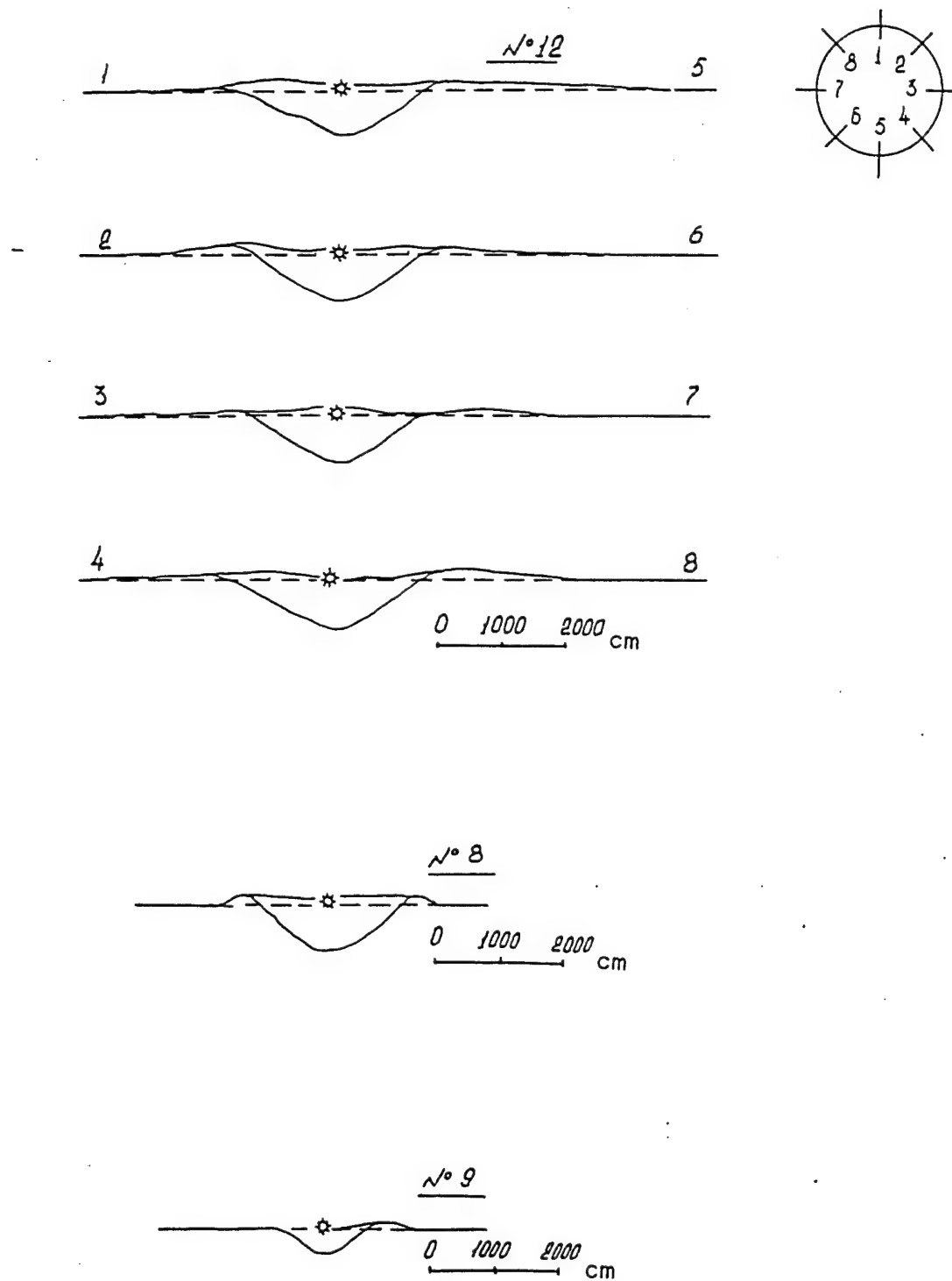


Fig. 2.8. Profiles of craters along different azimuths for events ## 8, 9, 12.

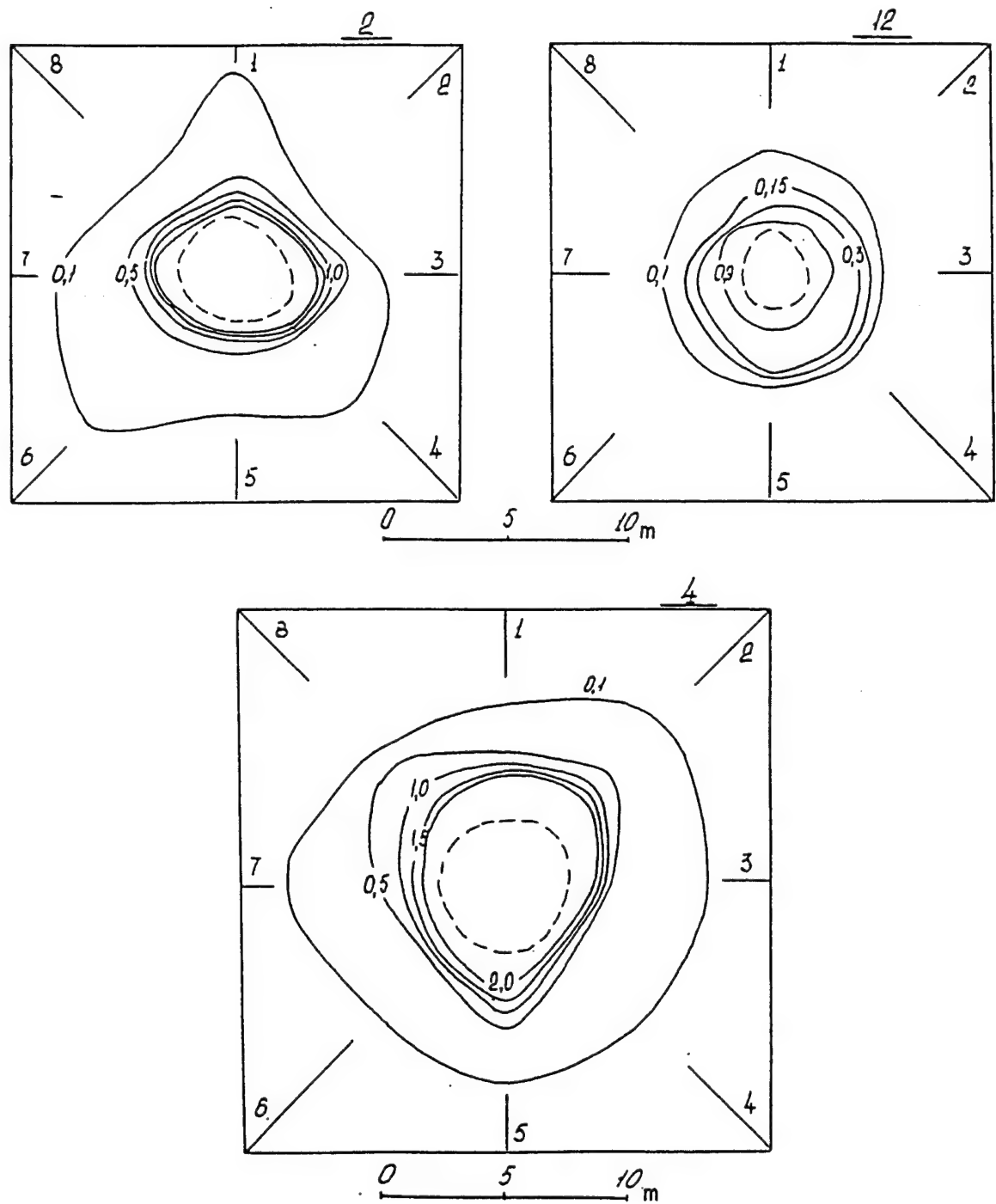


Fig. 2.9. Isolines of ejecta thickness for surface burst events # 2, 4, 12. Dashed lines - crater contour at the pre-event ground level.

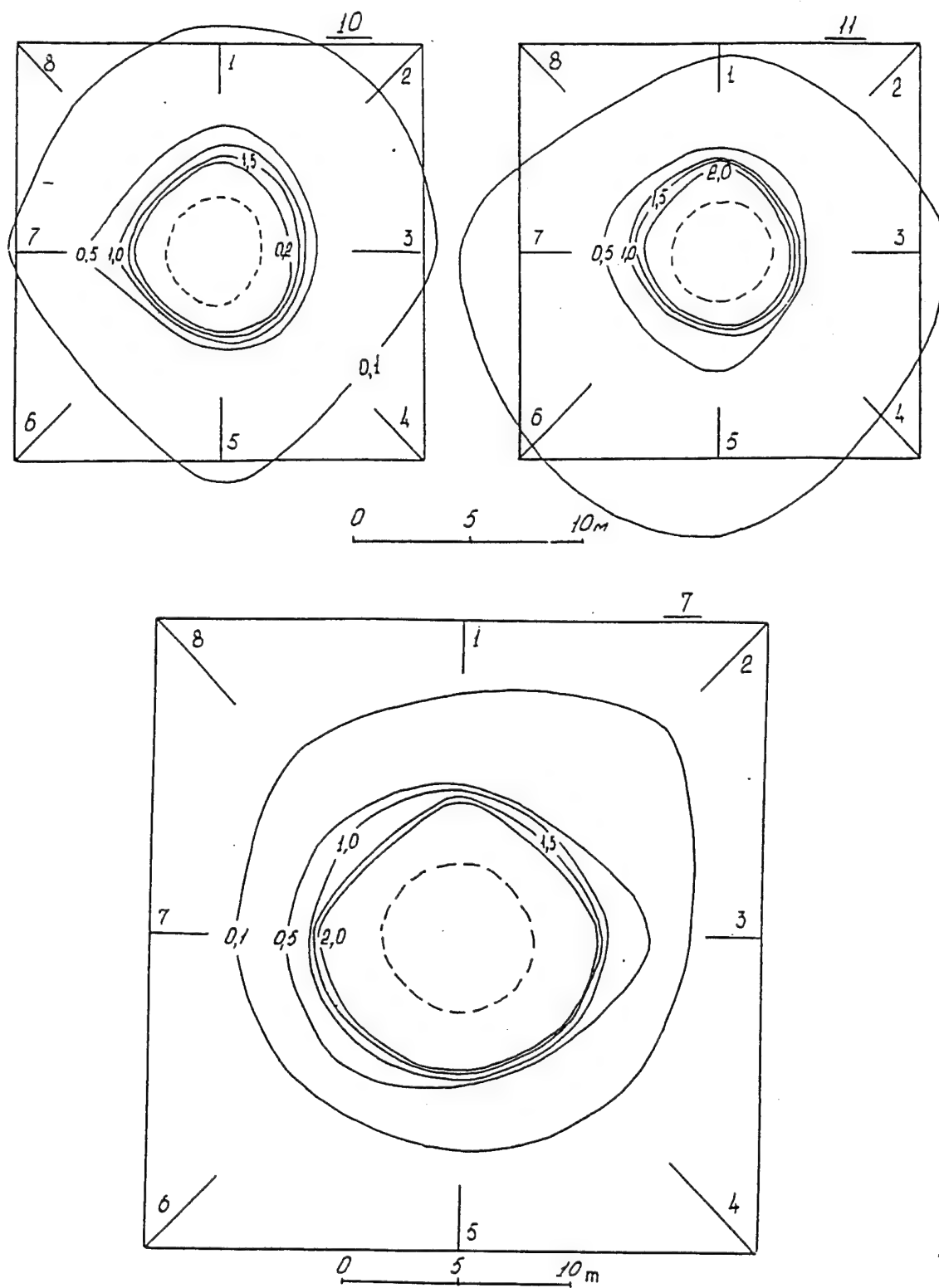


Fig. 2.10. Isolines of ejecta thickness for surface burst events # 7, 10, 11. Dashed lines - crater contour at the pre-event ground level.

3. Excavation explosions of HE charges

In 1957 an extensive series of explosion experiments was conducted at the USSR. The purpose of experiments was to study scale effects for increased depths of burst. These experiments (especially the explosion of 1000 ton HE charge) for the first time clearly demonstrated the gravity effect at crater size.

The program of experiments consisted of two sequences: (1) explosions of charges with mass 10, 80 and 1000 kg in loess-like loam, and (2) explosions of charges with mass 100 kg, 1, 10, and 1000 ton in clay. Explosions of 100 kg charges used to compare excavation efficiency in two different media.

Crater and ejecta deposits zone were measured by topographic survey. Measured data used to built the crater and ejecta zone map and two cross-sections along perpendicular directions. The later used to calculate crater volumes.

Movie cameras with a constant frame speed registered an explosion dome uplift. The velocity of the uplift was measured also by contact gages installed at different heights above the initial ground surface. When the uplifting ground surface touched a gage, it generated an electrical signal, recorded by oscilloscopes.

Table 3.1 and 3.3 summarize main parameters of excavated craters: Table 3.1 contains data for explosions in loess-like loam, Table 3.2 shows data for explosions in clay. Fig. 3.1-3.6 displays crater profiles.

Loess-like loam has follows mechanical properties:

density	1800 to 1900 kg m ⁻³
porosity	40 to 50 %
moisture content	10 to 30 %

Clays properties are:

density	1800 to 2200 kg m ⁻³
porosity	5 to 10 %
moisture content	25 %

Soil density increased with depth. At the same time near to surface soil density was sometime less than listed above: surface layers of loess had density of 1600 kg m⁻³.

Experimental study allowed to separate schematically the excavation process into 3 stages.

The first stage endures from the moment of detonation to the moment when a compressive wave reaches the free ground surface. The ground motion here is exactly the same as for totally contained explosion. The free surface does not influence the motion. The time duration of the symmetrical motion is relatively short, but this stage is very important for consequent effects. For example, experiments show that explosions with the characteristic ratio $n < 3$ the explosion cavity has enough time to grow up to the size close to camouflet cavity. This fact demonstrates that at excavation explosions a large part of energy is spent to plastic deformations and consequent heating of the target material.

At the second stage energy of detonation products is used mostly to accelerate the ground in the direction to the free surface. The free surface distorted previously central-symmetrical velocity field and maximum uplift velocity may be essentially larger than the particle velocity at the compression wave front. As the result, the specific dome of uplifted ground is formed. Thickness of the dome shell is small and continues to decrease as the dome uplifts. Later the dome disrupts into a swarm of flying fragments. At the end of the second stage the energy of detonation products is totally consumed.

Third stage is the inertial flight and deposition of fragments in the gravity field.

The 1957 experiments created the foundation to construct the above mentioned scenario of crater excavation explosions.

Table 3.1. Explosions in loess-like loam

#	Charge mass, ton	DOB, m	Crater dimensions			n
			Radius, m	Depth, m	Volume, m	
1	0.01	0.6	1.5	0.9	a)	2.5
2	0.01	0.65	1.7	0.95	a)	2.65
3	0.01	0.95	1.75	0.8	a)	1.84
4	0.01	1.0	1.75	0.8	a)	1.75
5	0.01	1.2	1.8	0.75	a)	1.5
6	0.01	1.55	1.8	0.7	a)	?
7	0.08	2.0	3.25	1.8	27	1.62
8	0.08	2.5	3.85	1.9	36	1.54
9	0.08	2.75	3.7	1.7	32	1.35
10	0.08	3.4	3.75	0.5	17	1.1
11	1.0	4.0	8.0	3.4	385	2.0
12	1.0	5.0	7.0	2.85	225	1.4
13	1.0	6.0	8.4	3.95	425	1.4
14	1.0	7.0	8.5	3.1	315	1.2

a) Volume is negligible

Table 3.2. Explosions in clay

#	Charge mass, ton	DOB, m	Crater dimensions			n
			Radius, m	Depth, m	Volume, m	
15	0.12	1.95	3.5	1.9	26	1.79
16	0.115	2.65	4.8	2.75	66	1.81
17	0.12	3.1	4.5	2.0	48	1.45
18	0.105	3.4	3.6	1.7	26	1.06
19	0.09	3.35	3.0	1.0	14	0.9
20	1.0	4.4	8.4	3.9	320	1.91
21	1.0	4.4	9.2	4.5	530	2.1
22	1.0	5.0	8.8	4.85	500	1.76
23	1.0	5.4	8.6	4.8	420	1.59
24	1.0	5.9	8.3	2.95	300	1.4
25	1.0	7.0	10.0	0	0	1.43
26	10.0	9.25	18.5	7.5	3760	2.0
27	10.0	11.0	19.0	9.7	4210	1.73
28	10.0	13.0	17.5	9.0	3800	1.34
29	981.0	40.0	75.0	32.0	238000	1.87

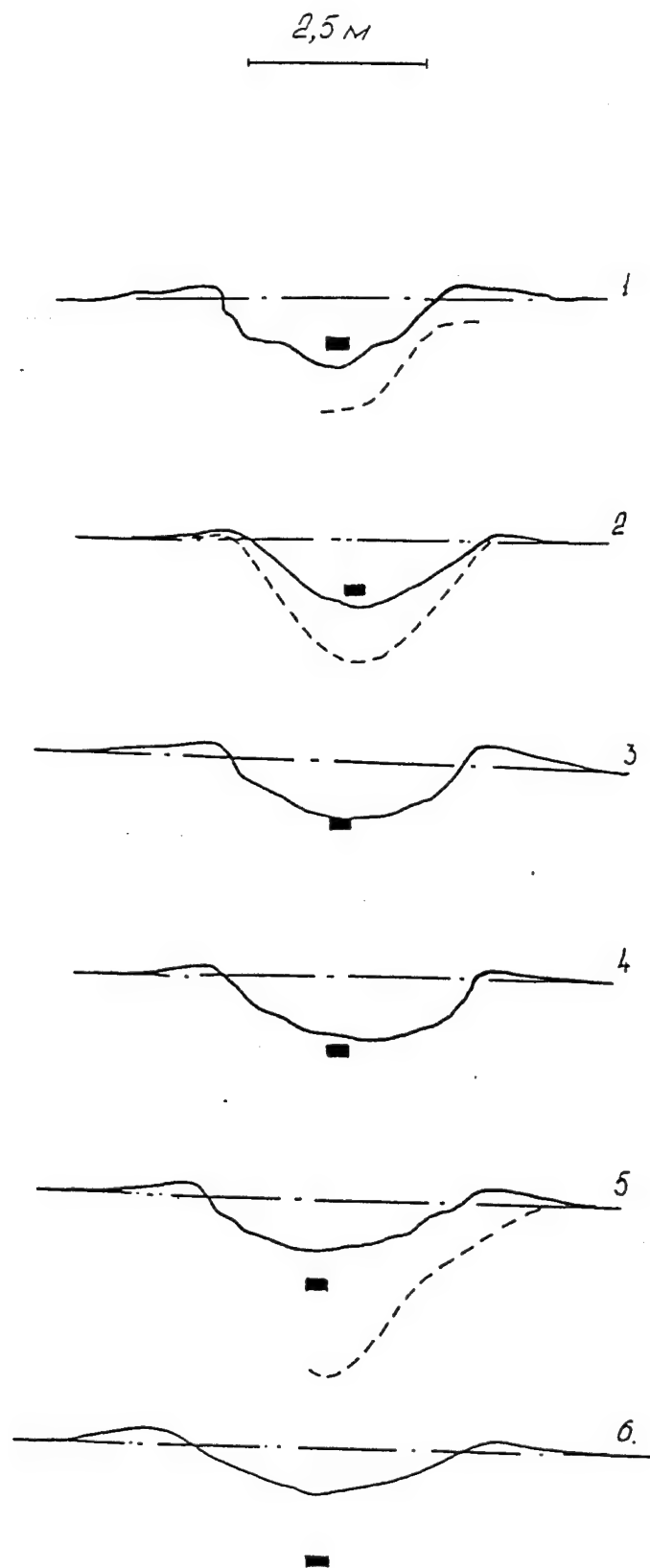


Fig. 3.1. Profiles of craters for bursts ## 1 - 6.

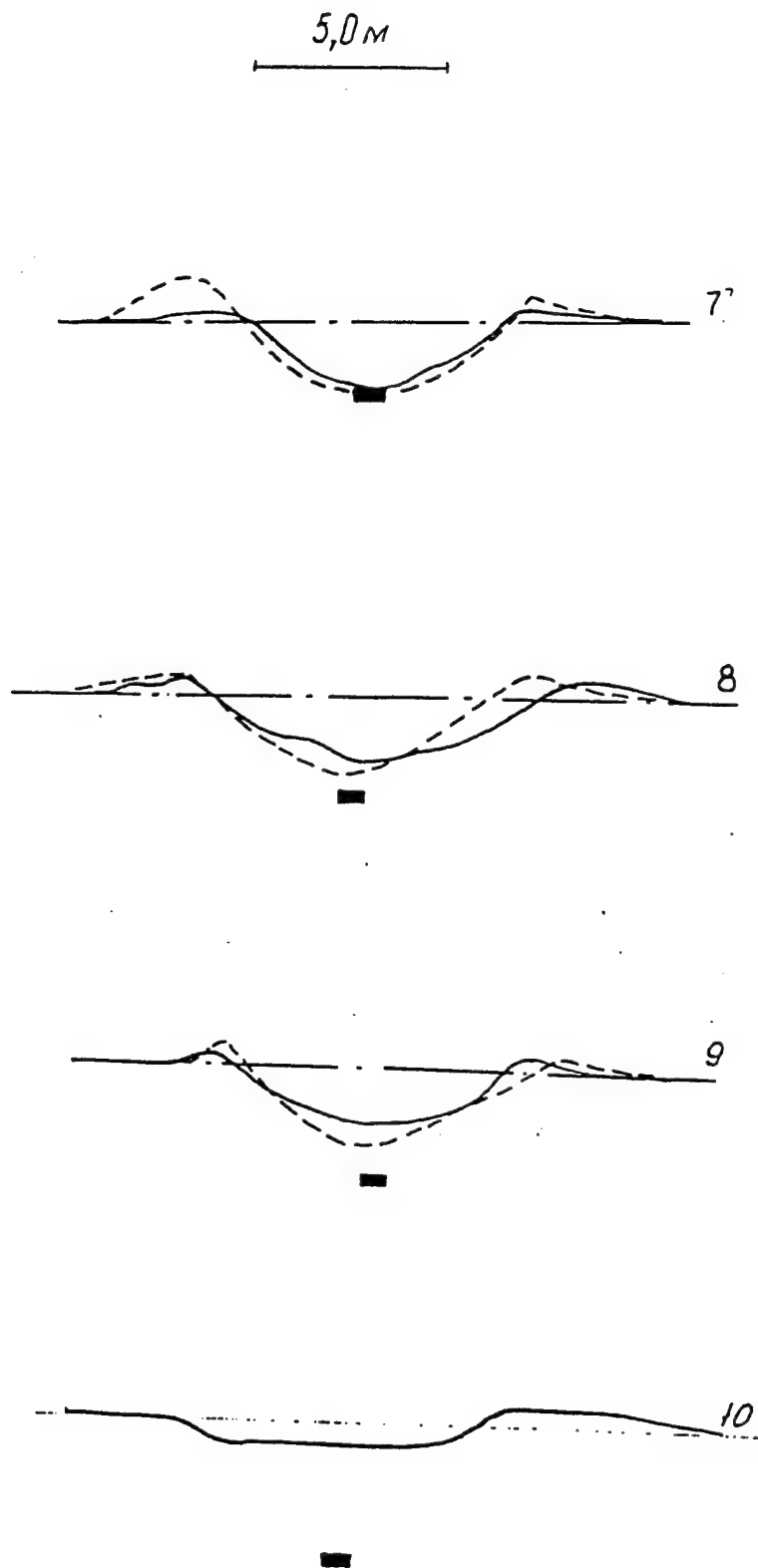


Fig. 3.2. Profiles of craters for bursts ## 7 - 10.

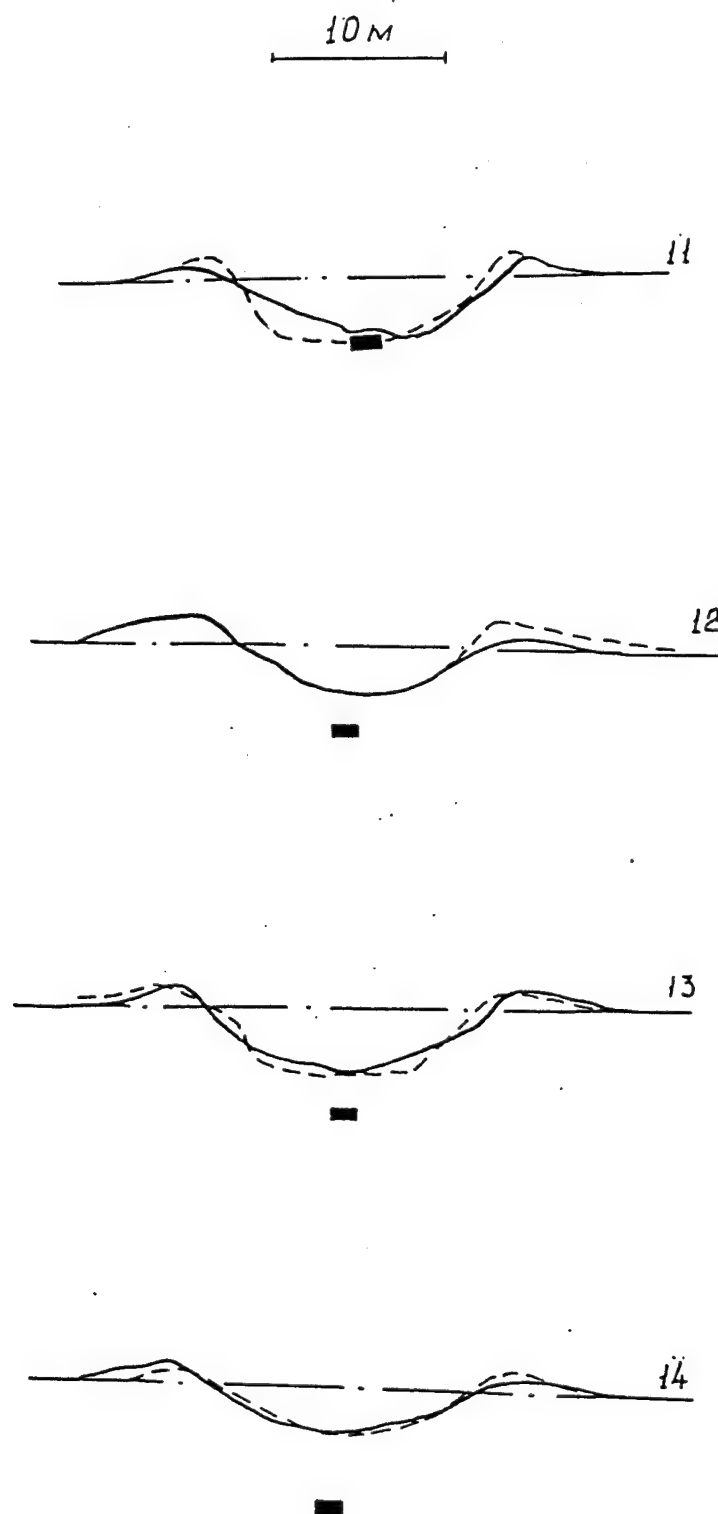


Fig. 3.3. Profiles of craters for bursts ## 11 - 14.

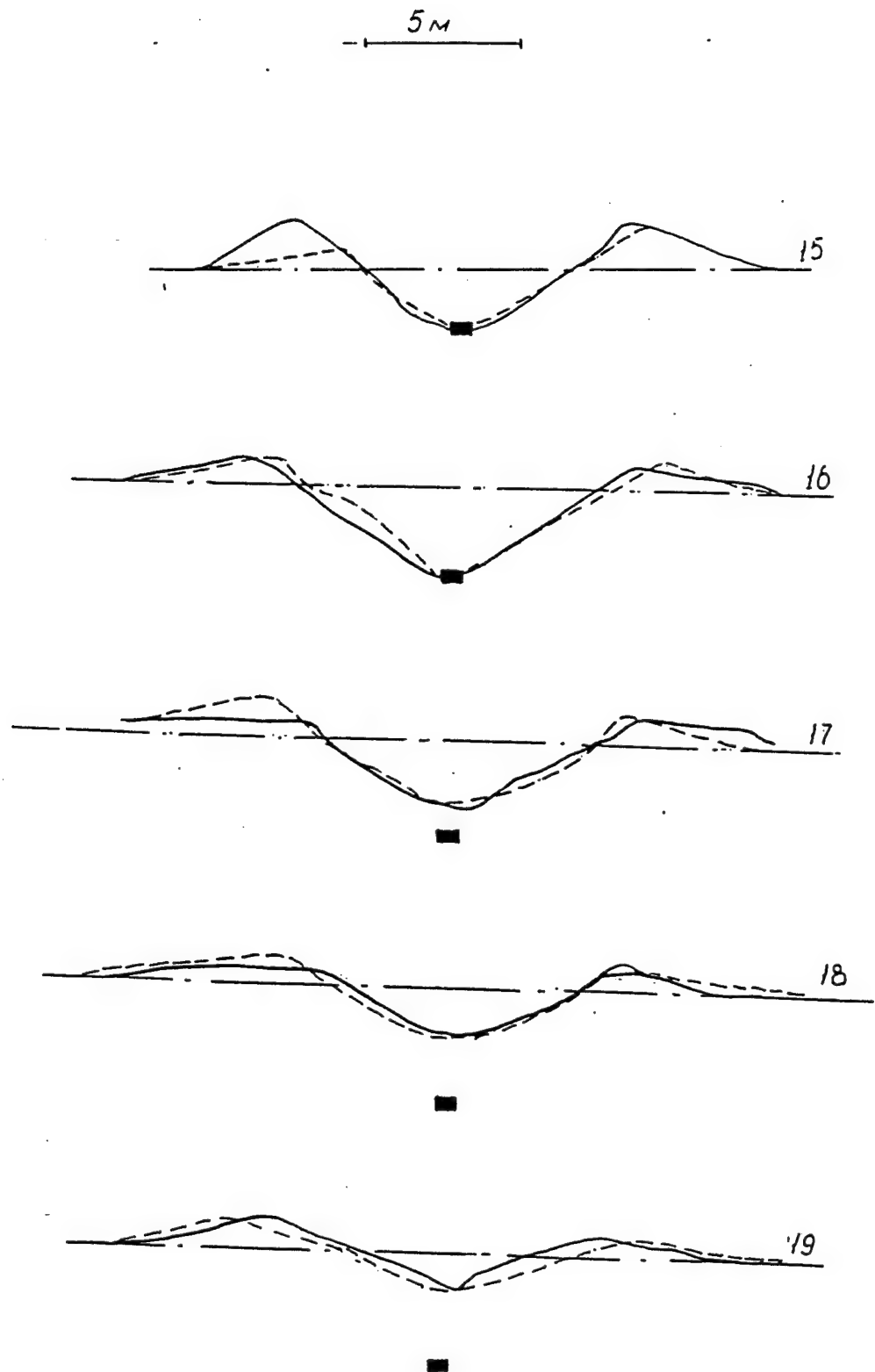


Fig. 3.4. Profiles of craters for bursts ## 15 - 19.

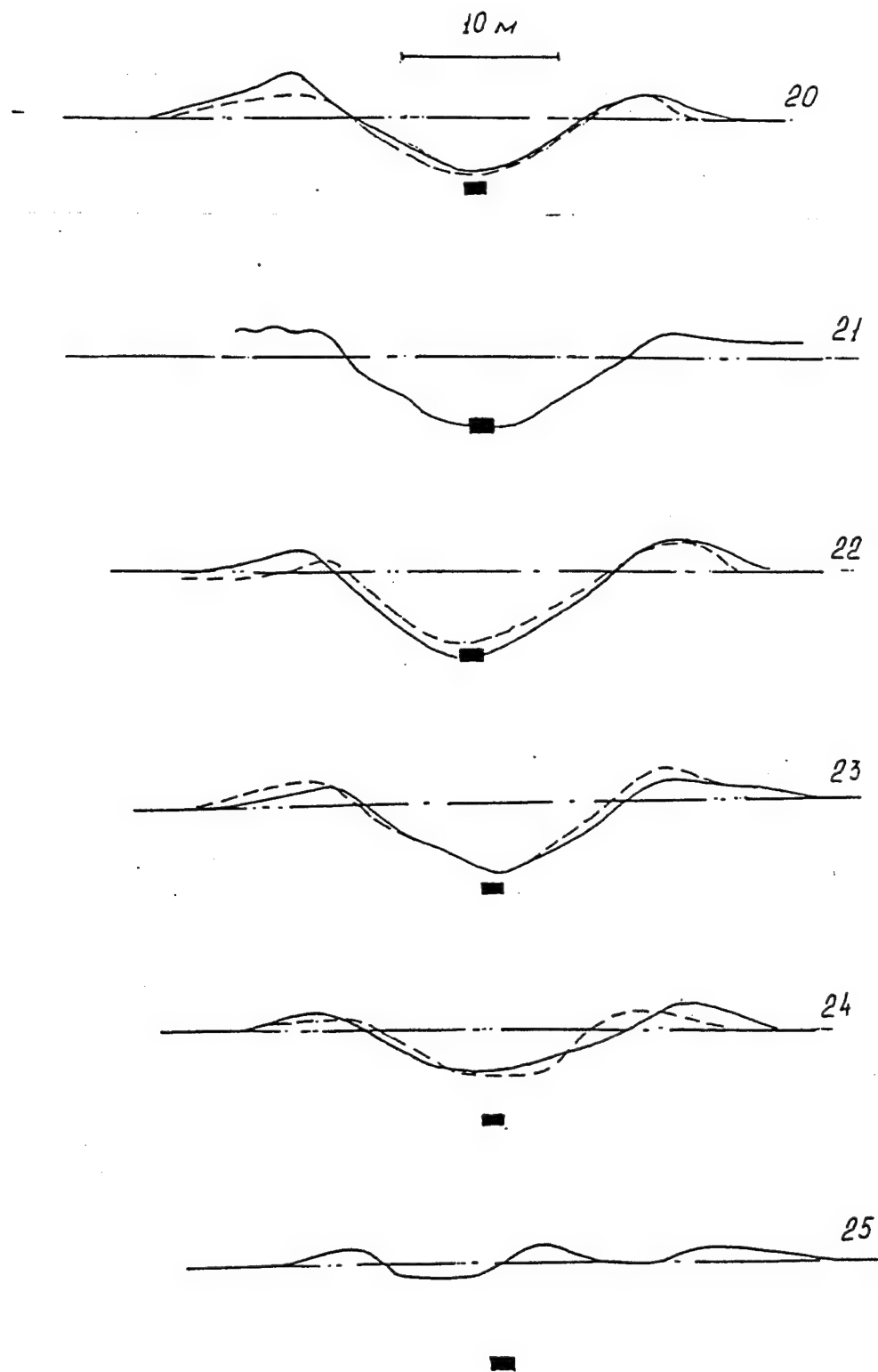


Fig. 3.5. Profiles of craters for bursts ## 20 - 25.

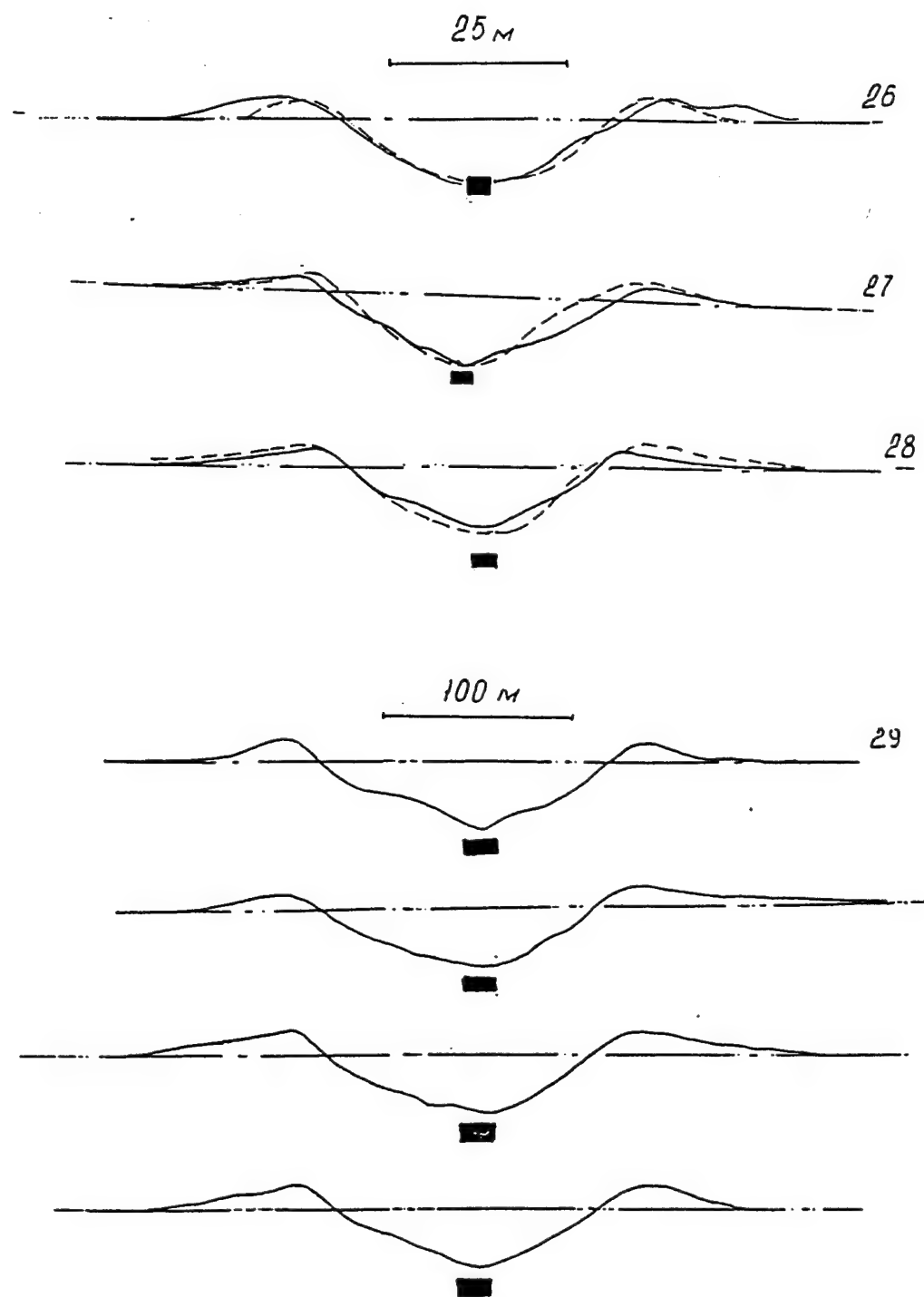


Fig. 3.6. Profiles of craters for bursts ## 26 - 29.

4. Physical Modeling of Excavating Explosions

The thorough study of cratering explosions, presented above, namely the scheme of consequent stages of energy transfer into excavated rocks, resulted in the special technique of large scale excavation explosion modeling.

Suppose that the first, shock-wave stage of explosion has been terminated. The dimensions of shot cavity are thus known. The rock around the shot cavity has suffered disintegration free-surfacewards. The breakdown zone radius is also known; as a rule, it is 2-3 times the charge burial depth. For this reason, the original strength properties of the rock are of minor importance. The shattered rock is visualized as a medium composed of grained particles. The cohesion between separate fragments of this medium is not great, and the medium offers resistance to shear stress in accordance with the law of dry friction. No kinetic energy imparted to the rock at the shock-wave stage is taken into account. Determinative of the process is motion of broken material in the gravitational field by the action of gas acceleration. The work done by gaseous explosion products is dependent on thermodynamic parameters and burial depth of explosion.

As we discuss above, the excavation process may be described as ejection of crushed rock by the gaseous explosion products. The initial explosion stage within which the shot cavity is formed and the rock undergoes destruction is ignored, and its involvement is reflected only in the choice of appropriate parameters of the initial model state. The zero-of-time for the initial model state is taken the time of termination of the first stage. Therefore the shot cavity radius r , the cavity gas energy E (or pressure P), and the explosion depth W are taken as the initial model parameters. Since the rock ejection process is a slow one, the medium compressibility may be ignored. To characterize the broken rock, we make use of the density ρ , the internal friction coefficient K , and the cohesion C (to account for the cohesion of ejected rock with surrounding massif). Naturally, the gravitational acceleration g and the atmospheric pressure P_0 over the free surface are to be included among the determining parameters. The dependence of the major crater dimensions (for example, radius R) on the initial conditions and the properties of ejected rock reads:

$$R/W = F(E/\rho g W^4; E/P_0 W^3; E/c W^3; W/r; k) \quad (4.1)$$

Two limited cases are distinguished in relationship (4.1). First, when parameter $E/\rho g W^4$ may be left out of consideration, a geometrical similarity takes place, and the cavity gas energy is $E \sim W^3$.

Apparently, a necessary and sufficient condition of this is the smallness of quantity $\rho g W$ when contrasted P_0 and C . This condition defines small-scaled explosions. In the other limiting case, when the scale of an explosion is large, the only parametric term incorporating energy is $E/\rho g W^4$. This signifies that similar craters with $R/W = \text{const}$ are generated at $E/\rho g W^4 = \text{const}$, that is, the cavity gas energy must be proportional to W^4 , rather than to W^3 , as one should expect on the geometrical scaling basis. If the medium characteristics remain invariant, the role of parameter $E/\rho g W^4$ becomes increasingly more decisive with higher scaling of the event.

As suggested by relationship (4.1), it will suffice, to comply with the modeling scaling conditions, to diminish the dimensional parameters P_0 , c , E , W , r such that the dimensionless combinations in the modeling experiment were the same in value as their real-life counterparts. To this effect with a view to reduce the value of P_0 , an evacuation

technique has been applied to the atmosphere over the free surface. In order to reduce the value of c , granular and unconsolidated material have been used in modeling, with insignificant cohesion and grains much smaller in size than the explosion depth W . This choice of the model material was in conformity with the schematization conditions which require the ejected rock be unconsolidated. The model cavity gas energy E was brought in correspondence with the explosion depth W to obey the scaling conditions. The model cavity radius r was chosen subject to the condition of maintaining constant W/r ratio. Thus, the underlying idea of the adopted modeling method is transformation of force fields aimed at maintaining the same proportion of forces operative both in model and in real life. A controlled variation of the free surface pressure and of the material cohesiveness will allow to reach the needed relation of determining parameters subject to scaling conditional in conduction a properly scale explosion.

In particular, in modeling large-scaled excavating explosions - a major pursuit of our endeavors - the effect of parameters $E/P_0 W^3$ and $E/c W^3$ was reduced to a linear case owing to the use of high vacuum and dry quartz sand. Under such conditions, the dimensionless parameter $E/\rho g W^4$ becomes a determining one. To meet these conditions, a massif of dry sand was loaded in a vacuum chamber. Within the sand massif, a volume of compressed air encased in a spherical elastic envelope was emplaced at a definite depth. The sudden expansion of gas from ruptured envelope produced an excavatory action on the overlying layer of sand to form a crater. In this experiment, the dimensionless combinations of determining parameters were in correspondence with the conditions for conducting a large-scaled explosion.

MODELING FACILITIES. In designing our physical model, a number of versions have been tried. Schematically, a diagram of one of this installation is shown in Fig. 4.1. The vacuum chamber, shaped as a 80*80*100 cm rectangular parallelepiped with stiffening ribs, was made from sheet steel 8 mm thick. The front side of the chamber was made from a transparent Plexiglas plate 5 cm thick to allow visual inspection. The upper part of the back side could be hinged out to admit access for the preparation of an experiment and for making post-shot measurements of the crater formed. Model material was loaded in the chamber to fill up about a half of the available volume. The pressure inside the chamber could be set at any level from the atmospheric down to 10^{-5} - 10^{-6} kg/cm². A standard vacuum gauge was used to measure the subatmospheric pressure. The "explosive charge" was a thin rubber envelope of spherical shape containing a working volume of air; the envelope was enclosed within a wire mesh framework which thus specified the cavity volume. The clear area of the wire mesh framework surface was 80-90% and practically did not affect the accuracy of experimental measurements. During the chamber evacuation, the excessive pressure in the working volume was controlled at a given level with the aid of a differential manometer. The differential manometer was an air-tight cylinder 5 cm in diameter and 60 cm in height, filled in part with mercury. A tube with an open end 8 mm in diameter ran down the mercury column nearly touching the cylinder bottom. The upper end of the tube was connected to the working volume, the space over the mercury surface communicated with the vacuum chamber. Making the mercury level vary, one can control a specified excessive pressure inside the working volume. In the course of evacuation, the excess air from the working volume passes through the mercury to maintain an excessive pressure in the working volume. The working volume pressure with respect to the pressure over the material surface is controlled by the mercury manometer and at need, with the differential manometer shut off the system, can be raised to the atmospheric. The needed vacuum having been reached, the envelope is

ruptured through its contact with a Ni-Cr alloy filament heated with electric current. The gas volume, suddenly released, ejected the model material to form a crater. The time of envelope rupture was automatically synchronized to the start-up of a high-speed instrumentation camera which recorded the throwout process.

This installation has been used to model nuclear cratering explosions and certain familiar large-scaled chemical explosions under the conditions of a simple free-surface topography. The experimental model results compared with the results of field test explosions in both the crater dimensions and kinetic parameters.

Table 4.1 summarize values of crater radius-to-DOB ratios for several large scale explosions and their model analogs.

Table 4.1

#	Explosion event	Real value of R/W	Model value of R/W
1	BHL 1004	1.18	1.2
2	BHL 1003	1.7	1.12
3	T-1	1.19	1.15
4	Sedan	0.95	0.9
5	Schooner	1.2	1.27
6	Cabriolet	1.06	1.03

The further elaboration of the modeling technique allowed to simulate large-scale explosions with complex mountain environments. Beginning 1972 all projects of hydropower construction using HE explosions were pre-tested by the model technique, described above. 3D models of real explosion sites were created in the vacuum chamber using sand mixture with up to 1% of glycerol. The power source for the explosion simulation was a pressurized rubber bag. The modeling allowed to estimate the optimum consequence of charges position, energy, and detonation sequence to create the project dam profile.

The typical example is the explosion construction of the dam at the river Uch-Terek. The explosion site was situated at the narrow valley with slope angle up to 50 degrees and depth up to 200 m. Explosion charges were buried under the right slope at two levels. The low level charge of 544 ton had a length of 145 m and DOB (normally to the free surface) 50 to 65 m. The upper charge of 620 ton had the length of 92 m and DOB of 82 to 94 m. Charge masses are cited in equivalent tons of TNT as the lower charge was constructed of ANFO (5.5% of fuel oil). The upper charge was designed for rock fragmentation at the upper part of the valley slope. The lower charge detonated 5 seconds later than the upper charge. It was designed to push out rocks, sliding down after the first charge detonated.

Fig. 4.2 shows profiles of the constructed dam across and along the valley. The dashed line corresponds to the model predictions. One can see the reasonably good fit of the model and the real dam profiles.

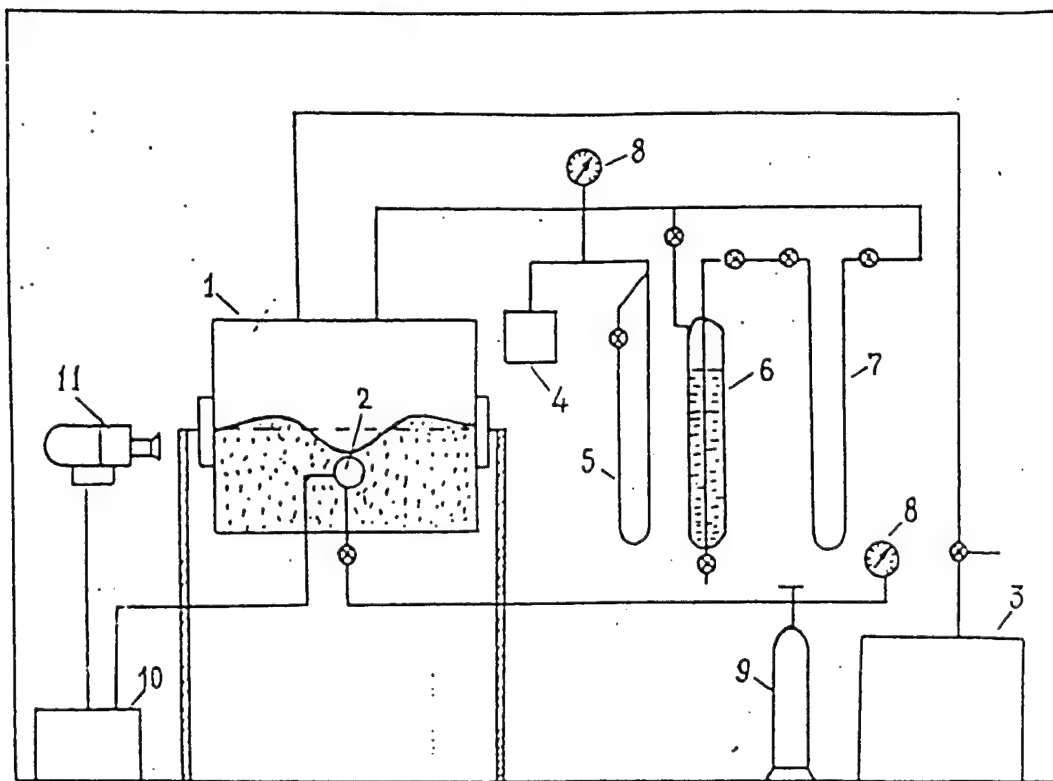


Fig. 4.1. The modelling installation diagram: 1 - vacuum chamber; 2 - working volume; 3 - vacuum pump; 4 - vacuum gauge; 5 - oil pressure gauge; 6 - differential manometer; 7 - mercury manometer; 8 - compound pressure and vacuum gauge; 9 - compressed air cylinder; 10 - blasting unit; 11 - instrumentation camera.

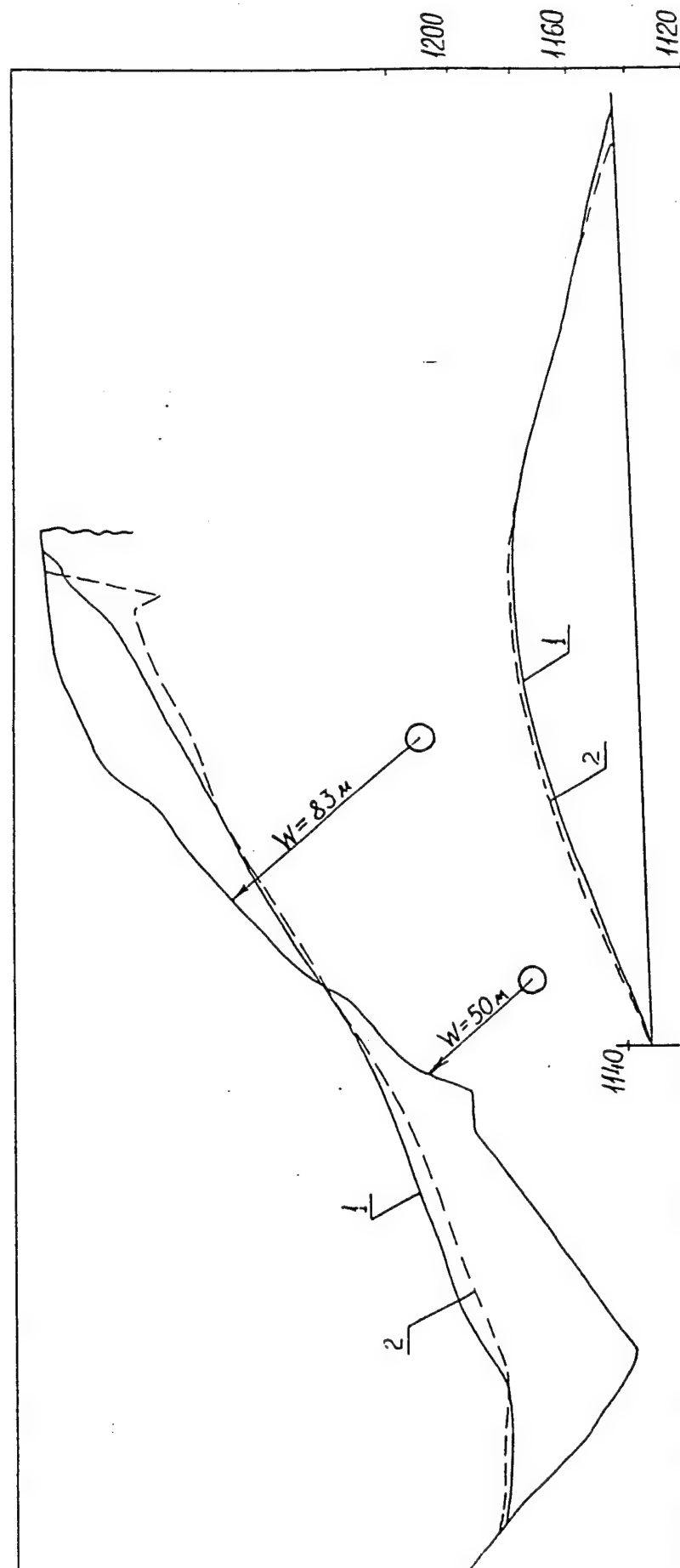


Fig. 4.2. Across- and along-valley crosssections of the dam at the river Uch-Terek
1 - the real explosion dam, 2 - the model simulation

5. Z-model for near surface bursts.

5.1. Historical notes.

In the early 70th the model of the excavation ground was created, named by US researchers as Z-model. Independently, in 1973-75 the similar model was elaborated in Russia. First unclassified publications seems to appear simultaneously in 1976 in Abstracts for the Symposium on Planetary Cratering Mechanics, Flagstaff, Arizona, 13-17 September 1976 and next year [4, 5, 6, 7]. Only in 1994 Russian researches got a possibility to look through the one of basic American reports described Z-model [8]. It become obvious that in 1974 Maxwell and Seifert always done many of applications, which was re-invented in Russia during the late 70th. The first unclassified detailed description for the Russian version of Z-model was published only in 1979 [9]. So no questions about priority arise. Nevertheless it seems to be instructive to describe the Russian approach and philosophy for the Z-model, as well as some ideas which we never met in American unclassified publications.

Initially we named our model as Integrally Balanced Flow (IBF) [6] or Simple Model of Cratering (SMC) [7, 9]. As we mostly used the letter n for the velocity exponent, it might be called "n-model", but here we will name the model with its real name.

5.2. Main ideas.

As we can conclude from [8] the starting point for Maxwell was computer simulations of surface bursts, revealed the specific geometry of the velocity field at late stages of cratering. In Russia the starting point based on experiments with a quarter-space geometry [9, 10].

HE charges of PETN detonated at the surface of wet and dry sand in the box. One wall of the box was a transparent one (plexiglas). The steel plug of 2 cm diameter closed the hole in the plexiglas window to keep the window from damage. Charges detonated at the plug surface. In some of experiments the plug was locked with a narrow vertical steel bar fixed at the outer

71
wall of the test box. In other experiments with a window of 5 cm thickness, the plug was allowed to move out of the hole. In this case, the high-speed movie camera may look at the region just below the charge, which was covered by a lock bar in previously mentioned experiments. To be sure that the plug does not make any damage, a rope kept the plug on a short rotational trajectory to the floor.

Small plastic discs and colored sand were used to mark the subsurface deformation. Plastic discs were used to measure final ejecta velocities, colored sand quadrangles were used to measure trajectories of corner points. Fig. 5.1 illustrates the motion of 4 near-surface plastic markers in a quarter-space experiment.

The first experiments were conducted with a modestly dense wet sand. Experiments shown two stages of the cavity growth: At the first stage the crater grown as a self-similar hemisphere. The apparent center of the hemisphere was at the pre-event surface a little bit above. With this geometry the cavity grown up to the maximum depth. At the second stage, the bottom of the cavity rest at the place, but side parts of the target continued to move, creating so-called "wings" of a crater. The final depth-diameter ratio was close to 0.5 for wet sand. Fig. 5.2 illustrates the observed crater growth.

Trying to describe the motion around the cavity during the first stage, we went to the conclusion that the radial velocity at all cavity surface may be supposed as a constant value decreasing with time.

In parallel to these experiments, we analyzed the flow of water due to surface explosion. At the late stage, when the incompressible model may be used, the cavity shape in water was very close to a hemisphere, what was very instructive being compared with surface bursts in sand targets. We constructed the self-similar potential flow, using the series of harmonic functions, revealed close-to-power law spatial decay of flow velocities.

Combining these two data sets, we got two main supposition for Z-model. If one uses the polar coordinates measuring radial distances from the center and the angle from the down-ward

vertical line, these suppositions may be described as follows: 1. Radial velocity is a power function only of radial distance. 2. Tangential velocity is defined by integral balance equations (for simplest case - the balance of mass).

For target materials of constant density ("incompressible media") it is easy to derive the velocity field from above mentioned conditions.

We use the polar coordinate system R, ϑ, φ . The $\vartheta = 0$ axis presents the downward vertical direction, R is the distance from the coordinate center, φ is an angle at horizontal plains. As we treat axis-symmetrical problems here, all values do not depend on φ . For such a coordinate system depth, z , is expressed as

$$z = R \cos \vartheta$$

and radial distance from the vertical axis, r , is expressed as

$$r = R \sin \vartheta$$

After the explosion deposition of energy at the point $R=0$, shock waves go out from the explosion source. The target material behind the wave front begins to move. When the shock waves go far from the center and decay, the zone of inertial motion is formed at the excavation area. The velocity field in this area may be approximately described as follows.

At any point the velocity vector may be presented as the vector sum of radial, v_R , and tangential, v_ϑ , components. According to Z-model, for near-surface explosions the value of v_R does not depend on the angle ϑ and may be described as a power function of R :

$$v_R \sim R^{-Z} \quad (5.1)$$

The condition of incompressibility in spherical coordinates is written as:

$$\text{div } \vec{v} = \frac{1}{R} \frac{\partial}{\partial R}(R^2 v_R) + \frac{1}{\sin \vartheta} \frac{\partial}{\partial \vartheta}(v_\vartheta \sin \vartheta) = 0 \quad (5.2)$$

Substitution of (5.1) to (5.2) gives the equation for the tangential velocity component, which has a solution:

$$v_\vartheta = (Z-2) v_R (1 - \cos \vartheta) / \sin \vartheta \quad (5.3)$$

So from assumption (5.1) and (5.2) we get the following result: The tangential velocity component, v_ϑ , depends on radial distance in the same way as v_R , and at a given R gradually increases from zero value at the axis of symmetry $\vartheta=0$ to the maximum value at

the free surface $\vartheta=90^\circ$ (if the coordinate center is situated at the free surface).

For the flow field expressed by (5.1) and (5.3) it is easy to get trajectories of particles:

$$R = R_1 [(1 - \cos \vartheta)/(1 - \cos \vartheta_1)]^{1/(Z-2)} \quad (5.4)$$

where R_1 and ϑ_1 are coordinates of a "pin" point - a point which fixes a given trajectory.

The Eq. (5.4) clearly demonstrates the shape of trajectories does not depend on time, so trajectories are stationary streamlines. Note that the motion of particles along these trajectories may be non-stationary one. Rotating of two streamlines around the vertical axis of symmetry gives the so-called *stream tube*, which defines the excavation motion of target material.

For some problems it is suitable to choose as the "pin" point the point of a trajectory and the initial target surface level intersection: $R_1 = r_e$, $\vartheta=90^\circ$.

According to Z-model the motion of material ejected from a crater is described as motion along streamlines, defined with the equation

$$R = r_e (1 - \cos \vartheta)^{1/(Z-2)} \quad (5.5)$$

Here r_e is the radial distance where a streamline crosses the initial target surface level (ITSL), the coefficient Z is in the range from 2.5 to 3 for most cases. A pair of two neighbor streamlines which cross the ITSL at radial distance r_e and $r_e + dr_e$ define a stream tube with volume

$$dV_e = 2 \pi \left[\frac{Z-2}{Z+1} \right] r_e^2 dr_e \quad (5.6)$$

The total ejecta volume from a crater with the radius R_t at the ITSL is

$$V_e = (2/3) \pi \left[\frac{Z-2}{Z+1} \right] R_e^3 \quad (5.7)$$

Eqs. (5.6) and (5.7) are derived for the model with the center ($R=0$, $\vartheta=0$) at the ITSL. The similar equations for model with buried center may be found elsewhere (sf. Croft, 1981).

The ejecta velocity for gravity craters may be estimated from rather simple consideration (Ivanov, 1979). The potential energy of the streamline in the gravity field with the free-fall

acceleration g is

$$dP_e = \rho g dV_e \left[\frac{(Z-2)(Z+1)}{2 Z (Z+2)} \right] r_e \quad (5.8)$$

If one approximate the ejecta initial velocity, v_e , as an exponential function of r_e

$$v_e = v_R (R_t/r_e)^m \quad (5.9)$$

where v_R is the coefficient which may be called as "the ejecta velocity at the crater edge". For the simplest estimation m may be treated as a constant in the range from 2.5 to 3.

The kinetic energy at the moment when all the material ejected along the given stream tube is raised above the ITSL may be estimated as

$$dK = \rho dV_e (v_e^2/2) \quad (5.10)$$

The ejection process is arrested at $r_e = R_t$ where

$$dK = dP \quad (5.11)$$

or

$$\rho dV_e (v_R^2/2) = \rho g dV_e \left[\frac{(Z-2)(Z+1)}{2 Z (Z+2)} \right] R_t \quad (5.12)$$

The value of v_R may be expressed from the Eq. (5.12) as

$$v_R = \sqrt{k g R_t} \quad (5.13)$$

where

$$k = \left[\frac{(Z-2)(Z+1)}{Z (Z+2)} \right] \quad (5.14)$$

Eqs. (5.9, 13, 14) define the ejecta velocity, v_e , as a function of the radial distance, r_e , of the point of ejection through the ITSL. The angle of ejection at the ITSL is depended on Z value as

$$\varphi = \tan^{-1} (Z-2) \quad (5.15)$$

The ejecta motion above the ITSL may be modeled with the well-known equation of a free body flight in the gravity field. The horizontal component of the velocity is constant up to the moment of deposition beyond the crater rim and is equal to

$$v_{eh} = v_e \sin \varphi \quad (5.16)$$

The horizontal velocity of the main mass of ejecta, deposited at the rim may be estimated as $v_R \sin \varphi$. Further from the rim the horizontal velocity gradually increases.

Beyond the crater edge (for $r_e > R_t$) the material in stream tubes does not ejected but displaced into a new position. The part of the material raised above the ITSL constructs the

so-called structural uplift at the base of a crater rim. The real motion in this region is rather complicated, but at the first approximation it may be described in terms of Z-model as follow.

Supposing the constant density of the target material one may derive that

$$R_f = \left(r_e^{Z+1} + a_f^{Z+1} \right)^{1/(Z+1)} \quad (5.17)$$

where r_e is the radial distance to the given streamline at the ITSL, a_f is the final radius of the crater profile point of intersection with the given streamline, R_f is the radial coordinate of top point of the streamline at the uplifted target surface. Lower trajectory at the Fig. 5.3 illustrates the model treatment of under-crater mass motion.

Using the geometric relationship (5.5) one may calculate the cartesian coordinates of the uplifted target surface. At the boundary between ejected and uplifted material ($r_e = a_f = R_t$)

$$R_f = 2^{1/(Z+1)} R_t \quad (5.18)$$

And the Cartesian coordinates of the uplifted rim crest are

$$\left. \begin{aligned} r_{ur} &= R_t \sin \vartheta_{ur} \\ z_{ur} &= R_t \cos \vartheta_{ur} \\ \cos \vartheta_{ur} &= 1 - (R_f/R_t)^{Z-2} \end{aligned} \right\} \quad (5.19)$$

Eqs. (5.19) give the maximum estimate of the uplifted rim height, probably never realized in nature due to complex material flow at the crater rim and immediate subsidence of the rim for complex craters. Nevertheless Eqs. (5.18) and (5.19) allow to make first-order estimates of the uplifted rim profile.

For $Z=3$ one can derive:

$$\left. \begin{aligned} V_e &= (\pi/6) R_t^3; \\ dV_e &= (\pi/2) r_e dr_e; \\ v_R &= \sqrt{(4/15) g R_t}; & R &= 4/15 \\ \varphi &= 45^\circ; \\ v_{Rh} &= \sqrt{(2/15) g R_t} = .365 \sqrt{g R_t} \\ r_{ur} &= 1.168 R_t \\ z_{ur} &= .189 R_t \end{aligned} \right\} \quad (5.20)$$

where V_e is the total ejected volume from the crater of an

apparent radius R_t , dV_e is the volume ejected through the stream tube of dr_e width at the surface, ϕ is the ejection angle, v_R is the characteristic ejection velocity near the gravity crater edge, v_{Rh} is the horizontal component of the ejecta velocity, g is the gravity acceleration, r_{ur} the radius of the structural uplift rim crest, z_{ur} is the amplitude of the structural uplift of the pre-event surface. These values are widely used in various applications.

5.3. Using of the Z-model

During 70th and 80th we used the model to estimate various application of surface burst cratering. As some of results has been published, and the same approaches has been found in the American report [8], here we shortly list several main applications:

1. Cratering in the media with an ideal (von Mises) plasticity was studied with the Z-model in [11]. Analogous study has been found in [8].
2. The Z-model helped us to introduce the separation of gravity and strength regimes of cratering [9, 12, 13]. This approach was independently elaborated by R. Schmidt and K. Holsapple [14, 15].
3. Using Z-model we elaboration a functional form to construct a form of a wide-range scaling law, recently used for planetary applications [16].
4. The mass balance based on Z-model helped us to create the model of the ejecta layer deposition [9]. It become obvious from this study that rim profiles for all gravity craters should to be geometrically similar. The same result was reproduced by Housen e.a. [17].

As these results were published (sometime in a short form), it seems practical to skip them here. We can return to these questions if anybody will be interested to discuss them. In this report we concentrate at the problem of Z-model with dilatancy, which analog we never saw at the literature. The short description of the model was published in [18].

5.4. Z-model with shear bulking.

More than 100 years ago Reynolds noted that shear deformation of grain media is accompanied with the increase of specific volume. This phenomenon was named as bulking or dilatancy. Recently the dilatancy was under investigation in connection with stress wave and general rock mechanics [20]. In this section we demonstrate how the Z-model may be extended to describe a cratering flow with dilatancy, i.e. when the volume of porous space in the target media may increase due to shear strain. To do it we need to sacrifice with a generalization of Z-model for arbitrary crater shape. The value of void volume may characterize to some extent the level of damage of rocks under the crater.

The simplest representation of dilatancy is the kinematic relation, described proportionality of the volume deformation rate, $\dot{\epsilon} = \dot{V}/V = \nabla \cdot \vec{v}$ (V - is specific volume of material), to the second invariant of the strain rate tensor,

$$J_2(\dot{V}_{ij}), \text{ where } V_{ij} = 0.5 (\partial v_i / \partial x_j + \partial v_j / \partial x_i).$$

For such a media the mass conservative law is expressed as:

$$\left. \begin{aligned} & \frac{1}{R^2} \frac{\partial}{\partial R} (R^2 v_R) + \frac{1}{R \sin \vartheta} \frac{\partial}{\partial \vartheta} (v_\vartheta \sin \vartheta) = \\ & = d \left\{ 0.5 \left[\left(\frac{\partial v_R}{\partial R} - \frac{1}{R} \cdot \frac{\partial v_\vartheta}{\partial \vartheta} - \frac{v_R}{R} \right)^2 + \left(\frac{\partial v_R}{\partial R} - \frac{v_\vartheta}{R} \cdot \operatorname{ctg} \vartheta - \frac{v_R^2}{R} \right)^2 + \right. \right. \\ & \left. \left. + \left(\frac{v_\vartheta}{R} \cdot \operatorname{ctg} \vartheta - \frac{1}{R} \frac{\partial v_\vartheta}{\partial \vartheta} \right)^2 \right] + 3 \left(\frac{1}{R} \frac{\partial v_R}{\partial R} + \frac{\partial v_\vartheta}{\partial R} - \frac{v_\vartheta}{R} \right) \right\} \end{aligned} \right\} \dots (5.21)$$

where d is the coefficient named as dilatancy coefficient. For the power law decay of radial velocity with a distance (Eq. 5.1), the above equation is simplified to the form below:

$$\begin{aligned} & -(Z-2) + f' + f \operatorname{ctg} \vartheta = \\ & = d \left\{ 0.5 \left[(Z+1+f)^2 + (Z+1+f \operatorname{ctg} \vartheta)^2 + (f' - f \operatorname{ctg} \vartheta)^2 \right] + \right. \\ & \left. + 0.75 (Z+1)^2 f^2 \right\}^{1/2} \end{aligned} \quad (5.22).$$

where function $f(\vartheta)$ describe the angle dependence of a tangential velocity:

$$v_{\vartheta} = v_R \cdot f(\vartheta), \text{ and } f' = df/d\vartheta.$$

Trajectories of particle motion now is described as

$$R/R_1 = \exp \left(\int_{\vartheta_1}^{\vartheta} f^{-1} d\vartheta \right) \quad (5.23)$$

which replace the Eq. 5.5.

One can see that for hemispheric cavities the including of dilatancy in the linear approximation conserves the main result of the traditional Z-model: any particle moves along a trajectory (a streamline) which does not change in time. Nevertheless the specific volume of any element INCREASES due to porous space increases by dilatancy:

$$\dot{V}/V = \nabla v = (A(t)/R) [-(Z-2) + f' + f \operatorname{ctg} \vartheta] \quad (5.24)$$

where $A(t)$ - is a function of time, depended on the cavity growth rate.

Using of an exact solution for the angle function $f(\vartheta)$ from the Eq. 5.22 is inconvenient as it destroy the main advantage of Z-model philosophy of simple analytical estimates. However our analysis shown that the function $f(\vartheta)$ may be affordably approximated in the familiar form of the Eq. 5.5 if one use the approach described below. One can see that the main effect of dilatancy for a given Z value is the more steep curvation of streamlines to the surface in comparison with the zero dilatation ($d=0$). As a rule in experiments one can measure deformation field much more easier than a velocity field. Then one can split the single value of Z in the traditional model into 2 values: Z_t and Z_v , where Z_t will describe trajectories in the form of Eqs. 5.5, while Z_v value will replace the "old" Z-value in the velocity field description in Eqs. 5.1 and 5.3. The relation ship between Z_t and Z_v may be found from the following consideration.

Let the stream tube has a form of Eq. 5.5 with the parameter $Z=Z_t$:

$$R = R_1 [(1 - \cos \vartheta)/(1 - \cos \vartheta_1)]^{1/(Z_t-2)} \quad (5.25)$$

and the velocity field is described by Eqs. 5.1, 5.2 with the parameter $Z=Z_v$. To fit the streamline one needs to determine the value of $f'(\vartheta=0)$. Using the limit transition one can find

$$\text{that } f'(\vartheta=0) = \frac{(Z_v - 2) + d \cdot (Z_v + 1)}{2 - d}$$

For zero dilatancy, $d=0$ (as in the standard Z -model

$$f'(\vartheta=0) = Z_t - 2$$

The initial derivative of $f(\vartheta)$ functions coincide if

$$Z_t = Z_v \frac{2 \cdot (d+1)}{2-d} \quad (5.26)$$

For simple radial flow for buried explosion $Z_t = 2$ and the Eq. 5.26 has a form

$$Z_v = \frac{2 - d}{1 + d} \quad (5.27)$$

Previously the same relationship was derived in [20], and was successfully used for the buried explosion analysis.

As one can find better way to choose proper pairs of Z_v и Z_t , the Eq. 5.27 appears to be enough correct for practical estimates.

The first check of the model we tried to do with the data by Piekutowski [19], who measured the dilatancy of dry sand under the crater. Fig. 5.4 a and b compare the volume strain distribution under the crater. The best fit occurs just under the crater. The model does not predict enhanced near-surface bulking, possibly due to air blast or some spallation effects of stress waves. Anyway the fit may be recognized as relatively good, taking into account the simplicity of the model we used. Original data similar to published in [19] may give the new challenge to test and to refine the model.

5.5. An example of mass balance for surface nuclear events.

Below we present an example of nuclear near surface burst cratering volumetric analysis for event #4 and #11 listed in the Section 3 of a current report.

Integration of the ejecta deposits thickness around craters, listed in the Section 3, allows to estimate the low limit of the

total volume of ejecta. The fitting of these data with the Z-model demonstrates the typical value of $Z_t = 2.5 \pm 0.1$. Due to the lack of direct measurements during surface events, it is hard to find the way to check these values with any direct transient displacement data. Only profiles of a structural uplift allows to check these values by restoring the uplift profile from the Z-model streamline geometry and observed shape of a crater. For current estimates we supposed the center of coordinates to be at the level of the target surface. It is possible in principle to vary the position of the coordinate center for better fitting.

To define the crater profiles, we used a scanner to digitize crater profiles, shown on pictures in the Section 3. The data on direct measurements, also displayed in the Section 3, were used to control the scale of digitized pictures. For any point at the crater profile, the streamline was traced above the preimpact process. The mass conservation (with a proper volume increase) determined the final position of the structural uplift. Closer to the crater rim, the theoretical rim profile is too steep to be stable, so partial down slide seems to be unavoidable.

It is become obvious very soon that the value of Z parameters, estimated from total ejecta volumes are too low to fit the structural uplift and the observed crater profile. At the same time, the mean density of the uplift is definitely smaller than initial target material density. So the supposition of dilatancy of a matter during cratering becomes to be natural. Unfortunately, the theory described at the previous section works exactly only for hemispheric cavities. If the shape of the cavity differs from the hemisphere, it means that shear strain may be larger than for a hemispheric cavity (neighbor streamlines have larger relative displacement).

Nevertheless for simple estimates we used the model relations Eqs. 5.4 (with $Z=Z_t$) and 5.26 to describe the cratering flow with dilatancy. In such an approximation the modest value of the dilatancy coefficient $d \approx 0.2$ produce much better fitting than the standard Z-model. As uplift fitting allow to estimate the "trajectory" value, Z_t , the "velocity" Z-value, Z_v , is calculated from Eq. 5.26.

Figs. 5.5 and 5.6 demonstrates the best fitting we found for 4 cross section of each of craters.

For events #4 and #11 the best value of Z_t was found as 2.6 and 2.67 correspondingly (which coincides with the total ejecta volume estimates). For $d=0.2$, the value of Z_y is about 2.0 - much lower than traditional fitting of crater computational velocity field: 2.7 to 3.

The dilatancy is naturally suppressed by high pressures, as well as the dilatancy stop to be linear one as the material begin to be very loose. So the range of pressure and volume strain exist where the dilatancy really can play some role. The effect was thoroughly investigated for stress wave decay, but it is very important to find the proper place of the dilatancy in cratering flow field description.

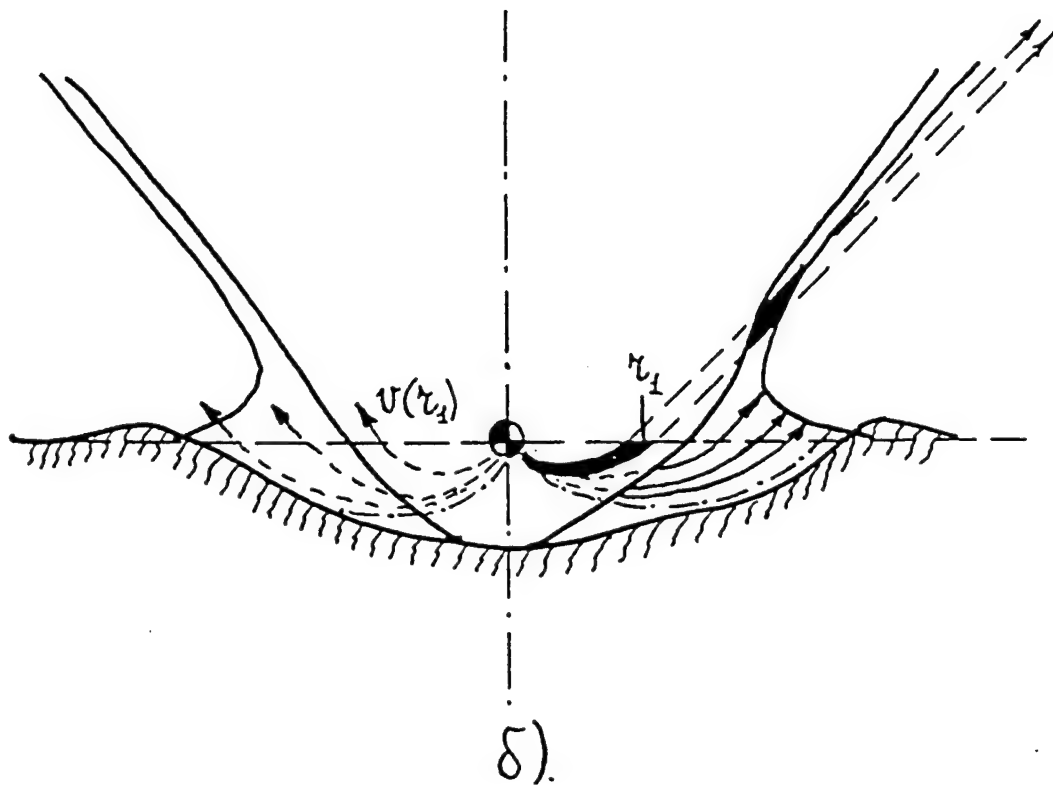
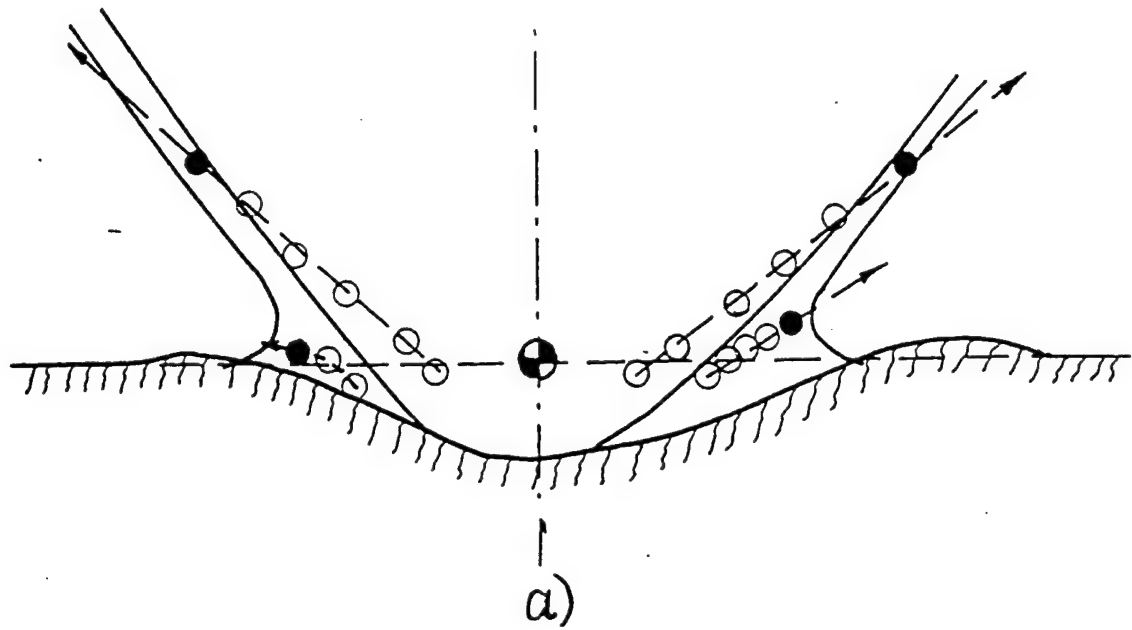
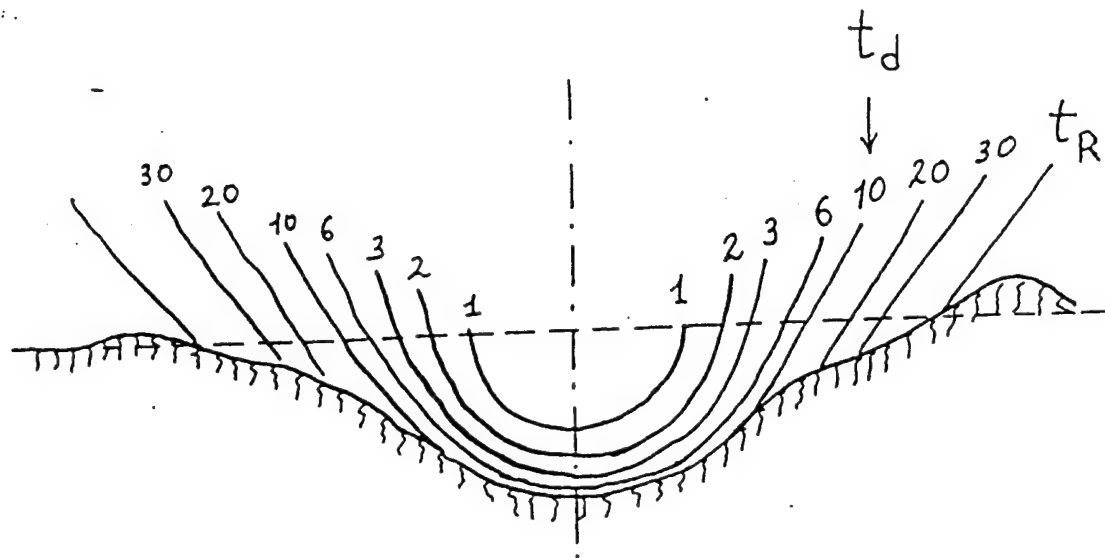
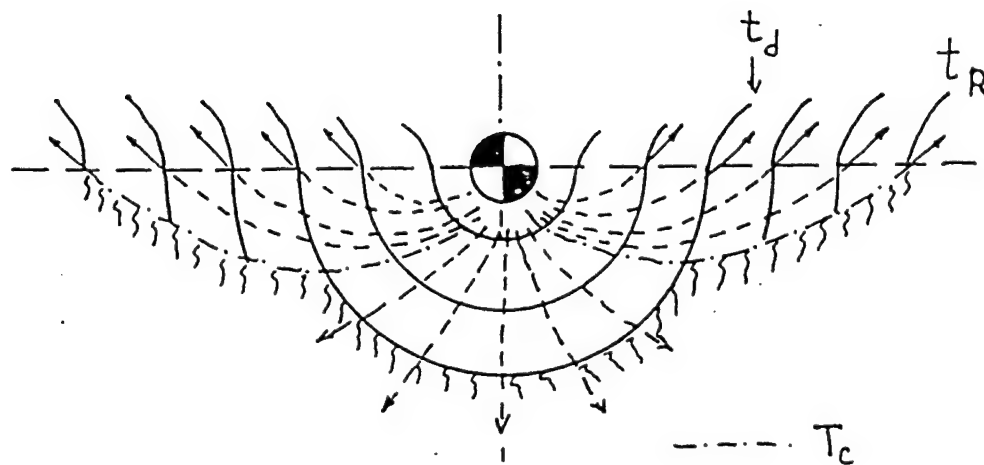


Fig. 5.1. a). An example of a quarter-space experiment. The high speed movie frames was overlapped to plot ejecta trajectories. Plastic disks embedded to the wet sand are ejected with decreasing with the ejection distance velocities. (b) Z-model representation of the same experiment. The material ejected along a stream tube at a later may be seen at the ejecta curtain.



a).



b).

Fig. 5.2. (a) Crater profile's evolution plotted from overlapped high speed movie frames. Profiles is numbered at the figure in ms. The time of crater depth formation, t_d , is about 3 times smaller then the crater radius formation. (b) Z-model representation of the same process. For some target media (i.e. for wet sand) one can find the critical time T_c .

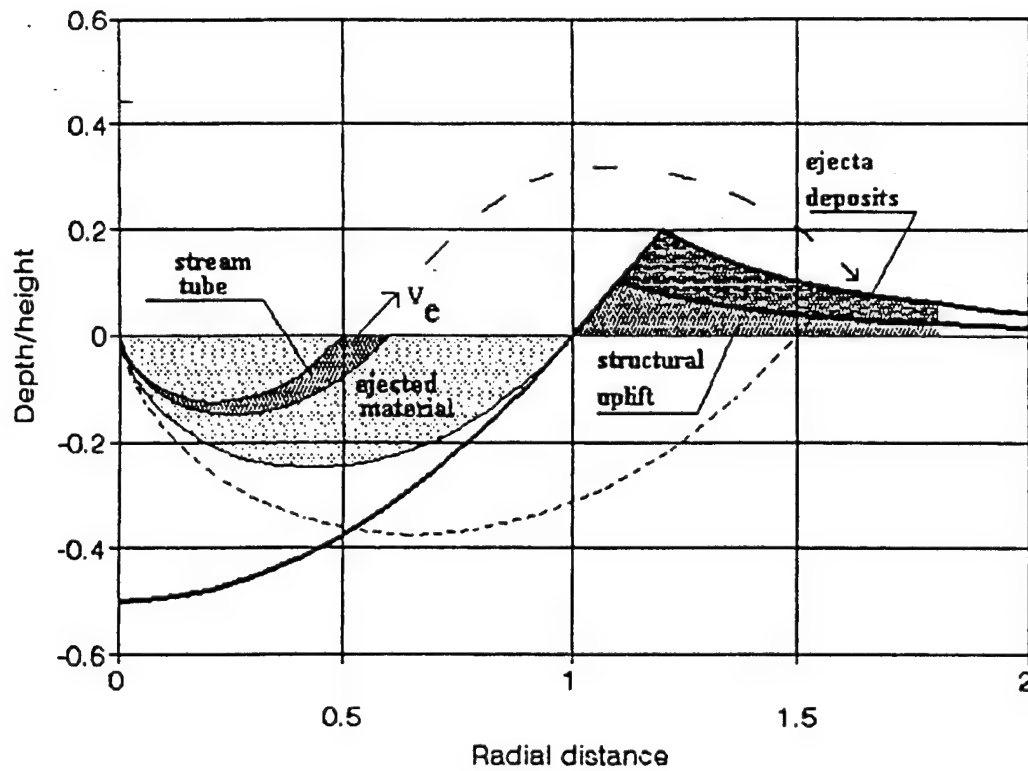
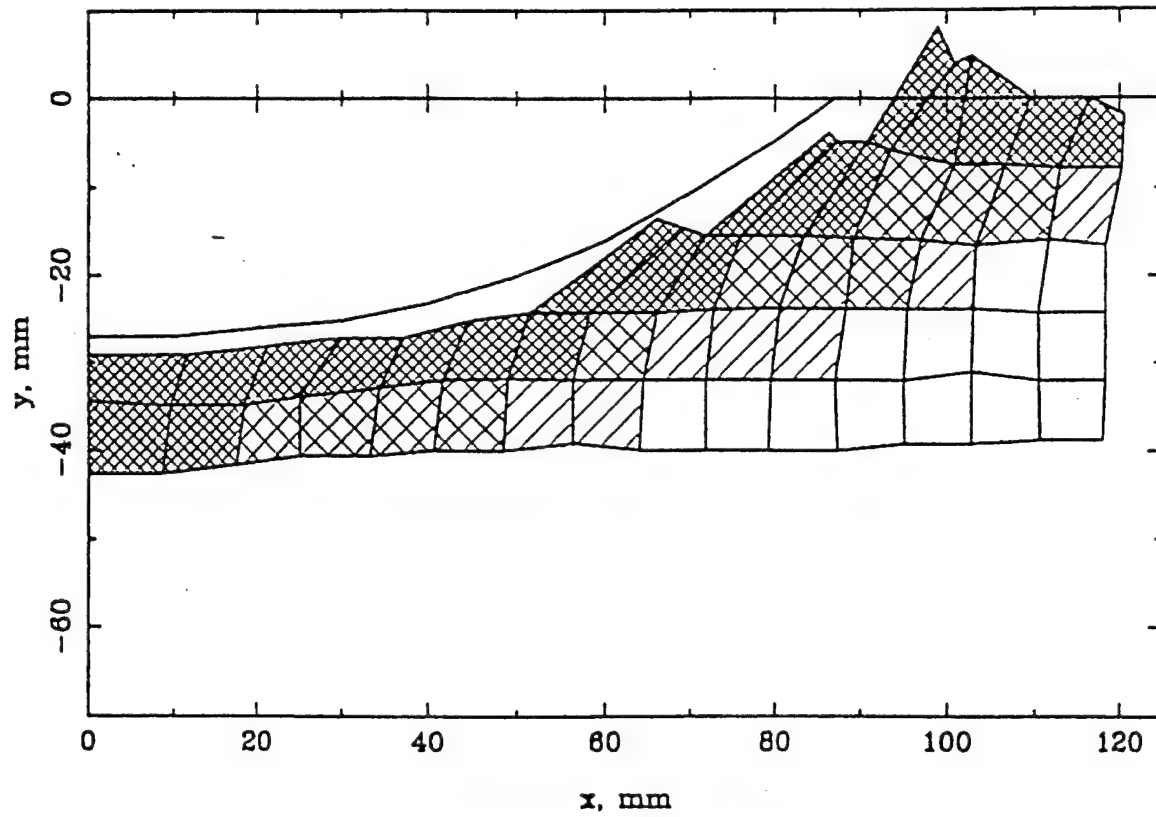


Fig. 5.3. A general view of a mass balance during cratering according to the Z-model.



Z-model with dilatancy

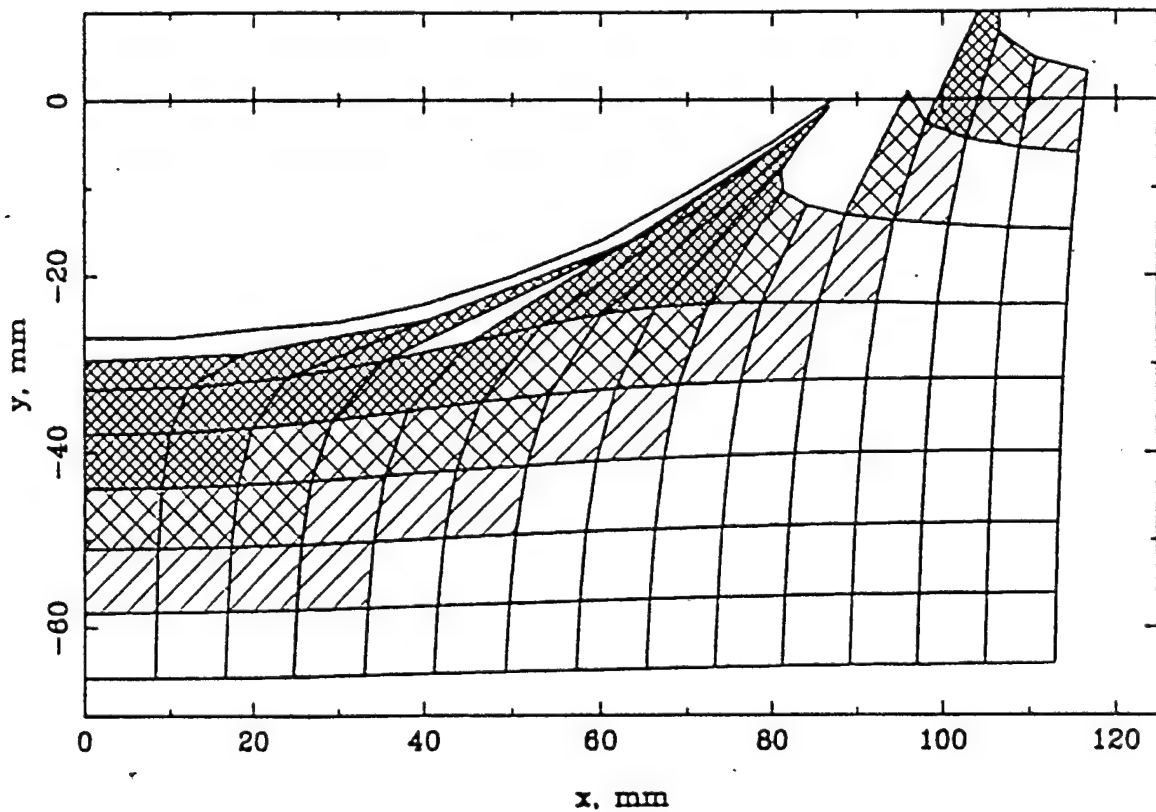


Fig.5.4. (a) Experimental data [19] illustrating the sand.

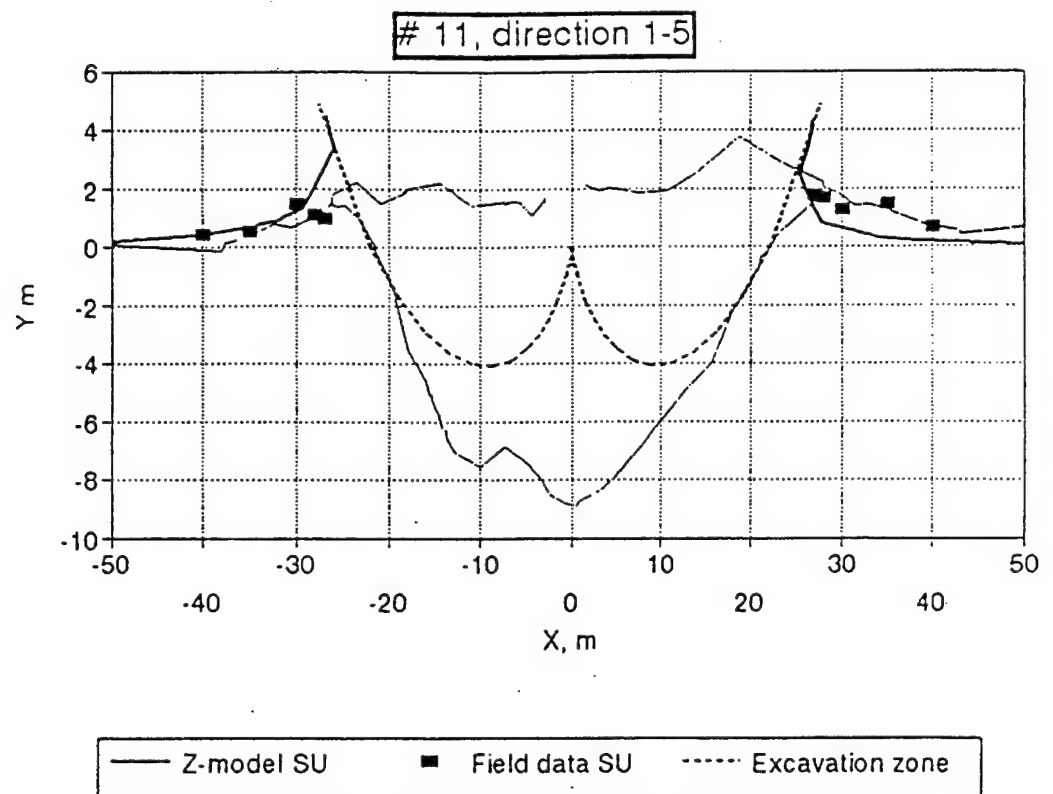


Fig. 5.5. Structural uplift for the surface burst #4 in comparison with Z-model estimates.

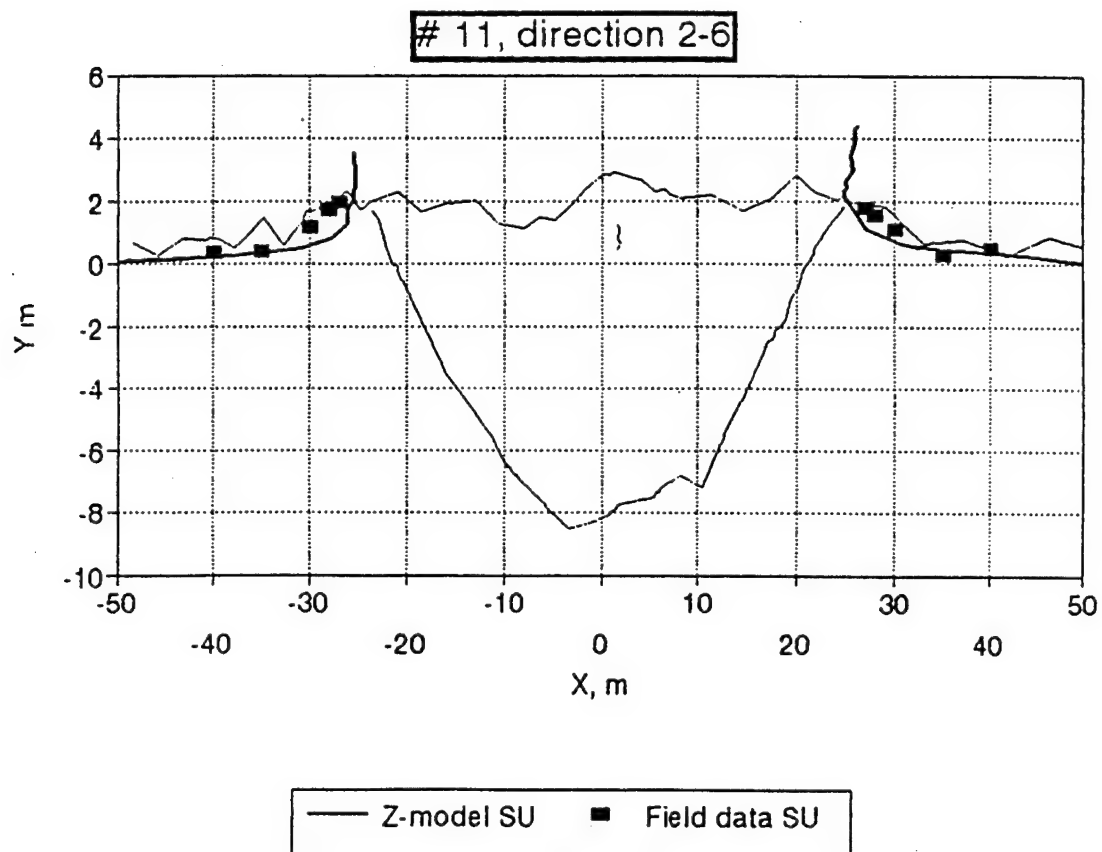


Fig. 5.5 (continuation)

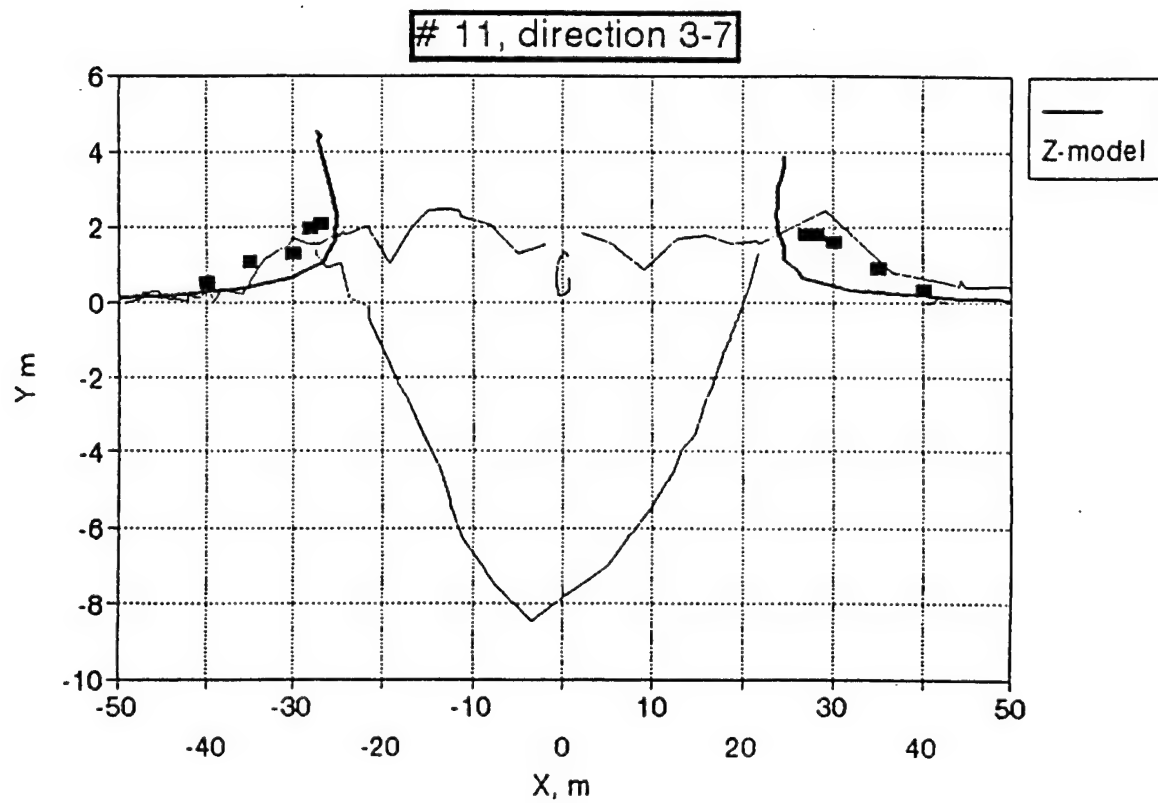


Fig. 5.5 (continuation)

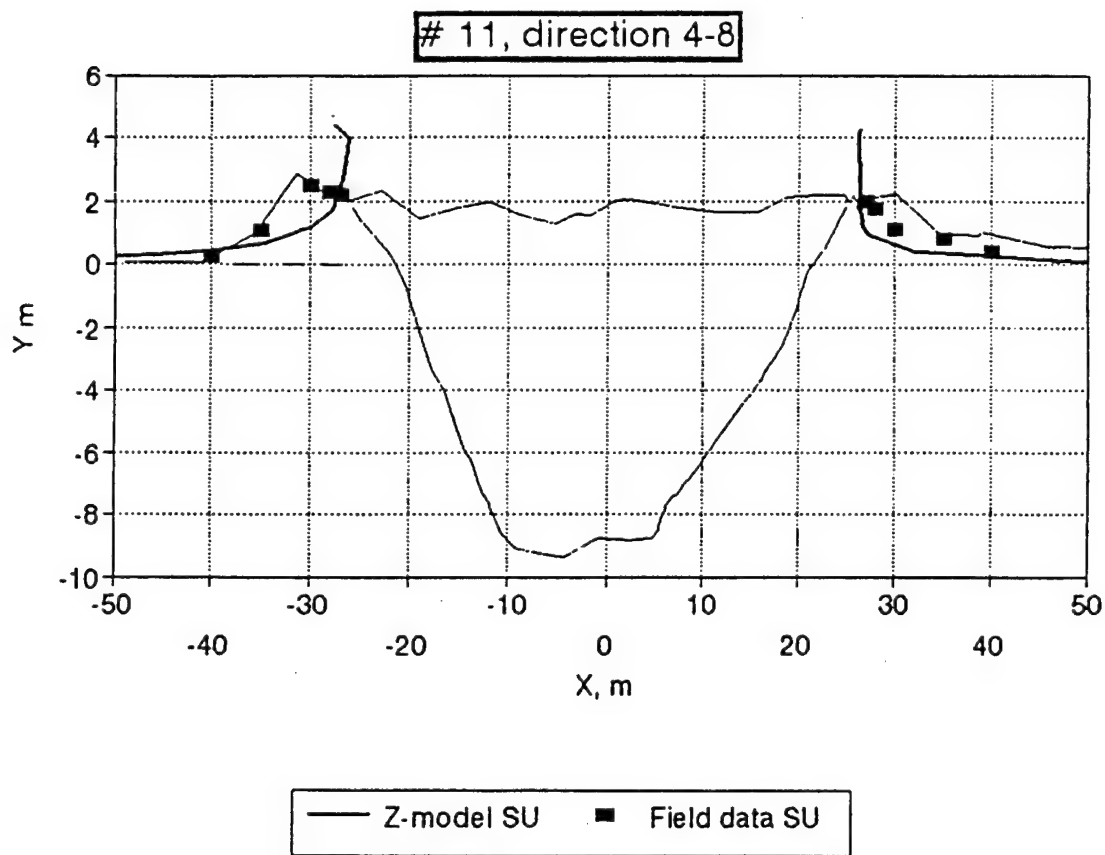


Fig. 5.5 (continuation)

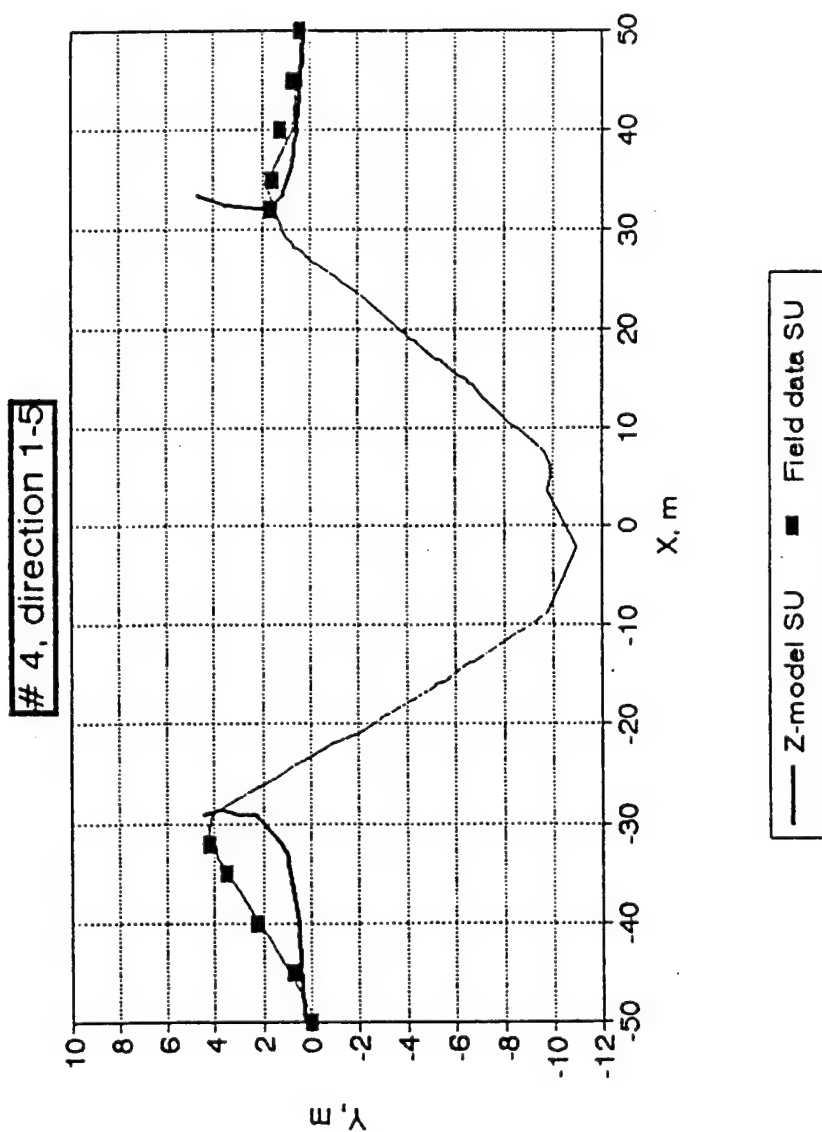


Fig. 5.6. Structural uplift for the surface burst #11 in comparison with Z-model estimates.

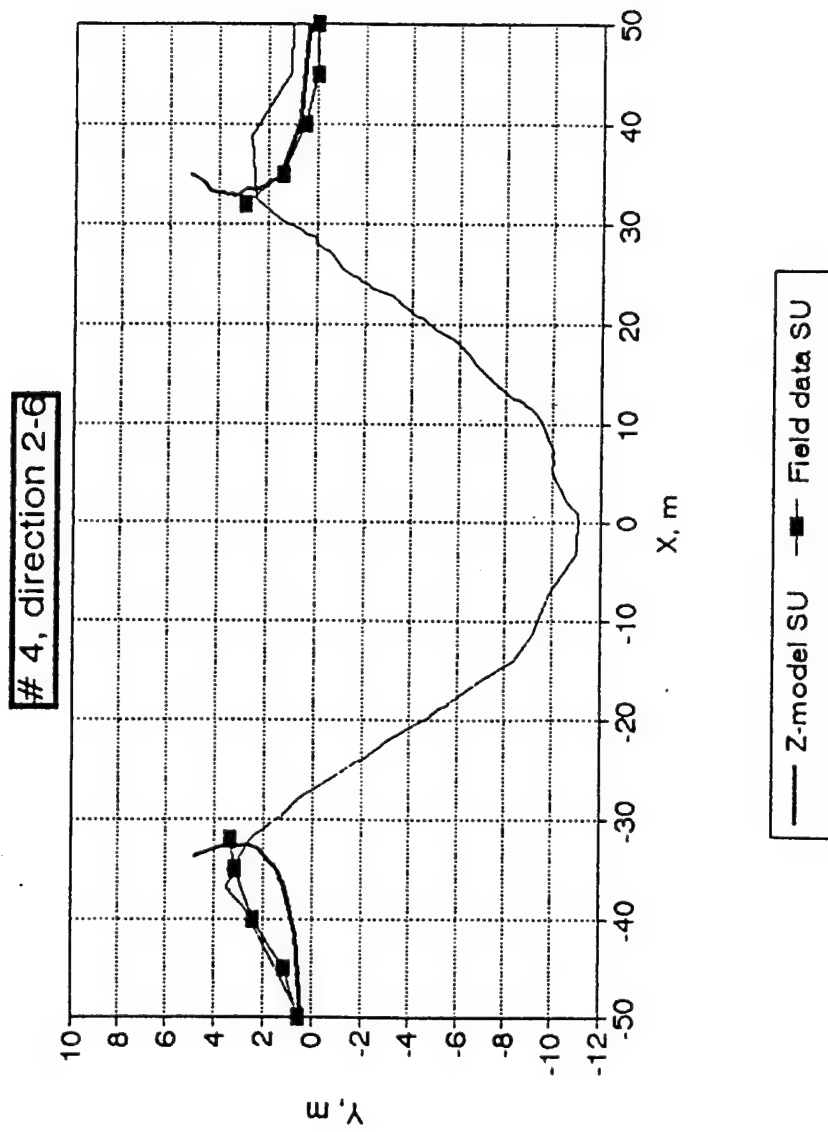


Fig. 5.6 (continuation)

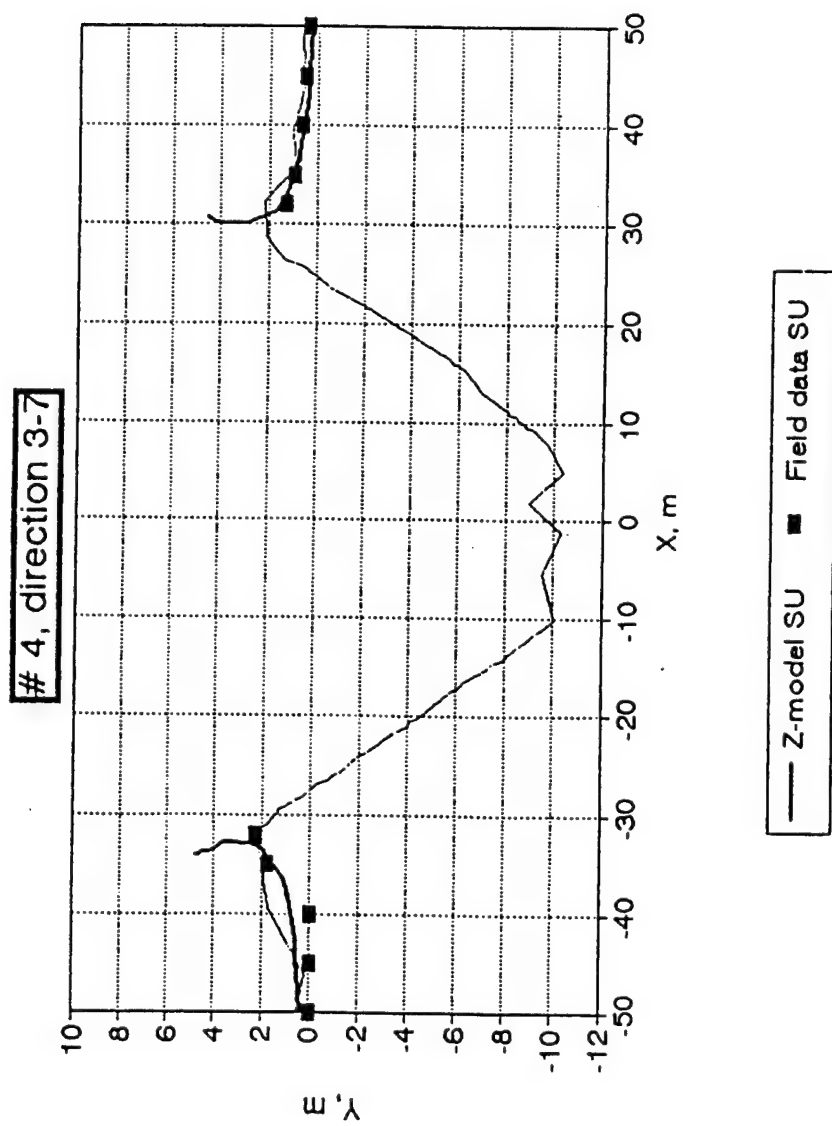


Fig. 5.6 (continuation)

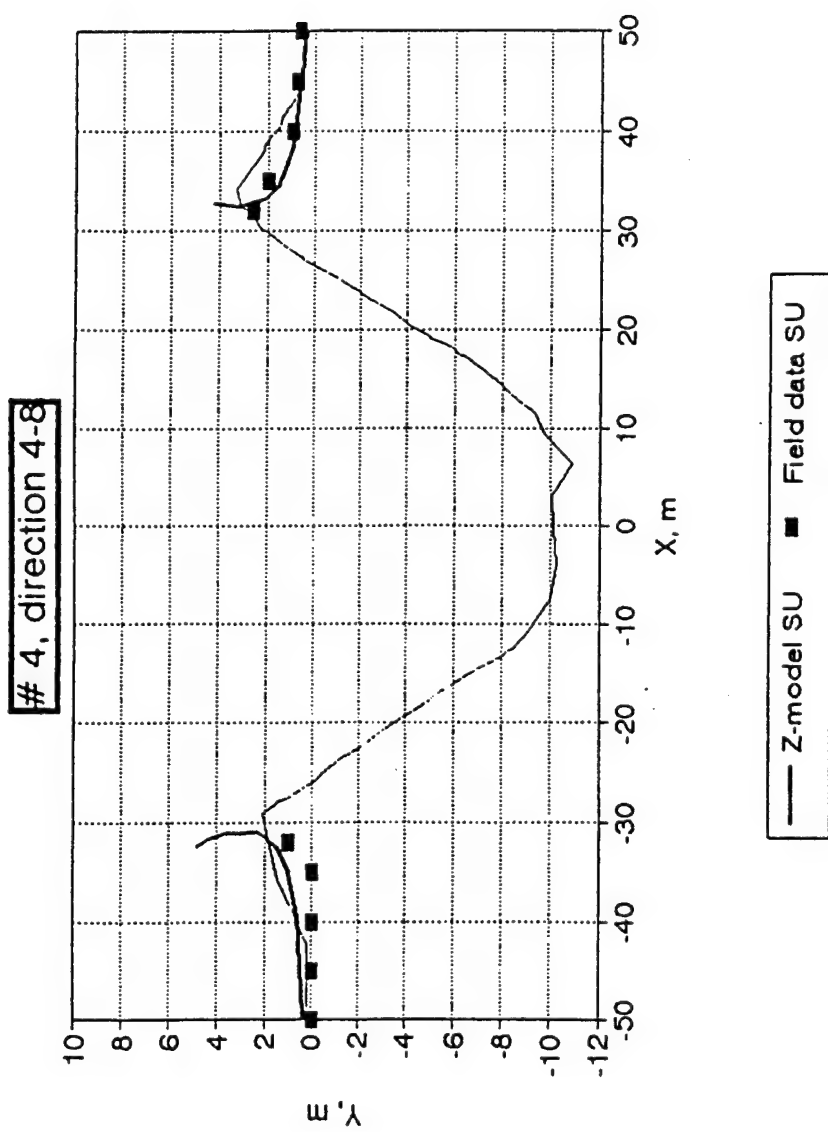


Fig. 5.6 (continuation)

6. References

1. Botcharov V.S., S.A.Zelentsov, and V.N.Mikhailov (1989) Characteristics of 96 underground nuclear explosions at the Semipalatinsk Test Site. Atomic Energy, V. 67, #3, 210-214 (in Russian).
2. Gorin V.V., G.A.Krasilov, A.I.Kurkin, A.L.Mal'tzev, A.M.Matuschenko, S.L.Orlov, A.V.Pitchugin, S.G.Smagulov, V.G.Strukov, V.I.Filippovsky, K.V.Kharitonov, A.K.Tchernyshov, and M.V.Shumakov. Semipalatinsk Test Site: Chronology of underground nuclear explosions and their primary radiation effects (1961-1989).
3. Nuclear Explosions for Peaceful Purposes (1970). Collection of papers. Atomizdat Public House, Moscow.
4. Maxwell D.E. (1976) Simple Z-model of cratering ejection and the overturned flap. in Abstracts for the Symposium on Planetary Cratering Mechanics, Flagstaff, Arizona, 13-17 September 1976. Lunar Science Institute, Houston, p. 72.
5. Allen R.T. (1976) Late-stage effects in crater and ejecta deposition. Ibid., p.4-5.
6. Ivanov B.A. (1976) On the mechanics of the surface explosion. Ibid., p.56-58.
7. Ivanov B.A., and Comissarova L.I. (1977) The simple hydrodynamic model of cratering (abstract). Lunar Science VIII, p.499-501.
8. Maxwell D., and K. Seifert (1974) Modeling of cratering, close-in displacements, and ejecta. DNA Report 3628F, 1975, 108 pp.
9. Ivanov B.A. (1979) Simple model of cratering. Meteoritika # 38, Nauka Press, Moscow, 68-85 (in Russian).

- 34
10. Ivanov B.A. (1977) On mechanical effects of explosion near ground surface. *Fizika gorenia i vzryva*, 1977, #1, 110-113.
 11. Ivanov B.A. (1983) The model of cratering in ideal-plastic media (abstract). *Lunar and Planetary Science XIV*, 343-344.
 12. B.A.Ivanov (1976). The effect of gravity on crater formation: thickness of ejecta and concentric basins, in *Proc. Lunar Sci. Conf 7th*, pp. 2947-2965.
 13. Ivanov B.A. (1981) Cratering mechanics, In *Advances in Science and Technology of VINITI, Ser. Mechanics of Deformable Solids*, v. 14, Moscow, VINITI Press, p. 60-128, in Russian - see also English translation: NASA Tech. Memorandum 88477/N87-15662, 1986.
 14. Holsapple K.A. and R.M.Schmidt (1979) A material-strength model for apparent crater volume. Proc. Lunar Planet. Sci. Conf. 10th, pp. 277-2777.
 15. Schmidt R.M. (1980) Meteor Crater: Energy of formation - implications from centrifuge scaling. Proc Lunar Planet. Sci. Conf. 11th, pp. 2099-2128.
 16. Neukum G., and B.A.Ivanov. Crater size distributions and impact probabilities on Earth from lunar, terrestrial-planet, and asteroid cratering data. In the book "Asteroidal Hazard", Arizona University Press, 1994, (in press).
 - 17 Housen K.R., R.M.Schmidt, and K.A.Housen (1983) Crater ejecta scaling laws: Fundamental forms based on dimensional analysis. J. Geophys. Res., 88: 2485-2499.
 - 18 Ivanov B.A. (1989) Z-model with shear bulking and gravity anomalies above impact craters, *LPSC XX*, 446-447.

22

19. Piekutowski A.J. (1980) Formation of bowl-shaped craters.
Proc Lunar Planet. Sci. Conf. 11th, pp. 2129-22144.

20. Rodionov V.N., V.V.Adushkin, V.N.Kostuchenko,
V.N.Nikolaevsky, A.N.Romashov, and V.M.Tsvetkov (1971)
Mechanical effects of underground explosions. Nedra Press,
Moscow, 222 p.

Appendix

Terminology and Nomenclature

Below we explain some details of terminology for sedimentary rocks used in the presented report.

алеверит (alevrite) - рыхлая осадочная порода, по составу промежуточная между песчаными и глинистыми породами с размером главной массы зерен 0.01 - 0.1 мм

алевролит (alevtolite) - сцементированный алеверит; сцементированный тонкодисперсный материал (более 50 % частиц 0.01-0.1мм)
 Плотность 2.68-2.75 г/см³,
 прочность на сжатие 49-78 МПа
 прочность на растяжение 5.9-8.8 МПа
 скорость продольных волн 4500-5500 м/с

аргиллит (argillite)- осадочная горная порода, образовавшаяся в результате уплотнения, обезвоживания и цементации глин; отличается от глин большей твердостью и неспособностью размокать в воде

супесь (sandy loam, sandy soil)- песчно-глинистая порода, содержащая 10-20% примеси глинистых частиц
 супесь,
 супесчаная почва = sandy clay

суглинок, суглинистая почва = sandy loam
суглинок - (loam, loam soil) глина низкой пластичности с примесью 30-40% песка
 глинистый, суглинистый, мергельный = loamy
 бурый суглинок = silt loam -

глинистый сланец, сланцевая глина =	shale
песчано-глинистый сланец =	sandy shale
углистый сланец =	carbonaceous shale

Grain size:

Psephites (rudites, gravel, rubble, boulder, pebble) are clustic sediments with more than 50% (by weight) of the constituents > 2 mm in diameter.

Psammites (arenites; sand) have more than 50% of their grains within the sand fraction (2 to 0.002 mm)

Pelites (argillites; clay, mud) are restricted to grain size < 0.002 mm. A transitional grain size fraction within the psammite fraction is that of silt (from 0.06 to 0.002 mm)

Approximate correspondence of English and Russian nomenclature of sedimentary rocks: English nomenclature according to [3]; Russian nomenclature (I): according to [1]; (II): according to geologic description in primary reports.

Particle Diameter, mm	<1/256 (< 0.004)	1/256 to 1/16 (0.004 to 0.06)	1/16 to 2 (0.06 to 2)	2 to 4	4 to 64	64 to 256	> 256
Particles	Clay	Alevrite (Silt)	Sand	Gravel	Pebble	Cobble	Boulder
Kind of rock	Clay Argilite	Alevrite Alevrolite, Siltstone	Sand, sandstone	Conglomerate, Breccia			
Частицы мм (I)	Глина < 0.01	Алеврит 0.01 to 0.1	Песок 0.1 to 1	гравий 1 to 10	галька 10 to 100	валуны 100 mm to 10 m	
Частицы мм (II)				дресва 2 to 20	щебень 20 to 200	валуны >200	
Породы	Глина Аргиллит	Алеврит, алевролит (Песок Песчаник	Конгломерат, брекчия			

дресва 2-20 мм = pebble

щебень 20-200 мм = rubble

Both may be named as breccia with different fragment size.

Used references

1. Советский Энциклопедический Словарь. Москва, Советская Энциклопедия, 1984 г., 1600 стр.
2. Терминологический словарь по вопросам использования подземных ядерных взрывов в мирных целях (Глоссарий). Под ред. О.Л.Кедровского, М.П.Гречушкина и Л.Б. Прозорова. Отдел научно-технической информации, 1981 г., 41 стр.
3. J. Verhoogen, F.J.Turner, L.E.Weiss, C. Wahrhaftig, and W.S. Fyfe. The Earth. An introduction to physical geology. Holt, Reinehart abd Winston, Inc. NY-Chicago-SF, Atlanta-Dallas-Montreal-Toronto-London-Sydney. Russian translation: Земля: Введение в общую геологию, Москва, Мир, 1974, 845 стр.
4. New English-Russian Dictionary (in two volumes) (Galperin I.R. Ed.). Soviet Encyclopedia Publishing House, Moscow, 1972, Vol.1 - 822 pp., Vol 2 -863 pp.
5. Russian-English Dictionary (Smirnitsky A.I. Ed.) State Publishung House of Foreign and National Dictionaries, Moscow, 1962, 951 pp.
6. Landolt-Bornstein. Numerical Data and Functional Relationships in Science and Technology, New Series, Group V: Geophysics and Space Research, Volume 1: Physical properties of Rocks (G.Angenheister Ed.), Springer-Verlag, Berlin-Heidelberg-NY, 1982, Subvolume a - 373 pp., Subvolume b - 604 pp.

DISTRIBUTION LIST

DNA-TR-95-71

DEPARTMENT OF DEFENSE

DEFENSE INTELLIGENCE AGENCY
ATTN: DIW-4

DEFENSE NUCLEAR AGENCY
ATTN: DFTD D LINGER
2 CY ATTN: OSIA
ATTN: RAES
ATTN: RAST W SUMMA
ATTN: SPSD
ATTN: SPSD D PYLE
ATTN: SPSD P SENSENY
2 CY ATTN: SPWE E TREMBA
ATTN: SPWE LEON A WITTWER
2 CY ATTN: SSTL
ATTN: T HOOVER
ATTN: TAIC
ATTN: TDTR
ATTN: TDTV F RENSVD

DEFENSE TECHNICAL INFORMATION CENTER
2 CY ATTN: DTIC/OCF

FIELD COMMAND DEFENSE NUCLEAR AGENCY
ATTN: NVCG

FIELD COMMAND DEFENSE NUCLEAR AGENCY
ATTN: FCTI G S LU
ATTN: FCTO
ATTN: FCTT-T B RISTVET
ATTN: FCTT-T E RINEHART
ATTN: FCTT DR BALADI
2 CY ATTN: FCTTS A MARTINEZ
ATTN: FCTTS R HENNY
ATTN: FCTTS R REINKE

DEPARTMENT OF THE ARMY

ADVANCED RESEARCH PROJECT AGENCY
ATTN: GSD R ALEWINE
ATTN: RMO RETRIEVAL

ARMY RESEARCH LABORATORIES
ATTN: TECH LIB

PED MISSILE DEFENSE SFAE-MD-TSD
ATTN: CSSD-SA-EV
ATTN: CSSD-SL

U S ARMY CORPS OF ENGINEERS
ATTN: CERD-L

U S ARMY ENGINEER DIV HUNTSVILLE
ATTN: HNDED-SY

U S ARMY ENGR WATERWAYS EXPR STATION
ATTN: D RICKMAN CEWES-SE-R
ATTN: E JACKSON CEWES-SD-R
ATTN: J ZELASKO CEWES-SD-R
ATTN: RESEARCH LIBRARY

U S ARMY MATERIAL TECHNOLOGY LABORATORY
ATTN: TECHNICAL LIBRARY

U S ARMY NUCLEAR & CHEMICAL AGENCY
ATTN: MONA-NU DR D BASH

U S ARMY RESEARCH LAB
ATTN: SLCBR-SS-T

DEPARTMENT OF THE NAVY

NAVAL RESEARCH LABORATORY
ATTN: CODE 5227 RESEARCH REPORT

NAVAL SURFACE WARFARE CENTER
ATTN: CODE K42 R ROBINSON
ATTN: CODE K42 S HUGHES

NAWCWPNSDIV DETACHMENT
ATTN: CLASSIFIED LIBRARY

NFESC
ATTN: CODE L64 LORY

NUWC, DETACHMENT NLON
ATTN: CODE 0261

OFFICE OF NAVAL RESEARCH
ATTN: CODE 1132SM

DEPARTMENT OF THE AIR FORCE

AF TECHNICAL APPLICATIONS CENTER
ATTN: ROBERT BLANDFORD

AFSOR/NP
ATTN: COL JERRY PERRIZO

AIR FORCE TECHNICAL APPLICATIONS CTR
ATTN: FRANK PILOTTE TT
ATTN: GEORGE ROTHE TTR

AIR UNIVERSITY LIBRARY
ATTN: AUL-LSE

GEOPHYSICAL LABORATORY
ATTN: JAMES LEWKOWICZ
ATTN: XO

HQ 497 IG/INOT
ATTN: INT

DEPARTMENT OF ENERGY

DEPARTMENT OF ENERGY
NEVADA OPERATIONS OFFICE
ATTN: OTIS D H MARTIN

DEPARTMENT OF ENERGY
ATTN: DR C V CHESTER

DNA-TR-95-71 (DL CONTINUED)

LAWRENCE LIVERMORE NATIONAL LAB

ATTN: R DONG
ATTN: D B CLARKE
ATTN: WILLARD J HANNON JR
ATTN: G POMYKAL

LOS ALAMOS NATIONAL LABORATORY

ATTN: BOB DEUPREE
ATTN: M HENDERSON
ATTN: PAUL JOHNSON
ATTN: FRED APP
ATTN: T KUNKLE
ATTN: R P WEAVER
ATTN: D STROTTMAN
ATTN: REPORT LIBRARY
ATTN: S TAYLOR
ATTN: R KIRBY
ATTN: TECH LIBRARY

SANDIA NATIONAL LABORATORIES

ATTN: J M MCGLAUN 6444
ATTN: MIKE FURNISH
ATTN: T K BERGSTRESSER DIV 9311
ATTN: TECH LIB 3141
ATTN: 9312 C W SMITH
ATTN: 9312 D GARBIN

OTHER GOVERNMENT

CENTRAL INTELLIGENCE AGENCY

ATTN: KATIE POLEY
ATTN: OSWR/NED L TURNBULL
ATTN: OSWR/NED 5S09 NHB

U S ARMS CONTROL & DISARMAMENT AGCY

ATTN: A LIEBERMAN

US GEOLOGICAL SURVEY NATIONAL CENTER

ATTN: W LEITH

DEPARTMENT OF DEFENSE CONTRACTORS

AEROSPACE CORP

ATTN: LIBRARY ACQUISITION

APPLIED RESEARCH ASSOCIATES, INC

ATTN: C J HIGGINS

APPLIED RESEARCH ASSOCIATES, INC

2 CY ATTN: S BLOUIN

APPLIED RESEARCH ASSOCIATES, INC

ATTN: R FRANK

BDM FEDERAL INC

ATTN: E DORCHAK
ATTN: J STOCKTON

BOEING TECHNICAL & MANAGEMENT SVCS, INC

ATTN: ROBERT M SCHMIDT

CALIFORNIA INSTITUTE OF TECHNOLOGY

ATTN: T AHRENS

CARPENTER RESEARCH CORP

ATTN: H J CARPENTER

ENSCO, INC

ATTN: DOUGLAS BAUMGARDT

HORIZONS TECHNOLOGY, INC

ATTN: B LEE

IIT RESEARCH INSTITUTE

ATTN: DOCUMENTS LIBRARY
ATTN: M JOHNSON

INSTITUTE FOR DEFENSE ANALYSES

ATTN: CLASSIFIED LIBRARY

JAYCOR

ATTN: CYRUS P KNOWLES

KAMAN SCIENCES CORP

ATTN: D CAYNE
ATTN: LIBRARY

KAMAN SCIENCES CORP

ATTN: DASAC

KAMAN SCIENCES CORPORATION

ATTN: DASAC

KTECH CORP

ATTN: F DAVIS

LACHEL AND ASSOCIATES, INC

ATTN: J BECK

LOGICON R & D ASSOCIATES

ATTN: C K B LEE
ATTN: D SIMONS
ATTN: LIBRARY

LOGICON R & D ASSOCIATES

ATTN: J RENICK
ATTN: L GERMAIN

LOGICON R & D ASSOCIATES

ATTN: D PIEPENBURG

MAXWELL LABORATORIES INC

ATTN: DR J L STEVENS
ATTN: DR K L MCLAUGHLIN
ATTN: DR C DISMUKES
ATTN: K D PYATT JR
ATTN: R LAFRENTZ
ATTN: S PEYTON

MAXWELL LABORATORIES, INC

ATTN: J MURPHY

MCDONNELL DOUGLAS CORPORATION

ATTN: R HALPRIN

MISSION RESEARCH CORP

ATTN: TECH LIBRARY

PACIFIC-SIERRA RESEARCH CORP

ATTN: H BRODE

S-CUBED

ATTN: JACK MURPHY

SCIENCE APPLICATIONS INTERNATIONAL CORP
ATTN: R SCHLAUG

SCIENCE APPLICATIONS INTL CORP
ATTN: G EGGUM
ATTN: G PHILLIPS
ATTN: H WILSON
ATTN: L SCOTT
ATTN: M MCKAY
ATTN: T C BACHE JR
ATTN: TECHNICAL REPORT SYSTEM
ATTN: W WOOLSON

SCIENCE APPLICATIONS INTL CORP
ATTN: J COCKAYNE
ATTN: W LAYSON

SOUTHERN METHODIST UNIV
ATTN: DR BRIAN STUMP

SRI INTERNATIONAL
ATTN: A FLORENCE
ATTN: DR JIM GRAN

TECH REPS, INC
ATTN: F MCMULLAN

TERRA TEK, INC
ATTN: S GREENE

TITAN CORPORATION
ATTN: J THOMSEN

TITAN CORPORATION (THE)
ATTN: LIBRARY
ATTN: S SCHUSTER

TRW INC
ATTN: TIC

TRW S.I.G.
ATTN: NORMAN LIPNER

TRW SPACE & DEFENSE SECTOR
ATTN: W WAMPLER

WASHINGTON, UNIVERSITY OF
ATTN: J KATZ

WEIDLINGER ASSOC, INC
ATTN: H LEVINE

WEIDLINGER ASSOCIATES, INC
ATTN: T DEEVY

WEIDLINGER ASSOCIATES, INC
ATTN: I SANDLER
ATTN: M BARON

FOREIGN

INSTITUTE FOR DYNAMICS OF
2 CY ATTN: B IVANOV
2 CY ATTN: L PERNIK
2 CY ATTN: V ADUSHKIM